

Life Cycle Management of Steel Bridges Based on NDE and Failure Analysis

**Principal Investigators: Professor Brian Moran and
Professor Jan Achenbach**

A final report submitted to the Infrastructure Technology Institute for TEA-21 funded projects designated A429, A439, and A453

DISCLAIMER: The contents of this report reflect the views of the authors, who are responsible for the facts and accuracy of the information presented herein. This Document is disseminated under the sponsorship of the Department of Transportation University of Transportation Centers Program, in the interest of information exchange. The U.S. Government assumes no liability for the contents or use thereof.

NORTHWESTERN UNIVERSITY

STRUCTURAL INTEGRITY ASSESSMENT OF PIN AND HANGER
CONNECTION OF AGING HIGHWAY BRIDGES USING FINITE
ELEMENT ANALYSIS

A DISSERTATION

SUBMITTED TO THE GRADUATE SCHOOL
IN PARTIAL FULFILLMENT OF THE REQUIREMENTS

for the degree

DOCTOR OF PHILOSOPHY

Field of Mechanical Engineering

By

David Houcque

EVANSTON, ILLINOIS

June 2008

© Copyright by David Houcque 2008

All Rights Reserved

ABSTRACT

STRUCTURAL INTEGRITY ASSESSMENT OF PIN AND HANGER CONNECTION OF AGING HIGHWAY BRIDGES USING FINITE ELEMENT ANALYSIS

David Houcque

The finite element method is used to investigate failure mechanisms in pin-hanger connection in aging highway bridges. Bridge pins and hangers are typically considered as critical elements whose failure may result in partial or entire collapse of the structure. The primary function of a pin-hanger connection is to allow for longitudinal thermal expansion and thermal contraction in the bridge super-structure due to temperature changes (daily or seasonal). The induced movements, due to thermal effects, have considerable impact on bridge design and performance. Thus, in addition to the applied mechanical loads (dead load and traffic), the thermal load due to temperature changes is also included.

A key goal was also to relate original design calculations (before the bridge was built) to the current analysis which accounts for the entire bridge structure under combined loads and extreme environmental conditions.

Many bridges in use today have deteriorated due to aging, misuse, or lack of proper maintenance. After years of exposure to atmospheric environments (deicing salts and load

variations), corrosion and wear tend to produce at least a partially fixed (or locked up) condition. Pack-rust (or corrosion buildup) can have two detrimental effects on the pin:

- First, the cross-section of the pin can “decrease” because of corrosive section loss. The corrosion can produce pitting that may act as crack initiation sites.
- Second, pack-rust can effectively “lock” the pin within the connection, so that no rotation is permitted. This may produce a likely location for the development and propagation of cracks.

Furthermore, bridge structure is *nonlinear* especially when the pin is in the locked condition and an elastic-plastic analysis is required to model the bridge behavior when the pin is locked.

One of the main focuses in this study is on the determination of the three-dimensional (3D) crack growth in the pin, since the lifetime of the entire structure is dependent on the behavior of cracks.

Due to the accessibility of 3D finite element programs and the comparatively low cost of computing time, it is state of the art to perform 3D analyses of complex engineering problems. The finite element program ABAQUS has been used throughout the investigation, which essentially includes:

- stress analysis
- thermal effects
- elastic-plastic analysis
- determination of the mixed-mode stress intensity factors (K_I , K_{II} , and K_{III})
- fatigue crack growth simulation

Furthermore, since analytical solutions are not available in many cases, especially for this 3D problem (with complex geometry and loading conditions), a series of validation tests were performed on bridge components.

Acknowledgements

I feel honored to have been chosen to work in this project and to have had the chance to meet and work with outstanding experts in this field. It is a pleasant aspect that I have now the opportunity to express my gratitude to all of them who made this thesis possible.

Let us recall that the thrust of the thesis is to develop an understanding of failure mechanisms in pin-hanger connections in aging highway steel bridges. The initiative to start working with this problem was taken by the Infrastructure Technology Institute (ITI) at Northwestern University, led by the late David Schulz (former Director), David Prine and Dan Hogan, in parallel with the work performed by Igor Komsky and Professor Jan Achenbach who initiated the investigations by using ultrasonic testing. Special thoughts go to the late ITI Director, David Schulz. His charismatic and leadership will be missed for ever.

I would like to thank my advisor, Professor and Chair Brian Moran, for providing me with the opportunity to complete my thesis at Northwestern University. His help and guidance throughout the work have been very valuable for me. I especially want to thank him for introducing me to the concepts of fracture mechanics used in the area of the joint connections in aging bridges, and also for giving me the opportunity to perform this thesis in collaboration with the Infrastructure Technology Institute (ITI). Many thanks to all of the ITI members who gave their monthly presentation, and from whom I learned much

about bridge engineering. They also provided valuable comments on my progress reports as my work developed.

I would like to thank the Committee Members of the thesis: Professor Jan Achenbach, Professor Edwin Rossow, and Professor Ken Shull, for their valuable suggestions and recommendations.

Acknowledgement is also due to the Wisconsin Department of Transportation (WisDOT), in particular to Finn Hubbard the bridge design supervisor, for providing bridge drawings and original design calculations.

For the non-scientific side of my thesis, I particularly want to thank the Associate-Dean of the McCormick School of Engineering and Applied Science at Northwestern University, Stephen Carr. Dean Stephen Carr gave me the opportunity to be the lab instructor (“Introduction to MATLAB programming for engineering students”) of the Engineering Analysis (EA) sections. I enjoyed working with the first year undergraduate students and especially relished the opportunity of sharing with them the real world experiences I had acquired in more than 20 years in industry (in Europe and the USA). The lab instructor position also gave me financial support to continue working on my thesis at a critical time when my thesis funding from the ITI became uncertain. In the same way, many thanks to the Science and Engineering Library for giving me a part-time position for a long period of time. Thanks to Dr. Bob Michaelson (Library Head) and Bruno Fast (Supervisor).

I would also like to thank the technical support staff at McCormick, in particular to Rick Mazec, Rebecca Swiertz, and Milos Coric, for helping with the computer issues.

Many thanks to all the administrative staff as well, especially to Pat Dyess and Karen Stove (Mechanical Engineering Department), Betty Modlin (Undergraduate Engineering Office), and Effie Fronimos (Civil and Environmental Department).

Thanks also go to the staff of the Graduate School at Northwestern, in particular to the Associate-Dean Lawrence Henschen, to the Assistant-Dean Pat Mann, and to the student Coordinators Linda Evans, Kate Veraldi, and Antoaneta Condurat.

I want to thank all my friends (graduate students and post-doc fellows), especially to Xiaoqing Jin and Dimtry Epstein for useful discussions on the crack propagation in 3D. A special thanks to Eugene Chez for sharing my thoughts and my problems, and for giving me valuable advice. Thanks to Jay Terry whom I enjoyed our brainstorming and technical discussion. Many thanks to Professor Jean-François Gaillard for providing valuable advice as well.

I particularly want to thank my family: my wife, Nary, and my three children, Laura, Richard, and Kevin. I am glad that my children can now finally read about what I have been doing all these years (Ph.D. thesis and several part-time jobs). They grew up by themselves without seeing regularly their father. Somehow, they turned out to become “honor” students.

Last but not least, my thanks to:

- the Shulls, the Klinkners, the Andersons, the Hartmanns, and the Blair family. They made my family feels at home in Evanston;
- Professor Ted Belytschko for allowing me to come here at Northwestern University (1995) working as visiting scholar. I then changed my mind to stay longer because I wanted to learn more;

- Professor Bill Wilson, my former advisor (MS degree), for teaching me the field of Tribology and Metal Forming process;
- Professor John Rudnicki for allowing me to work with him during my transition period;
- my mother, Ou Yen, who is still alive and live in Paris. She was the only one who still believed in me, when everyone else suggested to give up. My sisters and brothers: Sidy, Denis, Thida, Virginie, and Sudeth, who are always there to help and support. My father, Ouk Khoeun, who passed away in 1977. He first came here in the United States in 1955 on an internship funded by the U.S. government. Back in his home country (Cambodia) in 1956, he enjoyed sharing with us his love and admiration for the United States of America. He died in 1977 by assassination under Khmer Rouge regime. I remember a photo of him from 1955 smiling on top of the Empire State Building. Later, when I came here in 1984 as a tourist, my first stop was the Empire State Building in New York as well. I was impressed by the genius behind the design and architecture of this skyscraper. This probably ignited my passion for the study of heavy structures. Since then, I have had the opportunity to work on the design and analysis of various types of heavy structures, such as oil rig platform offshore (Norway), nuclear power plant (Germany), and welded steel tube forming manufacturing for crude oil transportation in North Sea (France).
- three countries and cultures: Cambodia, France, and the United States of America. I am French educated. I am so grateful for that background. Combined with my American educated, I get the best of both worlds.

Table of Contents

ABSTRACT	3
Acknowledgements	6
List of Tables	16
List of Figures	18
Chapter 1. Introduction	22
1.1. Historical background	22
1.2. Objective and scope	23
1.3. Literature review	25
1.4. Organization of Contents	27
Chapter 2. Statement of the problem	29
2.1. Bridge structure	29
2.2. Pin-Hanger assembly	29
2.3. Load path	33
2.4. “Pack rust” formation	35
2.5. Wear grooves	37
Chapter 3. Finite element modeling	39
3.1. Geometry and model	39

	11
3.1.1. Model validation	40
3.1.2. Geometric dimensions	40
3.2. Finite element procedure	42
3.2.1. Key phases	42
3.2.2. Mesh generation	44
3.2.3. ABAQUS/CAE	44
3.3. Finite element analysis (FEA)	45
3.3.1. Model discretization	45
3.3.2. Material properties	46
3.3.3. Loading	48
3.3.3.1. Mechanical loading	48
3.3.3.2. Thermal load	49
3.3.4. Contact modeling	49
3.3.5. Results	50
3.3.5.1. Checking tension in the hanger against applied load	51
3.3.5.2. Comparing design calculations against FEA predictions	53
3.3.5.3. Stress concentration in hanger plate	54
3.3.5.4. Shear stress in the pin	55
3.3.5.5. von Mises equivalent stress distribution	56
3.4. Concluding remarks	59
Chapter 4. Constitutive equations	61
4.1. Introduction	61
4.2. Elasticity	62

	12
4.3. Equilibrium equation	65
4.4. Thermal strain	66
4.5. Elasto-plastic material behavior	67
4.5.1. Basic concepts	67
4.5.2. Yield condition	69
4.6. Contact modeling	71
4.6.1. Basic concepts	72
4.6.2. Contact capabilities in ABAQUS	72
4.6.3. Friction	73
Chapter 5. Thermal effects on bridge movements	75
5.1. Introduction	75
5.2. AASHTO recommendations and alternative approaches	75
5.3. Temperature ranges	76
5.4. Response to temperature variations	76
5.5. New proposed method	77
5.5.1. Thermal strain	77
5.5.2. Rotational angle	78
5.5.3. Numerical results	80
5.6. Concluding remarks	81
Chapter 6. Operating conditions	82
6.1. Introduction	82
6.2. Locked-up condition	82

	13
6.3. Elastic-plastic behavior	84
6.3.1. Material nonlinearity	84
6.3.2. Defining plasticity in ABAQUS	84
6.3.3. Defining the plasticity curve	88
6.4. Lock-up condition and elastic-plastic response	89
6.5. Concluding remarks	91
Chapter 7. Stress intensity factors for transverse crack in a pin	93
7.1. Introduction	93
7.2. Determination of stress intensity factors	95
7.2.1. overview	95
7.2.2. Stress analysis of cracks	97
7.3. J-integral	100
7.4. Model validation	105
7.4.1. Contour integral evaluation of a simplified 3D model	106
7.5. FEA prediction of the mixed-mode SIFs on operating conditions	108
7.5.1. Unlocked conditions	109
7.5.1.1. Effects of temperature changes	110
7.5.2. Locked conditions	111
7.6. Concluding remarks	113
Chapter 8. Computational modeling of fatigue crack growth	125
8.1. Introduction	125
8.2. Computational procedure for evaluating the crack growth	126

	14
8.3. Crack growth simulation in ABAQUS	126
8.4. Fatigue crack growth	127
8.4.1. Crack growth analysis procedure	128
8.4.2. New contour crack front computations	130
8.4.2.1. New crack front normal positions	130
8.4.2.2. New crack front end-points located on the circle	133
8.4.3. Results	135
8.4.3.1. Prediction of fatigue crack growth	136
8.4.3.2. Initial state or stage no. 1	137
8.4.3.3. Stage no. 2	138
8.4.3.4. Stage no. 3	139
8.5. Concluding remarks	140
Chapter 9. Conclusion and discussion	146
9.1. General discussions and recommendations	146
9.1.1. Crack growth	148
9.1.2. Non-destructive evaluation (NDE)	149
9.2. Future work	149
References	151
Appendix A. Design requirements according to AASHTO	156
A.1. AASHTO code	156
A.2. Design calculations	157
A.2.1. Loading conditions	158

	15
A.2.2. Shear stress in pin	158
A.2.3. Tension in hanger	160
Appendix B. Material selection	163
B.1. NUCu 70W	163
B.2. ASTM A992	164
Appendix C. Pack-rust formation and expansion	166
C.1. Introduction	166
C.2. Corrosion expansion calculation	166
C.2.1. Chemical reaction	167

List of Tables

3.1	Geometric dimensions of the bridge elements	42
3.2	Material properties (ASTM A36)	48
3.3	Comparison of the tension in hanger near the pin hole	53
3.4	Shear stress in the pin	56
3.5	von Mises equivalent stress σ_{eq} in bridge components	59
5.1	AASHTO temperature ranges	76
5.2	Comparison between exact $(\theta)_{EXACT}$ and finite element results $(\theta)_{FEA}$	80
5.3	Elongation vs. temperature	81
6.1	von Mises equivalent stress σ_{eq} (locked condition)	83
6.2	von Mises equivalent stress σ_{eq} (locked)	90
7.1	AASHTO temperature ranges	110
8.1	Determination of ΔK_{eff} and Δa_i along the crack front ($\Delta N = 1$)	138
8.2	New crack front coordinates ($\Delta N = 1$)	139
8.3	Determination of ΔK_{eff} and Δa_i along the crack front ($\Delta N = 15000$)	140
8.4	New crack front ($\Delta N = 15000$)	141
8.5	Determination of ΔK_{eff} and Δa_i along the crack front ($\Delta N = 10000$)	142

		17
8.6	New crack front ($\Delta N = 10000$)	143
A.1	Results for the shear stress in pin and tension in hanger	162
B.1	Material properties (NUCu 70W)	164

List of Figures

2.1	Plan and elevation view of the bridge	30
2.2	Schematic representation of the intermediate span elevation	31
2.3	Typical pin-hanger connection	32
2.4	Section of pin-hanger assembly	33
2.5	Shear planes of the connection	34
2.6	Typical pack rust formation	36
2.7	Shallow defects or wear grooves (Removed pins)	38
3.1	Schematic representation of the intermediate span elevation	39
3.2	Finite element model of the bridge	41
3.3	Different stages of analysis	43
3.4	Linear and quadratic brick elements	46
3.5	Finite element mesh in vicinity of pin-hanger connection	47
3.6	Contour axial stress (S22)	51
3.7	Plot of the tension in the middle of the hanger plate	53
3.8	Tension near the hanger hole	54
3.9	Stress concentration prediction	55

		19
3.10	Axial stress profile across the hanger cross section	56
3.11	von Mises equivalent stress distribution	57
3.12	von Mises equivalent stress near joint connection	58
5.1	Typical pin and hanger connection	79
6.1	Typical pack rust formation	83
6.2	Decomposition of the total strain into elastic and plastic strains	87
6.3	Elastic-plastic material behavior (ASTM A36) used for the computations	89
6.4	Mises stress on the bottom pin: lock up and elastic-plastic material	90
6.5	Tension profile in the hanger plate: lock up and elastic-plastic material	91
6.6	Axial stress in hanger for lock up and elastic-plastic material behavior	92
7.1	Initial crack profile embedded on the pin surface	94
7.2	Initial crack dimensions: $a=6$ mm, $c=13.66$ mm, $D=165.1$ mm	95
7.3	Three basic modes of crack surface displacements	98
7.4	Stress components ahead of crack	101
7.5	Contour for the evaluation of the J integral and crack tip coordinates	102
7.6	Convention at crack tip. Domain A is enclosed by Γ , C^+ , C^- , and C^0	103
7.7	Comparison of computed Mode I stress intensity factors	106
7.8	Mesh for semi-elliptic crack problem	107
7.9	Local deformation near the crack surfaces due to compression (bottom pin)	109
7.10	Definition of local orthogonal coordinates on the crack front: \mathbf{q} , \mathbf{t} , and \mathbf{n}	111

7.11	Initial crack dimensions: $a=6$ mm, $c=13.66$ mm, $D=165.1$ mm	112
7.12	Mixed-mode SIFs (unlocked) for temperature $T = 15^\circ$ C ($T = 59^\circ$ F)	113
7.13	Mixed-mode SIFs (unlocked) for temperature $T = 30^\circ$ C ($T = 86^\circ$ F)	114
7.14	Mixed-mode SIFs (unlocked) for temperature $T = 45^\circ$ C ($T = 113^\circ$ F)	115
7.15	Effective SIF (unlocked), K_{eff} for different temperatures	116
7.16	Mixed-mode SIFs (locked) for temperature $T = 15^\circ$ C ($T = 59^\circ$ F)	117
7.17	Mixed-mode SIFs (locked) for temperature $T = 30^\circ$ C ($T = 86^\circ$ F)	118
7.18	Mixed-mode SIFs (locked) for temperature $T = 45^\circ$ C ($T = 113^\circ$ F)	119
7.19	Effective SIFs (locked) for different temperatures	120
7.20	Comparison between effective SIFs between unlocked and locked conditions	121
7.21	Schematic diagram of the combined loading	122
7.22	Stress contour for a temperature $T=45$ C	123
7.23	Stress contour for a temperature $T=-30$ C	124
8.1	Initial crack profile embedded on the pin surface	127
8.2	Schematic representation of the new crack front	131
8.3	Schematic of the normal positions to the crack front	131
8.4	New crack front end-points located on the circle	134
8.5	Crack surfaces	136
8.6	Deformed mesh showing new contour crack front	144
8.7	Initial crack dimensions: $a=6$ mm, $c=13.66$ mm, $D=165.1$ mm	145

	21
A.1 Shear stress acting on the cross section of a pin	159
A.2 Hanger plate subjected to a tensile load T	161
C.1 Typical pack rust formation	167
C.2 Schematic representation of the corrosion formation	168

CHAPTER 1

Introduction

1.1. Historical background

Bridge pin and hanger assemblies are considered as critical elements whose failure may result in partial or complete collapse of the structure. Some examples of bridge failures are:

- A failed hanger pin initiated the tragic collapse of one span of the Mianus River Bridge in June 1983.
- The nearly catastrophic failure of several pins in a bridge on I-55 in St-Louis, Missouri in January 1987.
- The most recent ones: the Hoan bridge in Milwaukee (December 2000) and the I-35W bridge in Minneapolis (August 2007).

Since 1983, the failure of several pins prompted the Federal Highway Administration (FHWA) to require inspection of all pins and connectors in all bridges throughout the country. More recently, in January 2003, the Paseo bridge in Missouri was suddenly closed to traffic after a strut was found to be fractured. According to the inspection, in reference to the report of the Missouri Department of Transportation (MoDOT) (2005) [1], it was concluded that the damage was likely caused by one of the following reasons: thermal contraction, overstressing, fatigue, and reduction in fracture toughness associated with low temperatures. At that time, temperatures were reported to have hit a record low

of 25°F below zero. Field inspectors found the lower pin was frozen and did not allow for free movement of the superstructure. This example shows the importance of thermal effects due to temperature changes on bridge components.

1.2. Objective and scope

For several decades, ultrasonic inspection has become the primary method of performing a detailed inspection of in-service pin and hanger connections of steel bridges.

In the present study, the emphasis is on the investigation of failure mechanisms in pin and hanger connections using the finite element analysis (FEA). In the present study, two potential failure mechanisms of the pin and hanger connection are considered:

- (1) Due to corrosion and the introduction of corrosion buildup, “pack-rust”, into the mechanism, the connection may partially or fully “freeze” (lock-up), thus inhibiting the free rotation of the joint. This can lead to a large torque on the pin with possible plastic yielding and failure.
- (2) Cycling loading, due to daily and seasonal temperature fluctuations of the pin (in the freely rotating, or partially or fully, frozen conditions), may cause the growth of fatigue cracks and the emergence, in time, of a fatal flaw (with stress intensity factor exceeding the fracture toughness).

Therefore, in order to investigate the effects described above, a series of numerical simulations were carried out. The finite element program ABAQUS (2003) [2] has been used throughout the investigation, which essentially includes stress analysis, thermal effects, determination of the mixed-mode stress intensity factors (K_I , K_{II} , and K_{III}), and

fatigue crack growth simulation. On the other hand, it is important to note that the version of ABAQUS, version 6.4-5 (2003) [2], used in this investigation, does not have crack propagation capabilities in 3D. Therefore, an alternative approach was used. Our current approach consists in creating add-on tools, which combine with the Paris's power law for fatigue crack growth, to be used in conjunction with the ABAQUS program. Fatigue crack growth rates were correlated with the stress intensity ranges.

Since analytical solutions are not available in many cases, especially for 3D problems with complex geometry and loading conditions, a series of validation tests were performed:

- (1) Check the tension in the hanger plate to verify consistency between the applied mechanical load and the corresponding response in the hanger plate. The results obtained show agreement in the tension values.
- (2) Validate the bridge movements (expansion or contraction) due to thermal loading. The comparison shows excellent agreement between the proposed analytical expression and the finite element solution.
- (3) Check the stress concentration around the hole of the hanger plate. Our results agree well with the theoretical result.
- (4) Validate the element selection in crack analysis. Due to the size and the complex geometry of the model, singular elements are difficult to employ. Accordingly, we use 8-node standard hexahedral elements and verify their accuracy and mesh suitability through a benchmark calculation.

In order to simulate the entire bridge structure, in realistic operating conditions, the following models were created: (a) a traffic simulation model which includes dead load and traffic load, (b) a temperature simulation model which includes the temperature

changes according to the American Association of State Highway and Transportation Officials (AASHTO) specifications, and (c) a crack simulation model which includes an initial crack on the cylindrical pin surface. In addition, a final model which includes all the above parameters as well as lock-up of the connection (due to pack-rust) was also created. Results for the first of these cases were obtained for the case of a typical highway bridge and associated pin and hanger geometries and dimensions. These results indicate that the contact algorithms and the thermal aspects of the modeling are correctly implemented and that they give accurate results in validation tests previously mentioned. Results also indicate that when lock up of both the upper and the lower pins occurs, extensive plastic yield develops in the pins and in the hanger. This will render the bridge unsafe for daily use for traffic.

Due to cyclic loading generated by the traffic, the initial crack embedded on the pin surface can grow over a period of time until the crack extends through the pin section. This can lead to catastrophic consequences.

Civil engineers throughout the world accept both system of units: the United States Customary System (USCS) and le Système International d'unités (SI). For that reason, both units are used in the present document.

1.3. Literature review

As mentioned earlier, ultrasonic inspection has become the primary method of performing a detailed inspection of in-service hanger-pins for decades. A literature review has

shown that there is a reasonable amount of information which relates directly to this technique. However, we found relatively few works dealing with pin and hanger connections using numerical simulation.

Among others who used ultrasonic inspection are the work done by Kelsey *et al.* (1990) [3]. Their work is based on testing in-situ. The object of the examination is to detect and locate cracks or excessive wear in the pins and cracks in the hanger straps.

Illinois Department of Transportation (IDOT) issued a technical report (1992) [4], which illustrates methods used in Illinois for analysis, inspection, and repair of pin connections in bridges. “This report documents efforts by the Illinois Department of Transportation (IDOT) to define the problem in Illinois, develop methods to detect pin movement, inspect pins for defects, and develop improved pin connection details”, IDOT (1992) [4].

Walther and Gessel (1996) [5] highlighted the key elements of an effective inspection using ultrasonic testing. They also provided interesting details on how to detect wear grooves. Walther and Gessel indicated that wear grooves are sometimes detected at the shear plane of the pin and may be difficult to distinguish from potential cracks. Based on their observation, such grooves are often rounded and generally continue around the circumference of the pin. They concluded that the use of ultrasonic methods can prove difficult considering the complex geometry of typical pin elements which might include keyways, center bore holes, changes in pin diameters, and threads. Furthermore, wear grooves and acoustic coupling further complicate ultrasonic pin testing.

Later, Graybeal *et al.* (2000) [6], from the Federal Highway Administration (FHWA), investigated different ultrasonic techniques: (1) The first technique involves testing in-service pins using a contact ultrasonic method. This type of inspection would generally

be used during an in-service inspection; (2) The second involves testing of decommissioned pins through a non-contact ultrasonic method using an immersion tank. Although this type of inspection is not practical for field use, it does provide highly repeatable and reliable results that can be used to verify the contact ultrasonic technique on the field. The work described was performed by the staff of FHWA's nondestructive evaluation validation center (NDEVC). They concluded that the results from the immersion tank testing correlated well with the field ultrasonic testing. The defect location and the defect size findings indicate a high level of consistency between the two ultrasonic techniques. In addition to these, Graybeal and co-workers gave a clear and precise idea about the "load path" which travels from the applied load location through the connection. The same load path has been used in our numerical simulation model.

Prior to this study, there were not many examples of 3D crack growth work on cylindrical pin with transverse crack. Furthermore, moving and combined loads due to multibody contacts had not been considered in these previous analyses. The absence of closed-form solutions add to the list of difficulty during the investigation.

1.4. Organization of Contents

The historical background, objective, and literature review are discussed in this Chapter. The statement of the problem, which includes the description of the original geometry of the bridge and its critical components are described in Chapter 2. In Chapter 3, we present the first finite element stress analysis of the model. We will also include the validation tests of the 3D model. A key goal was also to relate original design calculations for the pin and hanger components to the current analysis which accounts for the entire

bridge structure under combined loads and extreme environmental conditions. Therefore, the results obtained from the finite element computations are checked against the design calculations provided by the Wisconsin Department of Transportation (WisDOT). In Chapter 4, the constitutive equations for linear elastic and elastic-plastic behavior of the materials are recalled and presented. Also, as we mention previously, in Chapter 5, a new proposed analytical expression for thermal bridge movements is introduced. The “operating conditions” are highlighted in Chapter 6. The mixed-mode stress intensity factors (K_I , K_{II} , and K_{III}) are discussed in Chapter 7. In Chapter 8, we have established a framework for assessment of structural integrity and fatigue life of pin and hanger connections. Conclusions are presented in Chapter 9.

Appendix A illustrates original design calculations as well as corresponding AASHTO specifications. The design computations were performed by a consulting company (Ayres and Associates Co.) in 1954, before the construction of the bridge was launched. The material selection is discussed in Appendix B. The list contains new types of materials with high-performance and corrosion resistance, which meet the requirements of the structural steel ASTM A36 currently used here in this investigation. In Appendix C, we present a method on how to estimate the rate of corrosion expansion and show the origin of its development through electrochemical reaction.

CHAPTER 2

Statement of the problem

2.1. Bridge structure

The bridge studied for this research project consists of 3 spans and is 610 feet long (186 meters). The bridge is located in the Midwest and was built in 1955. An overall view of the bridge elevation is given in the Figure 2.1.

The whole structure is composed of three long spans: two *anchor* spans and an *intermediate* span. The pin and hanger connections are located in the intermediate span. The deck structure over the river consists of parallel haunched girders. The girders are haunched with a depth of 8 feet 14 inches (2.44 meters) at middle-span and deeper over the piers.

According to the elevation plan, as depicted in Figure 2.1, the middle span, in which the critical components such as hinge connections and pin and hanger connections are located, is measured of 244 ft (74.4 m) long. A schematic representation of the intermediate span is shown in Figure 2.2.

As shown in Figure 2.2, the intermediate span consists of a suspended span and is supported by a cantilevered span on each side.

2.2. Pin-Hanger assembly

Fundamentally, a pin-hanger assembly performs much in the same way as a bearing in that it is designed to accommodate both translation and rotation and transmit vertical

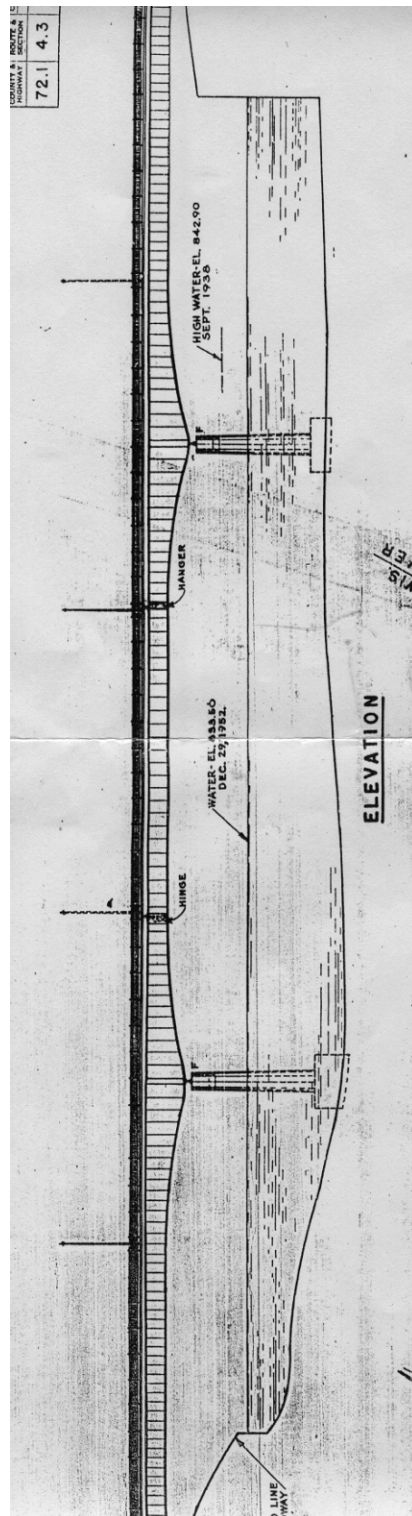


Figure 2.1. Plan and elevation view of the bridge

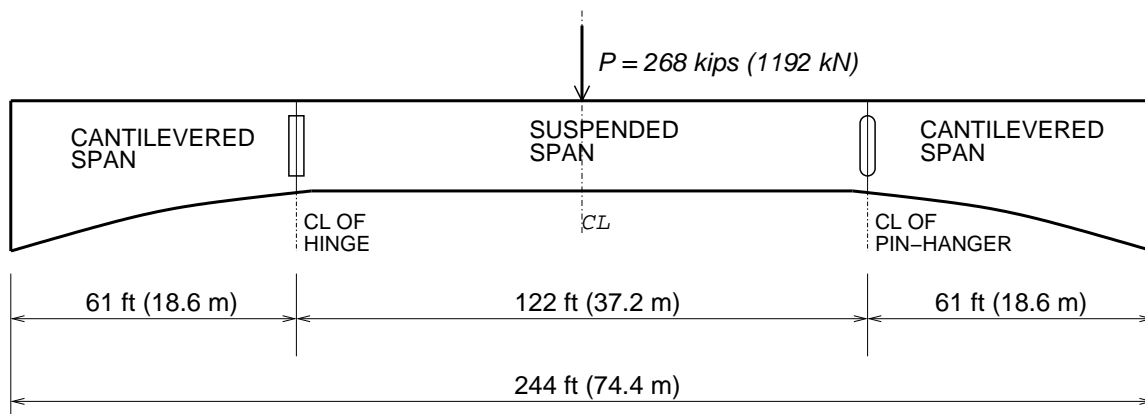


Figure 2.2. Schematic representation of the intermediate span elevation

and horizontal loads. Translation is facilitated through the ability of both top and bottom pins to rotate.

For short span bridges, the use of a pedestal built into the supporting beam can be used since there will be minimal movement. Longer span bridges, however, demand a more robust connection to account for the necessary translation and rotation at the joint (Tonias *et al.* 2007 [7]).

The pin-hanger arrangement allows for load transfer without excessive stress concentration. Similar arrangements can be found in other engineering applications as well; e.g. aircraft engines and wings.

The assemblies consist of an upper pin in the cantilever arm and a lower pin in the suspended span connected by two hangers, one on either side of the web (Figures 2.3 and 2.4).

As previously mentioned, the primary function of a pin-hanger connection is to allow for longitudinal thermal expansion and contraction in the bridge structure. As such, it is designed to move freely in response to traffic and thermal movements, and is assumed to

be torsion-free. This assumption may be valid when the bridge is “new”. After years of exposure to atmospheric environments (deicing salts and load variations), corrosion and wear tend to produce at least a partially fixed (or locked up) condition. Note that a new method of detecting relative movement or rotation is developed and presented in Chapter 5.

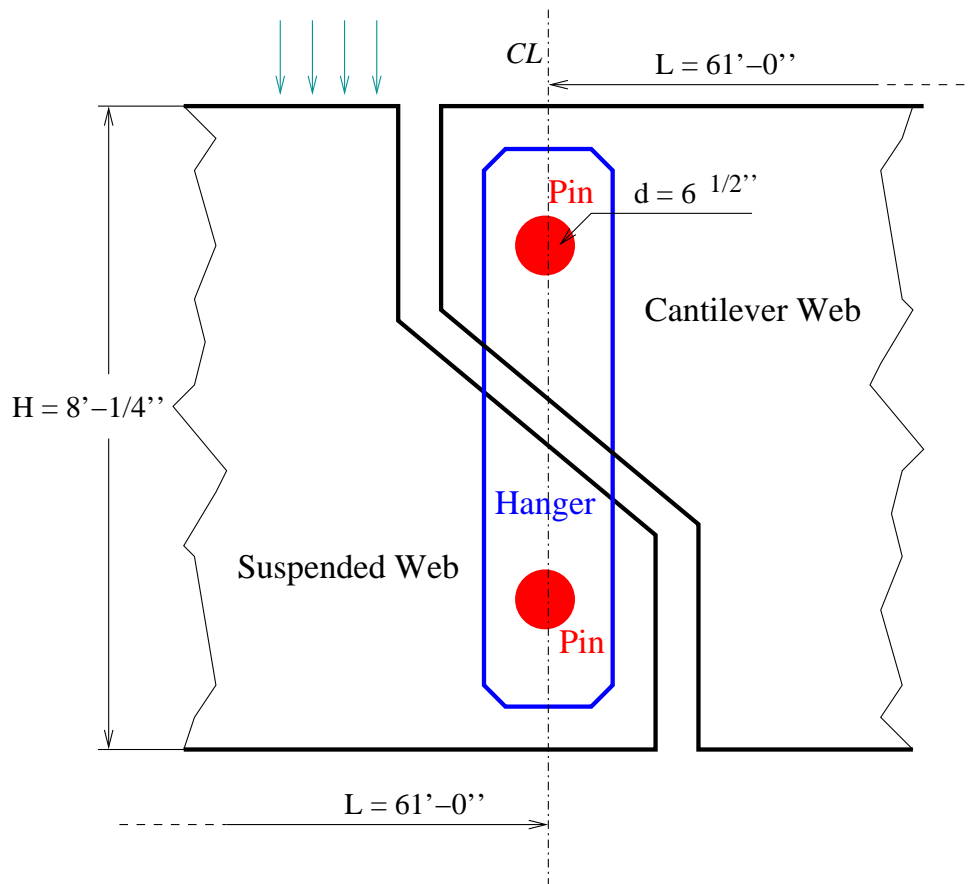


Figure 2.3. Typical pin-hanger connection

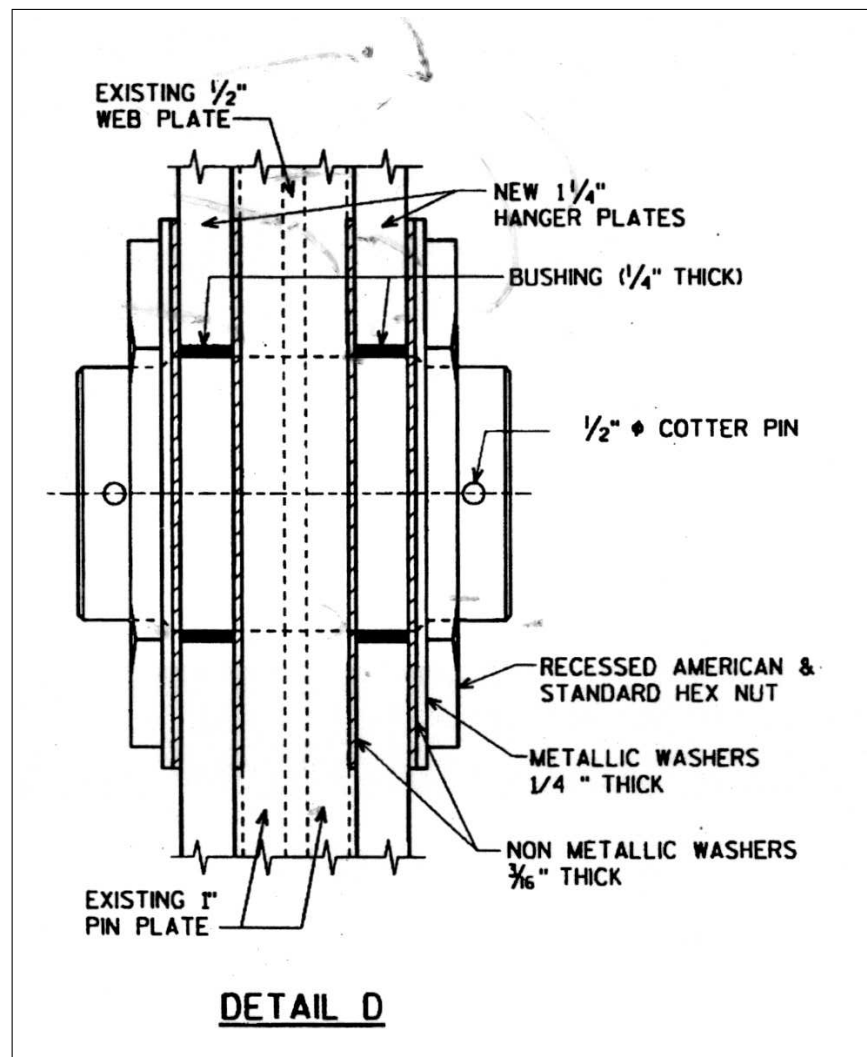


Figure 2.4. Section of pin-hanger assembly

2.3. Load path

According to Graybeal *et al.* (2000) [6] of the Federal Highway Administration (FHWA), loads from the suspended span are transmitted into the cantilever span as follows (see Figure 2.3).

- The loads travel from the suspended girder web to the lower pin, and then into the hanger plates.
- From the hanger plates, the loads are transferred into the upper pin, and finally into the cantilevered girder web.

These connections are designed to support the transfer of shear forces from the suspended span into the cantilever span.

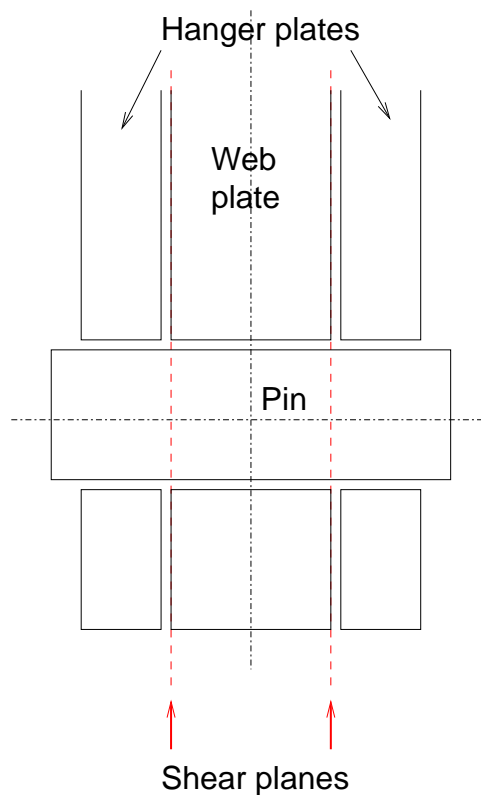


Figure 2.5. Shear planes of the connection

The *load path*, mentioned above, creates two shear planes within each pin, as illustrated in Figure 2.5, one at each of the intersection of the web plate and the hanger plate. If

a pin fails along shear planes, the portion of the bridge section suspended by that pin would be unsupported.

The inclusion of hinges (Figure 2.2), as back up joint assemblies, will help as an alternative load paths and redundancy. This means that if a pin-and-hanger assembly failed, the assembly (hinge connection) could provide an alternative load path.

2.4. “Pack rust” formation

The joint assemblies are in general located directly beneath bridge deck expansion joints. Consequently, they are often exposed to water and debris that falls through the joints. Water and debris can accumulate behind the hanger plate and around the pins. Moreover, the presence of moisture in the confined region between the hanger plates and girder web can lead to an expansion or packing of rust flakes caused by corrosion, also called “pack rust”. Furthermore, due to gravity, as depicted in Figure 2.6, moisture falls to the lower pin and it tends to lock-up first. Also, in Appendix, we present a method on how to estimate the rate of corrosion expansion.

In most cases, the pack-rust can have two detrimental effects on the pin, [6]:

- First, the cross-section of the pin can decrease because of corrosive section loss. In addition, the corrosion can produce pitting that may act as crack initiation sites.
- Second, pack-rust can effectively *lock* the pin within the connection, so that no rotation about the pin is permitted. This can lead to large torsional stresses, which may produce a likely location for the development and propagation of cracks and the eventual failure of the pin.

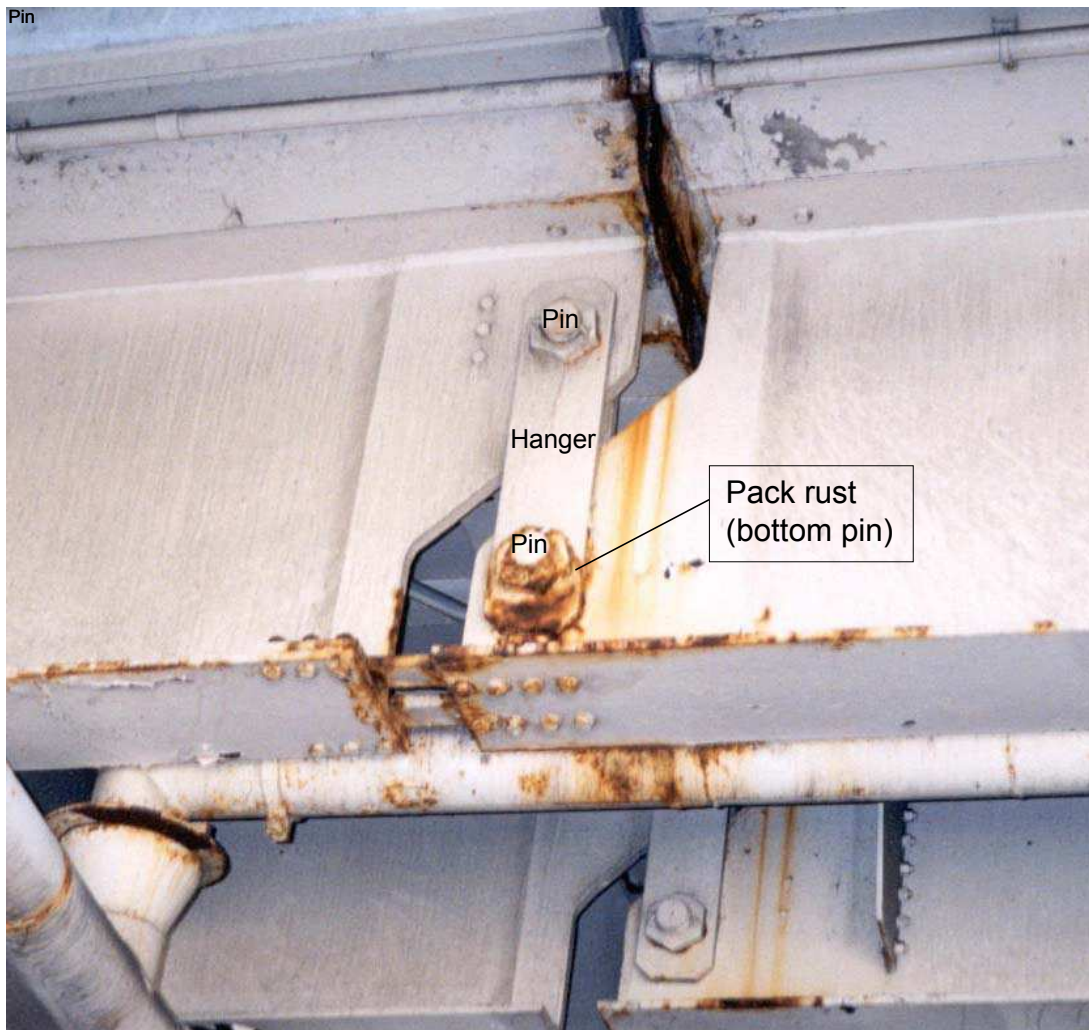


Figure 2.6. Typical pack rust formation

On the other hand, locating cracks that initiate on the pin barrel at the shear perimeter is a difficult task. The shear plane is not visible unless the pin is removed from the connection, as shown in Figure 2.7, (Graybeal *et al.*, 2000 [6]). This operation is labor and equipment intensive.

As shown in the previous picture (2.6), pack-rust is a thick build-up of corrosion product that tends to develop between the surfaces of closely joined and unprotected metal parts (unpainted joints, for example), in particular in older or aging structures.

According to our calculation (see Appendix C for details), the volume of rust produced by corrosion is about 3.5 times that of the parent metal; i.e., full corrosion of 1/4 inch of metal will cause about 1 inch of pack rust.

2.5. Wear grooves

As indicated by Graybeal *et al.* (2000) [6], the combined results of the ultrasonic testing and visual examination revealed shallow defects in some of the pins and no defects in the hanger links. In general, these shallow defects were reported as wear grooves or corrosion section loss having depth ranging from minimal to 3mm (1/8in.). Pins with wear grooves on the surfaces are illustrated in Figure 2.7.



Figure 2.7. Shallow defects or wear grooves (Removed pins)

CHAPTER 3

Finite element modeling

3.1. Geometry and model

A schematic representation of the intermediate span elevation is illustrated in Figure 3.1.

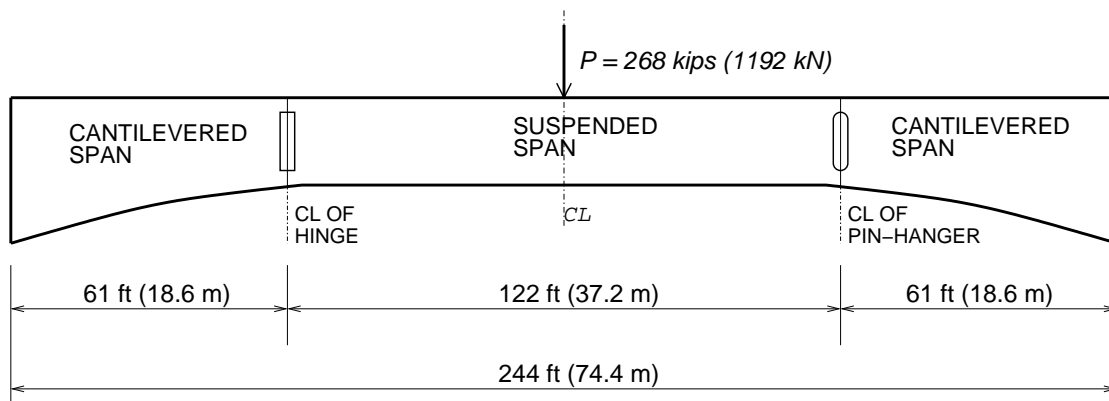


Figure 3.1. Schematic representation of the intermediate span elevation

With a reasonable approximation, the symmetry of the model is taken in the middle of the *intermediate* span. With this as a boundary condition, only the right half of the structure (which contains pin-hanger assembly) needs to be considered. In addition, due to the pier support, the boundary condition on the right pier (cantilever span) is taken to be a built-in support. Finally, the third boundary condition is taken in the z -direction (1/2 web girder). Since the model is symmetric with respect to $x - y$ plane and $y - z$ plane, only 1/4 of it needs to be discretized.

Detailed simulations of the bridge structure, which consists of a suspended span, a cantilever span, and a complete set of elements of the joint connection, were carried out with the ABAQUS finite element program [2].

The finite element mesh of the bridge model is shown in Figure 3.2.

3.1.1. Model validation

Since analytical solution are not available in many cases, especially for this 3D problem with complex geometry and loading conditions, a series of model validation tests are performed:

- Check tension versus applied load
- Verify stress concentration near the hole
- Validate tension versus design calculation

The corresponding results will be shown later in this Chapter.

3.1.2. Geometric dimensions

The geometric dimensions of the bridge elements are summarized in Table 3.1. The units of dimension and force are consistent. Every data in this report are given in both, the United States Customary System (USCS) and the Système International d'Unités (SI). The USCS is generally given first, followed by the SI value in parentheses. Thus, if the USCS unit is 61 ft, it will be expressed as 61 ft (18.6 m).

Note that all dimensions are given in meters (SI units) for the computations. Consequently, the outputs are automatically displayed with SI units. For convenience, we will convert, if necessary, the solution data from SI units to USCS units.

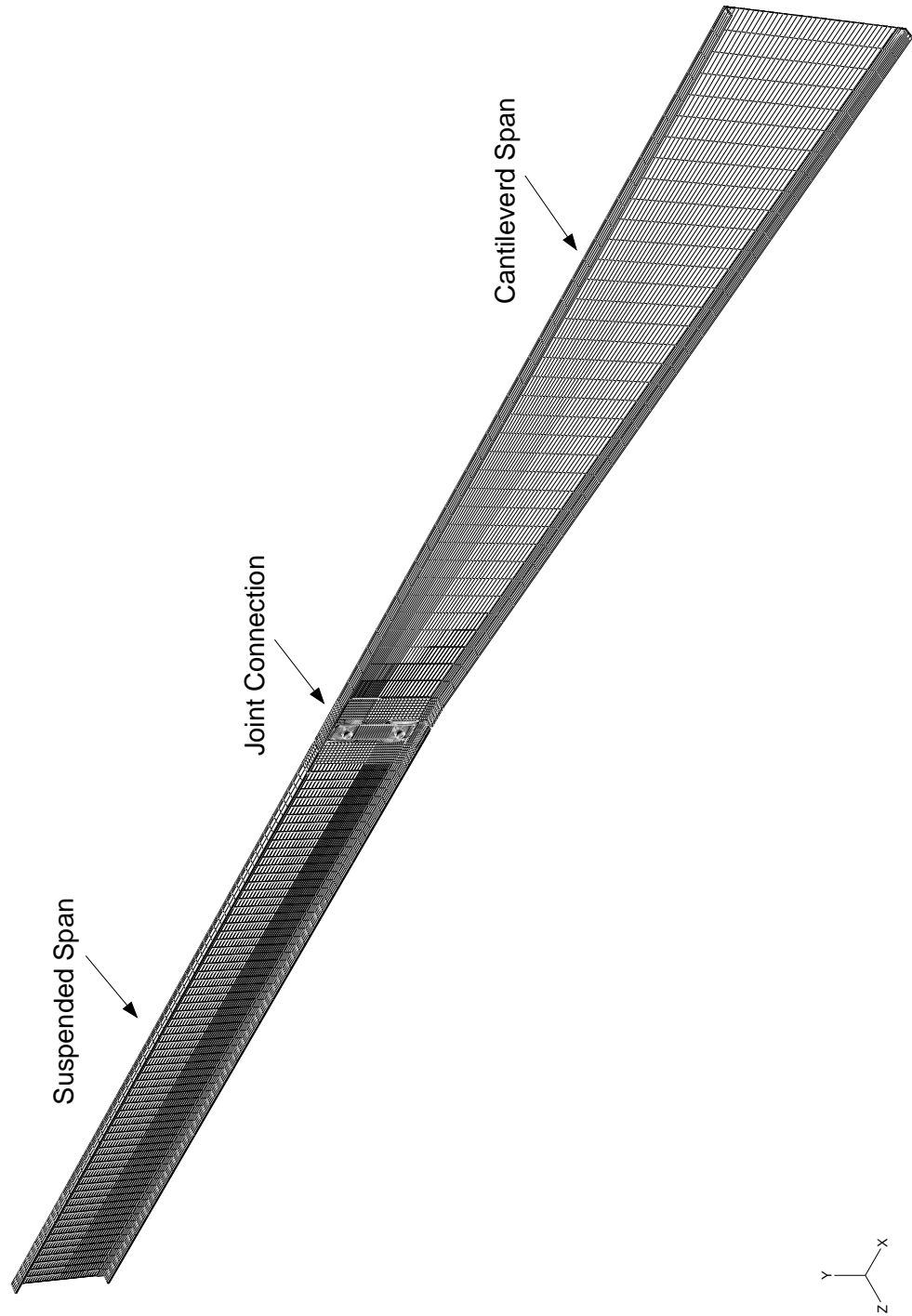


Figure 3.2. Finite element model of the bridge

Table 3.1. Geometric dimensions of the bridge elements

Components	UCSC units	SI units
Intermediate span	$L = 244$ ft	$L = 74.4$ m
Cantilever span	$L = 61$ ft	$L = 18.6$ m
Suspended span	$L = 122$ ft	$L = 37.2$ m
Web height	$H = 8$ ft 1/4 in	$H = 2.4$ m
Web thickness	$t = 0.5$ in	$t = 0.0127$ m
Pin diameter	$d = 6.5$ in	$d = 0.1651$ m
Hanger thickness	$t = 1.25$ in	$t = 0.03175$ m
Hanger width	$w = 1$ ft 4 in	$w = 0.4064$ m
Hanger length	$l = 6$ ft 5 1/4 in	$l = 1.9621$ m
Distance between pins	$l = 4$ ft 4 in	$l = 1.3208$ m
Pin-plate thickness	$t = 1$ in	$t = 0.0254$ m

3.2. Finite element procedure

Before we show the FEA results, it seems important to recall the main sequences of steps involving the numerical simulations.

3.2.1. Key phases

In general, the FEA procedure involves three key phases:

- A *pre-processing* phase
- An *analysis* phase, and
- A *post-processing* phase.

The three phases are illustrated in Figure 3.3.

Perhaps the most time consuming of the three phases is the *pre-processing* phase. After making reasonable assumptions with appropriate boundary conditions, one must choose suitable types of finite elements and create a finite element mesh that is sufficiently refined

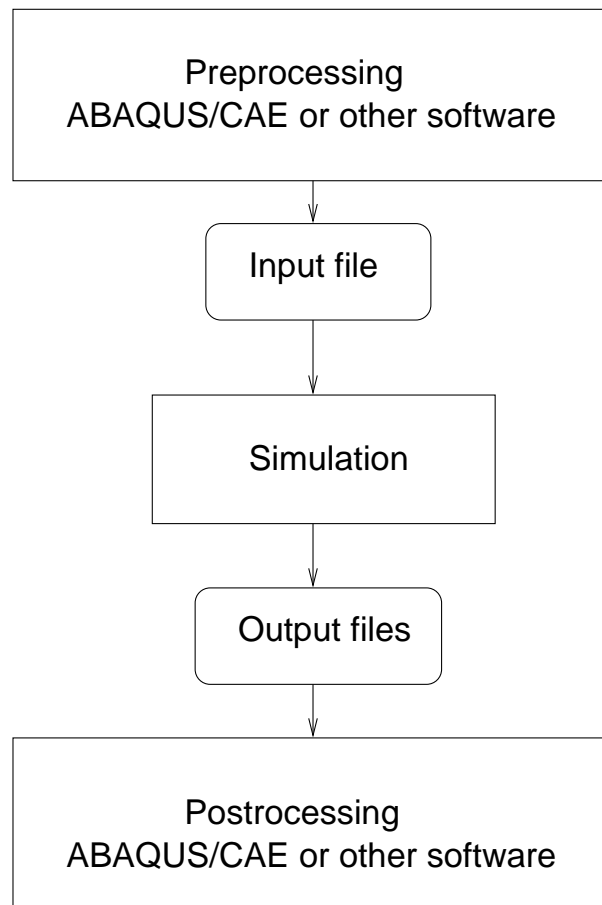


Figure 3.3. Different stages of analysis

in regions where high stress distribution is expected; i.e. the connection areas between joint components.

For the most part, the *analysis* phase is straightforward. However, in the final phase, one faces the difficult task of interpreting the results of the analysis. The *post-processing* phase has been made easier through post-processing software. In addition, at this stage, one must assess whether or not the “nice-looking” contour plots make sense. In particular, one must be able to answer questions such as: Are the boundary conditions satisfied? Is the finite element mesh sufficiently refined? Is the assumption of linear material behavior

appropriate? Are the applied loads accurate? etc. Other sources of information include Cook *et al.* (2002) [8], Gosz (2006) [9], and ABAQUS (2003) [2].

3.2.2. Mesh generation

As mentioned above, mesh generation by itself is a time consuming process. With the arrival of modern pre-processing software, the amount of time spent in the pre-processing phase has been significantly reduced.

For example, the geometric model of each component covered by this study necessitates the use of an automatic mesh generator (pre-processing program). This must be capable of producing fine elements near the assemblies where the stress gradients are changing very rapidly, and coarser elements in regions where the stresses are more evenly distributed. The elements should not be excessively elongated or distorted, [2].

3.2.3. ABAQUS/CAE

ABAQUS/CAE provides a complete modeling (pre-processing) and visualization environment (post-processing) for ABAQUS analysis products. Here, CAE stands for “Complete ABAQUS Environment”, not to be confused with “Computer Assisted Engineering”, a term commonly employed in the field of design and simulation. The ABAQUS suite consists of three core products: ABAQUS/CAE, ABAQUS/Standard, and ABAQUS/Explicit.

ABAQUS/CAE provides a consistent interface for creating finite element model for ABAQUS solver (Standard or Explicit). It produces a data file (called model database) for immediate analysis by the solver. For example, ABAQUS/CAE has been used here to build a complete bridge model.

ABAQUS/CAE is divided into modules, where each module defines a logical aspect of the modeling process. For example, defining the *geometry*, defining *material properties*, and generating a *mesh*. As we move from *module* to *module*, we build the model from which ABAQUS/CAE generates an *input file* that we then submit to the *solver*. Finally, we use the *visualization* module to view the results of our analysis.

Here, the bridge model is organized as a collection of individual parts, also called *instances*, connected together to form a one piece of structure. We then position those instances relative to each other in a global coordinate system to form the *assembly*. We can create and position multiple instances of a single part; e.g. we can create multiple instances of a single part of pin (upper and lower pins). In addition, we can assemble instances of deformable parts; e.g. hanger, webs, pins, when we are solving contact problems. When we modify a part, ABAQUS/CAE automatically regenerates all instances of the modified part in the assembly.

For further details, one can refer to ABAQUS documentation (2003) [2].

3.3. Finite element analysis (FEA)

3.3.1. Model discretization

All structural components (web girders, pins, hanger, and reinforcement plates) are modeled 8-node standard brick reduced-integration elements (known as C3D8R in the ABAQUS element library). The entire model consists of about 31,000 elements. The density of the mesh increases toward the centers of the connections where most of the deformation occurs.

Since the problem involves *contact interactions* between different components, also known as 3D multi-body contacts, first order brick elements are the best choice for this type of problem. In addition, reduced-integration elements are used, because among other considerations, it decreases the analysis cost, and provides reasonable accuracy on stress prediction, [2]. Figure 3.4 illustrates typical brick elements: linear and quadratic elements.

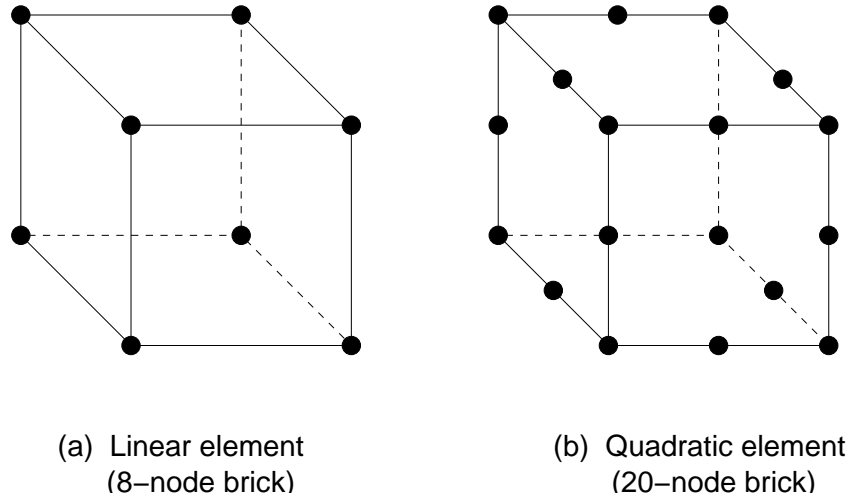


Figure 3.4. Linear and quadratic brick elements

Figure 3.5 shows the discretization in the vicinity of the joint connection which is the region of interest. Note that the mesh is finer toward the vicinity of the contact surfaces where the stresses are highest.

3.3.2. Material properties

We assume that the entire bridge is made of the same construction material (ASTM A36). A Young's modulus of $E = 29 \times 10^6$ psi (200 GPa) and a Poisson's ratio of $\nu = 0.3$ define the elastic response of the material. The initial yield stress is $\sigma_Y = 36$ ksi (248 MPa)

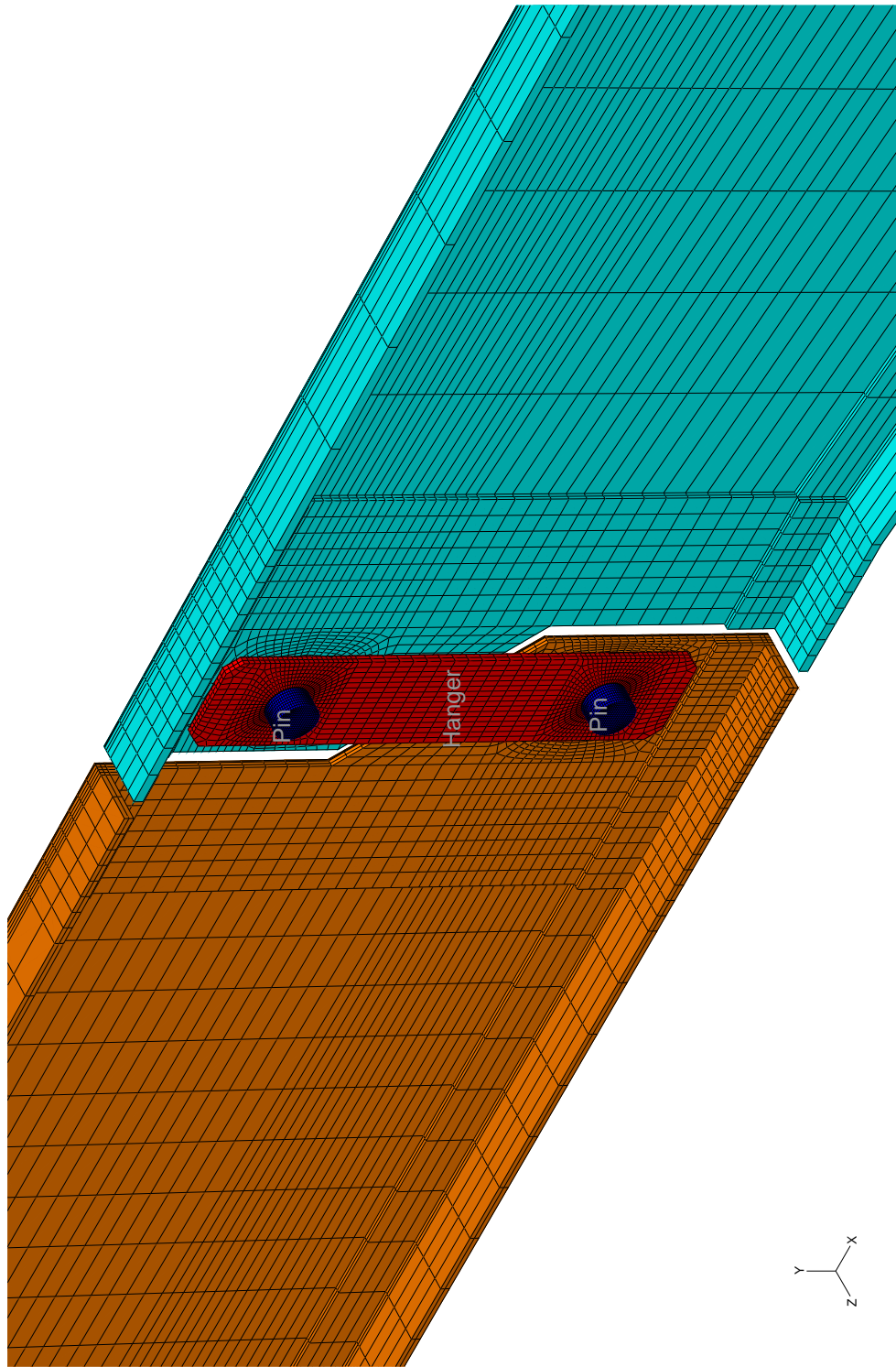


Figure 3.5. Finite element mesh in vicinity of pin-hanger connection

and the ultimate tensile strength of $\sigma_{UTS} = 58$ ksi (400 MPa). The coefficient of thermal expansion is $\alpha = 6.5 \times 10^{-6}/^\circ\text{F}$ ($\alpha = 11.7 \times 10^{-6}/^\circ\text{C}$). These values are recapitulated in Table 3.2.

Table 3.2. Material properties (ASTM A36)

Material	σ_Y		σ_{UTS}		$\alpha (\times 10^{-6})$	
	ksi	MPa	ksi	MPa	/°F	/°C
ASTM A36	36	248	58	400	6.5	11.7

3.3.3. Loading

3.3.3.1. Mechanical loading. According to the document provided by the Wisconsin Department of Transportation (WisDOT) (1999) [10], it was estimated that the total load for one girder, which includes *dead load*, *traffic* and *impact*, is equal to 268,000 lbf (121,563 kgf).

$$\begin{aligned}
 P &= DL + (LL + I) \\
 &= 197,000 \text{ lbf} + 71,000 \text{ lbf} \\
 &= 268,000 \text{ lbf} \\
 &= 268 \text{ kips}
 \end{aligned}$$

where DL , LL , I are *dead load*, *live load*, and *impact* respectively. Therefore,

$$DL = 197 \text{ kips}$$

$$LL + I = 71 \text{ kips}$$

In this model, the dead load is approximately 3 times the live load and impact. Note that the design calculations can be found in Appendix A.

As a result, an analysis of the bridge under the design external load of 268 kips (1192 kN) was carried out. The load was applied at the top of the suspended web girder at the pin-hanger connection, which is known as the critical location for the bridge structure. We recall here the *load path* described in the previous Chapter. As a result, we apply the same load path for the FEA computations.

3.3.3.2. Thermal load. A new and simple method is proposed to evaluate the bridge movements due to temperature changes. We present an analytical expression and the comparison with the corresponding finite element solution. We will discuss this in detail in Chapter 5.

3.3.4. Contact modeling

The contact analysis was performed using the *contact pair* approach in ABAQUS. Contact pairs, named as *master* and *slave* surfaces define surfaces which can potentially come into contact. In the present study, the contact is modeled by the interaction of contact surfaces defined by grouping specific faces of the elements in the contacting regions. Here, surface-to-surface contact is defined between:

- the suspended web-girder and the lower-pin,
- the lower-pin and the bottom-hole of the hanger plate,
- the top-hole of the hanger plate and the upper-pin, and
- the upper-pin and the cantilever span.

Thus, 4 multi-body contacts were defined to describe the deformable surfaces in 3D.

Normal pressure will be transmitted through the contact pairs. In ABAQUS, contact can occur in the form of *small sliding* or *finite sliding*. Analyses performed in this work used the small sliding option, in which surfaces are allowed to undergo finite separation and sliding. Contact surface tractions were calculated assuming that the surfaces are perfectly *hard*, which means that there will be no penetration of surfaces into one another. Contact tractions were defined by local basis system formed by the normal to the master surface.

To perform the first series of simulations (stress analysis), a coefficient of friction $\mu = 0$ is used between all contacting surfaces which correspond to the *unlocked* (unfrozen) condition.

In addition, the analyses were performed using small-displacement theory. The only nonlinearities in the problem are the result of changing conditions due to contact interactions.

3.3.5. Results

We investigate here several different approaches to simulate the pin and hanger connections. In addition, the analysis is first performed by assuming a linear elastic material behavior and frictionless contacts, i.e. unlocking scenario. This simple material model would probably suffice for routine design.

We have mentioned before the need for the validation of our finite element model. This is mainly due to the complexity of the geometry and boundary conditions. Therefore, a series of validation tests were performed. These include:

- Check the tension in the hanger plate if there is consistency between the applied mechanical load and the corresponding tension in the hanger plate.

- Compare the results between the design calculation and the finite element analysis prediction (near the connection).
- Check the stress concentration in the hanger plate.

3.3.5.1. Checking tension in the hanger against applied load. First, we check the tension in the hanger versus the applied load (Figure 3.6). Axial loading is a load passing through the body of the hanger plate. This is the type of load when the plate is designed. We assume that there is no friction between components in the joint assemblies. Based on that assumption, we should obtain the same amount of applied load and tension (or axial stress) in the hanger plate. Note that the axial stress S22 (or σ_{22}), as depicted in

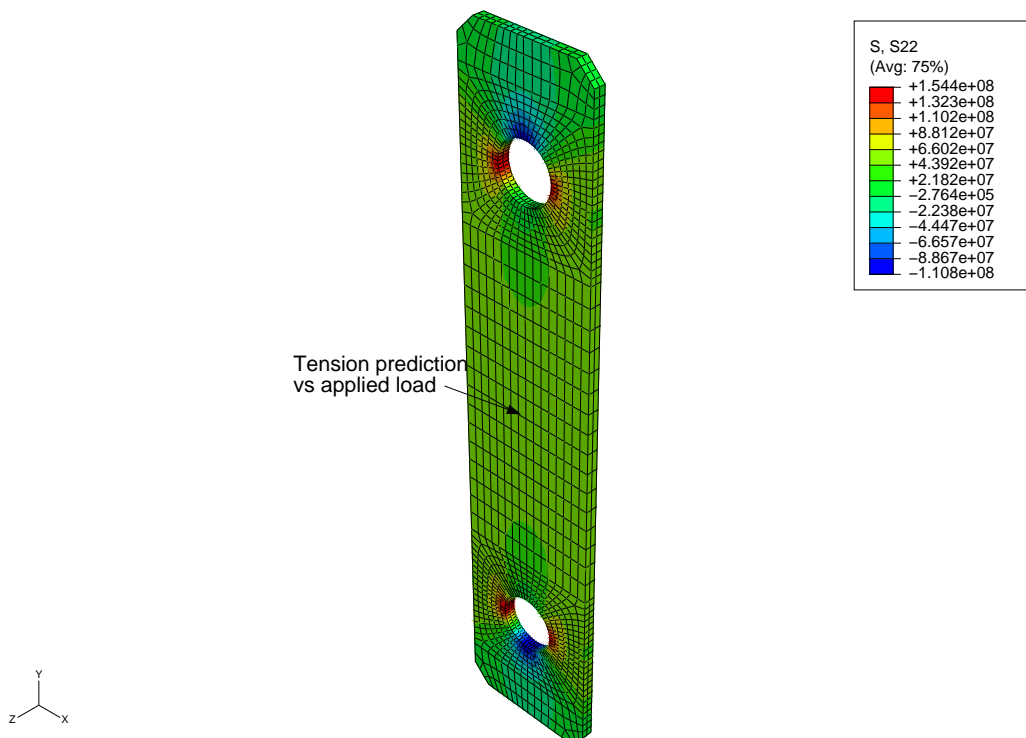


Figure 3.6. Contour axial stress (S22)

Figure 3.6, is expressed in Pascals (SI units). In order to convert to kilopound per square inch (kips), we need to perform the following steps.

According to the FEA prediction, as depicted in Figure 3.7, the averaged axial stress σ_{22} (or S22) is:

$$\begin{aligned}\sigma_{22} &= 46.2 \times 10^6 \text{ Pa} \\ &= 6.70 \text{ ksi}\end{aligned}$$

The cross sectional area (A) of the hanger plate is

$$\begin{aligned}A &= 16 \text{ in} \times 1.25 \text{ in} \\ &= 20 \text{ in}^2\end{aligned}$$

Therefore, the tension in the hanger is

$$\begin{aligned}t &= \sigma_{22} \times A \\ &= 6.70 \times 20 \\ &= 134 \text{ kips}\end{aligned}$$

Note that the applied load was $P = 134$ kips. Here, the result of our computation for the tension in hanger is $t = 134$ kips. Therefore, an excellent agreement was obtained. Consequently, the first model validation is checked.

It is clear, by the results presented, that our FEA model with current boundary conditions and 8-node brick elements (with reduced-integration) provide sufficient accuracy.

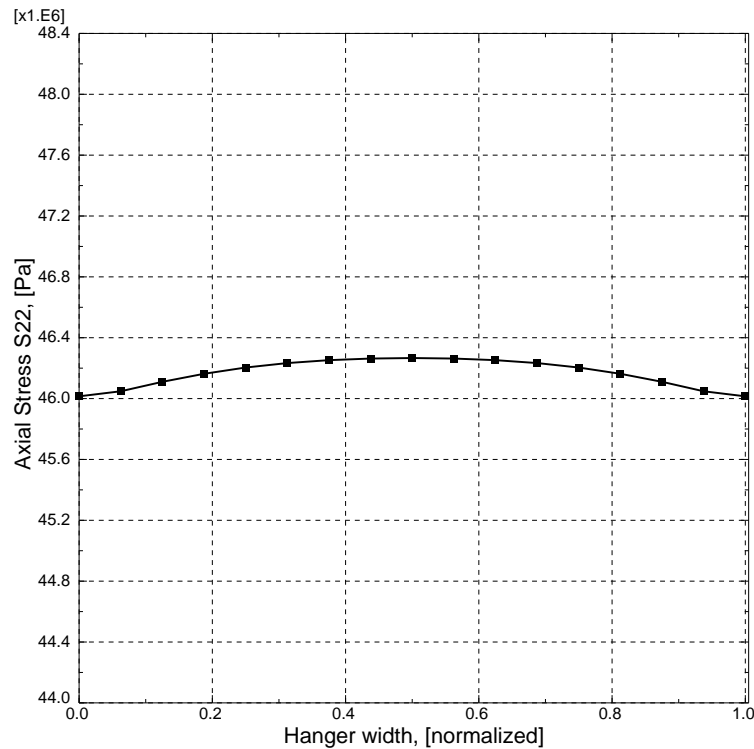


Figure 3.7. Plot of the tension in the middle of the hanger plate

3.3.5.2. Comparing design calculations against FEA predictions. Because stress concentrations occur at the hanger holes, the net section of the hanger plate across the hanger hole is the critical section for carrying load. The solutions are summarized in Table 3.3. It shows the results which compare the design calculations, the corresponding data provided by the American Association of State Highway and Transportation Officials specification, AASHTO (1996) [11], and the finite element analysis (FEA) solutions.

Table 3.3. Comparison of the tension in hanger near the pin hole

Stress	DESIGN		AASHTO		FEA	
	ksi	MPa	ksi	MPa	ksi	MPa
Tension in Hanger	12.43	85.70	27.72	191.12	11.63	80.20

As the results show, an excellent agreement is found between the design calculations (12.43 ksi) and the FEA prediction (11.63 ksi). The design data is slightly more conservative. The relative error is less than 7%. The FEA data (11.63 ksi) were obtained by taking the average of the tension near the hanger hole (Figure 3.8). Accordingly, we found that both design calculations and finite element solutions are far below the maximum allowable stresses (27.70 ksi) dictated by the AASHTO recommendations.

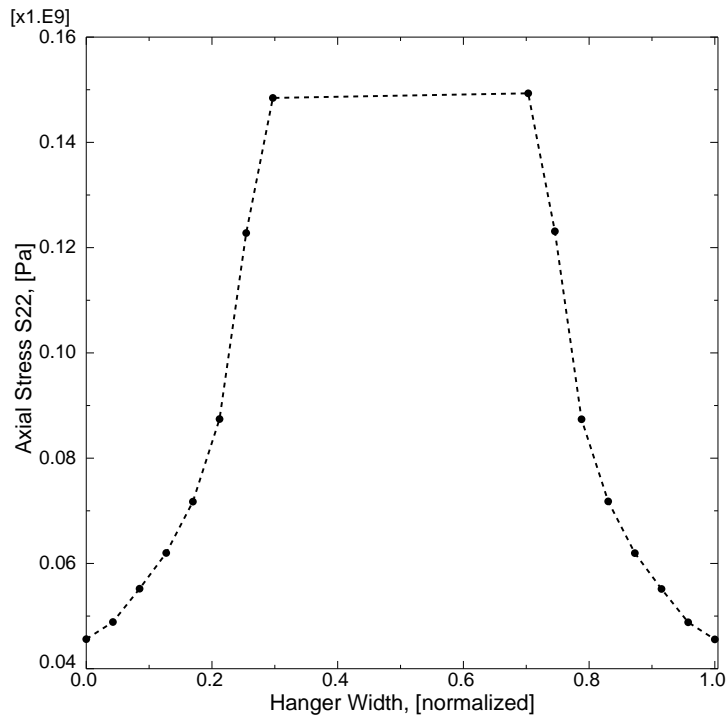


Figure 3.8. Tension near the hanger hole

3.3.5.3. Stress concentration in hanger plate. Consider the circular hole (on top of the hanger plate), as illustrated in Figure 3.9, it is known that the local tangential stress at the edge of the hole is at least three times the applied far-field stress. Here, we found that the stress concentration near the hole is 3.27 times higher than the far-field axial

stress (see Figures 3.10 and 3.9). Therefore, the FEA results confirm the accuracy of the computations when compared with analytical solution (a stress concentration greater than 3.0 is to be expected because of the effect of the pin in the hole).

In addition, Figure 3.10 shows the axial stress profile across the section of the hanger width. As indicated by this profile, the magnitude of this localized stress diminishes with distance away from the hole.

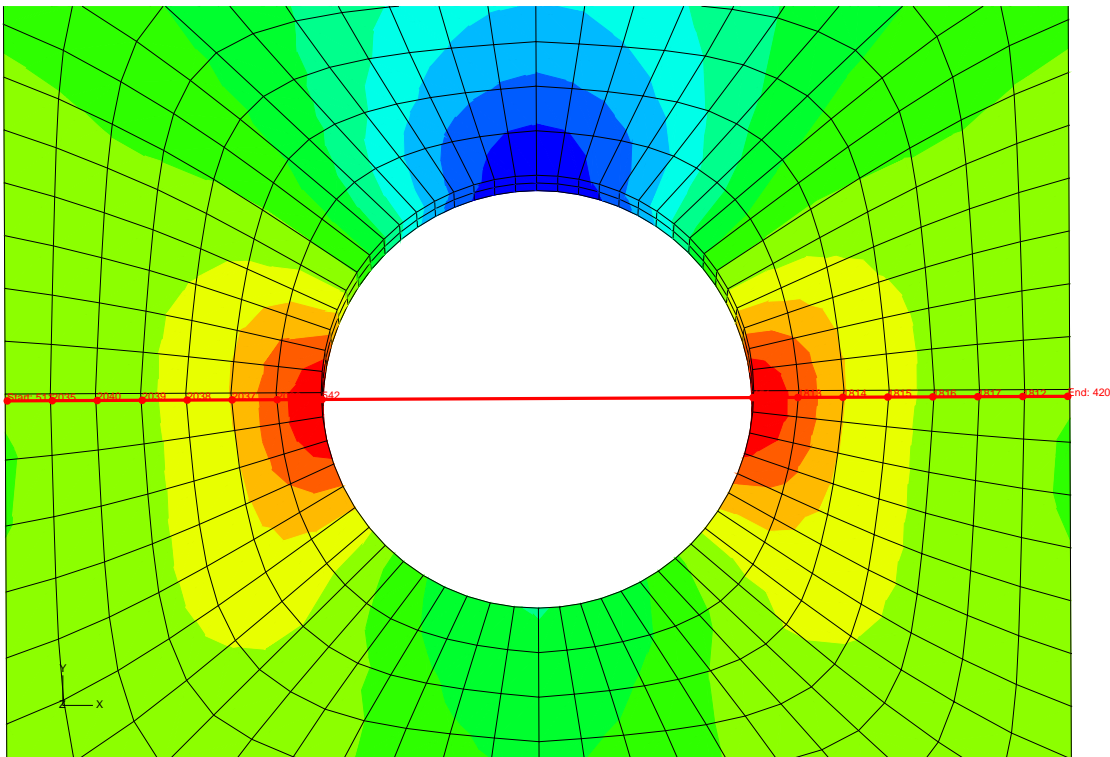


Figure 3.9. Stress concentration prediction

3.3.5.4. Shear stress in the pin. There is another verification recommended by AASHTO, which is to verify the maximum allowable shear stress in the pin. Table 3.4 summarizes the results by comparing shear stress values. We found that the design calculation (average

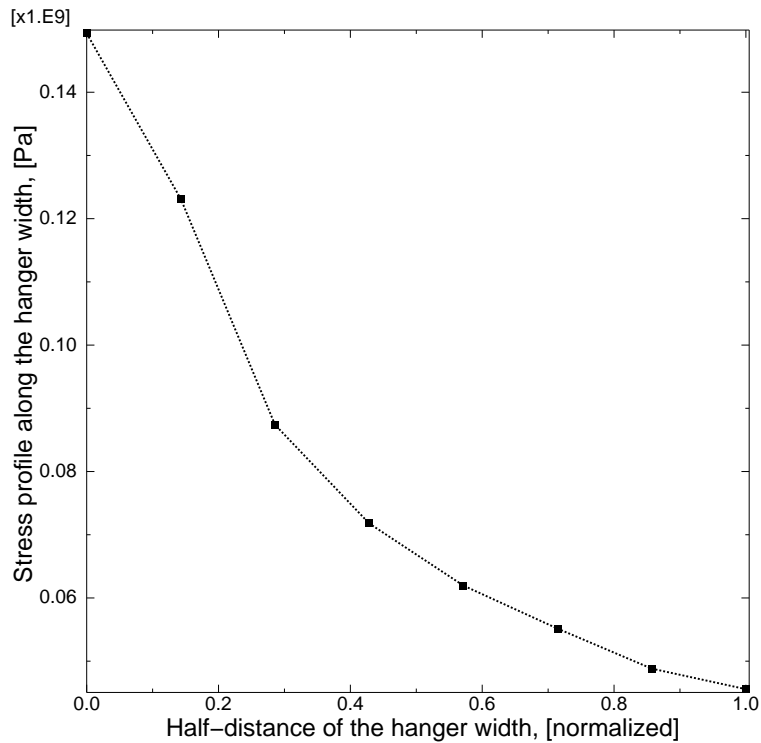


Figure 3.10. Axial stress profile across the hanger cross section

shear) and finite element prediction (maximum shear) are below the maximum allowable stress dictated by the AASHTO recommendations.

Table 3.4. Shear stress in the pin

Stress	DESIGN		AASHTO		FEA	
	ksi	MPa	ksi	MPa	ksi	MPa
Shear in Pin	4.04	27.85	14.40	99.28	8.37	57.73

3.3.5.5. von Mises equivalent stress distribution. Table 3.5 recapitulates the FEA results of the von Mises equivalent stresses (σ_{eq}) in each component of the assembly. These values are then compared to the yield stress, σ_Y , of the materials (ASTM A36). Stress levels in the pin and hanger are below yield, as expected.

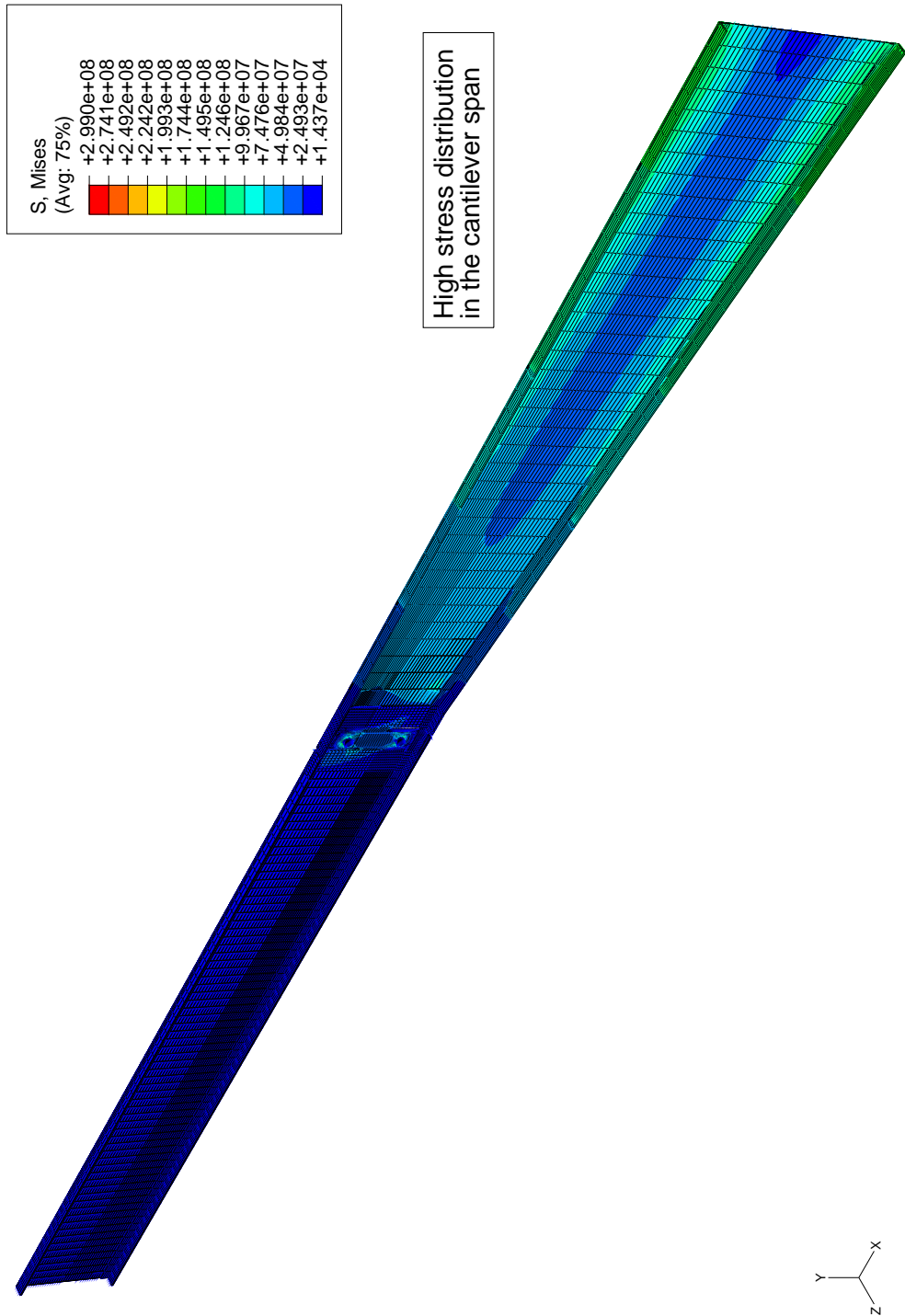


Figure 3.11. von Mises equivalent stress distribution

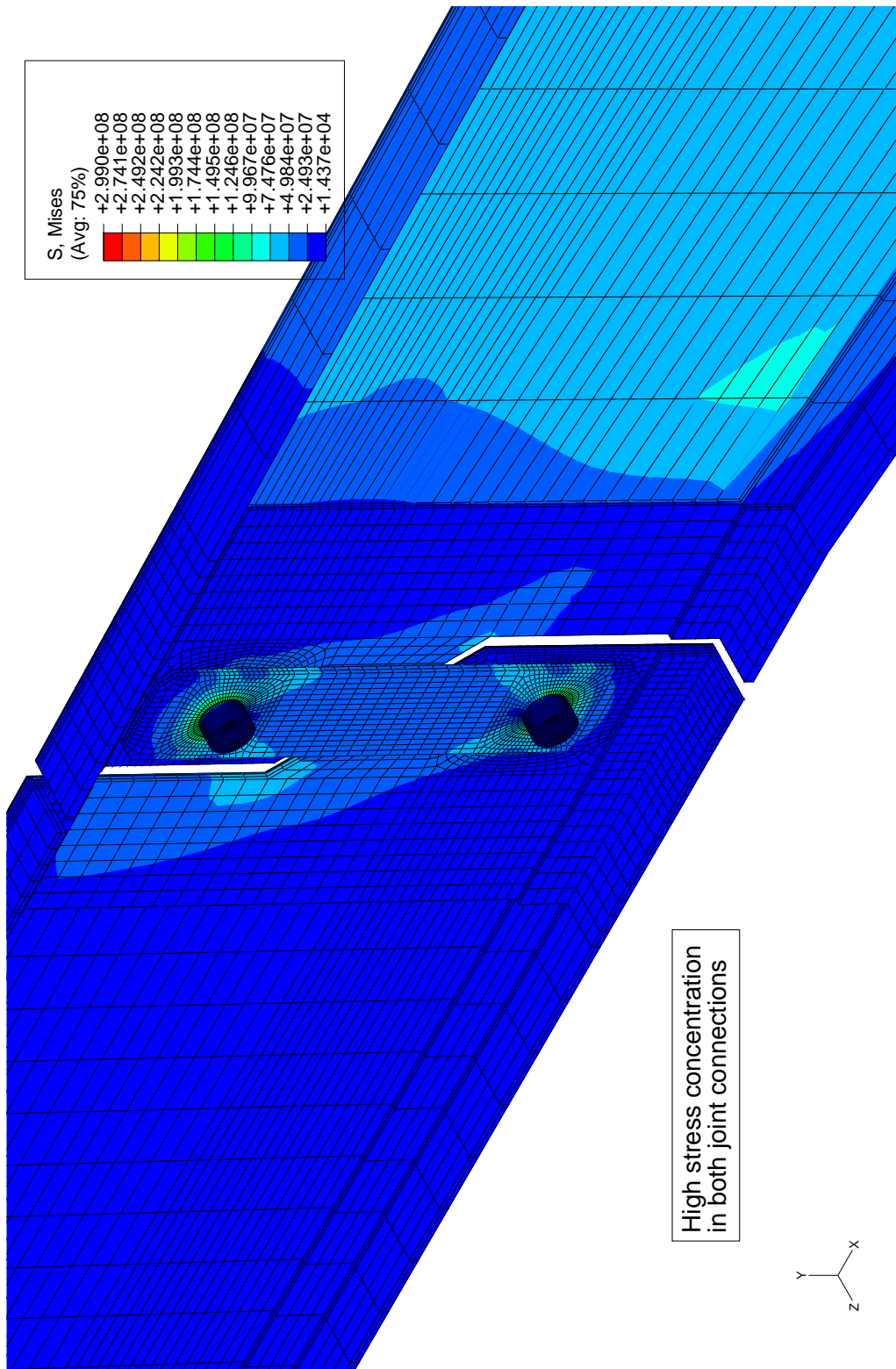


Figure 3.12. von Mises equivalent stress near joint connection

Table 3.5. von Mises equivalent stress σ_{eq} in bridge components

Components	σ_{eq}	σ_{eq}/σ_Y
Pin (bottom)	32.88 ksi	0.91
Pin (top)	32.79 ksi	0.91
Hanger	22.91 ksi	0.64

3.4. Concluding remarks

The results of the design calculations and the finite element analyses are seen to agree closely. The results also suggest that our 3D finite element model is a suitable model for the bridge problem. Furthermore, the accurate results we obtain confirm that the model is properly constrained and the choice of element as well as the selection of the contact algorithm is satisfactory. There is another issue that may affect the results as well, which is the contact interaction. It is important to note that if the contact procedure is not taken into account properly, the final results of the computation are greatly affected and can be completely wrong. This topic is not straightforward from the engineering point of view.

Additional sources of information include Belytschko *et al.* (2000) [12], Wriggers (2002) [13], and ABAQUS theory manual (2003) [2], amongst others.

It should be noted that the von Mises stress is an “equivalent” stress which is the result of the conversion from a multiaxial state of stress to an equivalent state of stress. Note that the resulting stress field is fully three-dimensional. Therefore, the *yielding* condition is obtained by converting 3D states of stress to equivalent 1D states which can be used with uniaxial experimental data (i.e., yield strength of the material used). As a result, this

equivalence is not perfect. Also, the von Mises equivalent stress (σ_{eq}) is always positive and does not identify the algebraic signs of stresses that contribute to it.

CHAPTER 4

Constitutive equations**4.1. Introduction**

The aim of this Chapter is to set up constitutive equations required to describe the physical stress-strain response of the bridge subjected to applied loads. The mechanical constitutive models often consider elastic and inelastic response. The inelastic response is most commonly created with plasticity models.

In the previous Chapter, the finite element modeling of the bridge was entirely based on an elastic response of the structure. For example, a mechanical component; i.e. hanger plate, made from a standard structural steel (ASTM A36), can be modeled as an isotropic and linear elastic material. This simple material model would probably suffice for routine design, so long as the component is not in any critical situation. However, if the component might be subjected to a severe overload, it is important to determine how it might deform under that load and if it has sufficient ductility to withstand the overload without catastrophic failure. In that case, the elastic-plastic material model will also be considered.

It is important to note that most engineering materials have a linear elastic behavior at the early stages of deformations. However, when certain criteria are reached; e.g., yield condition, several materials undergo permanent or plastic deformation.

4.2. Elasticity

As mentioned above, we first consider the simplest of these models, the linear elastic material model. Hooke's law for linearly elastic materials states that there is a linear relationship between the Cauchy stress and the small strain. The relationship between stress and strain can be written as,

$$(4.1) \quad \boldsymbol{\sigma} = \mathbf{C} : \boldsymbol{\varepsilon}^{el}$$

where $\boldsymbol{\sigma}$ denotes the *Cauchy stress* tensor, $\boldsymbol{\varepsilon}^{el}$ is the *elastic strain* tensor, and \mathbf{C} (often denoted by \mathbf{D} in some literature) is the fourth-order elasticity tensor.

For further details, one can refer to Timoshenko (1951) [14] and Malvern (1969) [15], amongst others, for references to the literature.

It is somehow interesting to note that the tensor notation, i.e. Eq. 4.1, is very elegant when it comes to theoretical derivations. The tensor notation is appealing because it allows the equations to be developed concisely without the complexities with the component form (also called index notation) in a particular basis system. However, for the purpose of applications, it is often more practical to work with the component form. Accordingly, Eq. 4.1 can be rewritten as,

$$(4.2) \quad \sigma_{ij} = C_{ijkl} \varepsilon_{kl}^{el}$$

Note that indices i, j, k , and l take on values $1, \dots, n$, where n is the spatial dimensions, and the summation convention applies to repeated indices i, j, k , and l .

For an *isotropic* material, \mathbf{C} takes a form ensuring that the material has the *same* properties in every direction. An isotropic fourth-order tensor \mathbf{C} has the form,

$$(4.3) \quad C_{ijkl} = \lambda \delta_{ij} \delta_{kl} + \mu (\delta_{ik} \delta_{jl} + \delta_{il} \delta_{jk})$$

where λ and μ are Lamé constants. After substituting Eq. 4.3 into Eq. 4.2, we obtain,

$$(4.4) \quad \sigma_{ij} = (\lambda \delta_{ij} \delta_{kl} + 2\mu \delta_{ik} \delta_{jl}) \varepsilon_{kl}^{el}$$

where $\delta_{ij}, \dots, \delta_{jk}$ denote Kronecker deltas. The Kronecker delta is defined as,

$$\delta_{ij} = \begin{cases} 1 & \text{if } i = j \\ 0 & \text{if } i \neq j \end{cases}$$

Therefore, the stress components becomes,

$$(4.5) \quad \sigma_{ij} = \lambda \varepsilon_{kk} \delta_{ij} + 2\mu \varepsilon_{ij}$$

In tensor notation, Eq. 4.5 can be written as,

$$(4.6) \quad \boldsymbol{\sigma} = \lambda \text{trace}(\boldsymbol{\varepsilon}) \mathbf{I} + 2\mu \boldsymbol{\varepsilon}$$

where $\text{trace}(\boldsymbol{\varepsilon}) = \varepsilon_{kk}$, the sum of the diagonal elements, and \mathbf{I} is the identity matrix.

In engineering practice, it is common to use engineering constants instead of the Lamé constants. The engineering constants are Young's modulus (E), Poisson's ratio (ν), and shear modulus (G). Thus, the relationships between these constants are,

$$(4.7) \quad \lambda = \frac{\nu E}{(1 + \nu)(1 - 2\nu)}, \quad \mu = G = \frac{E}{2(1 + \nu)}$$

After substituting these constants in Eq. 4.5, we obtain,

$$(4.8) \quad \sigma_{ij} = \frac{\nu E}{(1 + \nu)(1 - 2\nu)} \varepsilon_{kk} \delta_{ij} + \frac{E}{1 + \nu} \varepsilon_{ij}$$

In tensor notation, Eq. 4.8 becomes

$$(4.9) \quad \boldsymbol{\sigma} = \frac{\nu E}{(1 + \nu)(1 - 2\nu)} (\text{trace } (\boldsymbol{\varepsilon})) \mathbf{I} + \frac{E}{1 + \nu} \boldsymbol{\varepsilon}$$

Writing explicitly stress and elastic strain in column vectors, Hooke's law, in a three-dimensional state of stress, becomes

$$(4.10) \quad \begin{bmatrix} \sigma_{xx} \\ \sigma_{yy} \\ \sigma_{zz} \\ \sigma_{xy} \\ \sigma_{yz} \\ \sigma_{zx} \end{bmatrix} = \begin{bmatrix} \bar{E}(1 - \nu) & \bar{E}\nu & \bar{E}\nu & 0 & 0 & 0 \\ \bar{E}\nu & \bar{E}(1 - \nu) & \bar{E}\nu & 0 & 0 & 0 \\ \bar{E}\nu & \bar{E}\nu & \bar{E}(1 - \nu) & 0 & 0 & 0 \\ 0 & 0 & 0 & G & 0 & 0 \\ 0 & 0 & 0 & 0 & G & 0 \\ 0 & 0 & 0 & 0 & 0 & G \end{bmatrix} \begin{bmatrix} \varepsilon_{xx} \\ \varepsilon_{yy} \\ \varepsilon_{zz} \\ \gamma_{xy} \\ \gamma_{yz} \\ \gamma_{zx} \end{bmatrix}$$

where,

$$\bar{E} = \frac{E}{(1 + \nu)(1 - 2\nu)}$$

and,

$$\begin{cases} \gamma_{xy} = 2\varepsilon_{xy} \\ \gamma_{yz} = 2\varepsilon_{yz} \\ \gamma_{xz} = 2\varepsilon_{xz} \end{cases}$$

where γ is used to represent engineering shear strain because of its convenient geometric interpretation.

For further details, one can refer to Timoshenko (1951) [14], Fung (1965) [16], and Malvern (1969) [15], amongst others, for references to the literature.

4.3. Equilibrium equation

Let us consider an equilibrium problem in linear elasticity for an isotropic material. The problem consists of determining the displacements, strains, and stresses that satisfy the partial differential equations of equilibrium,

$$(4.11) \quad \frac{\partial \sigma_{ij}}{\partial x_j} + b_i = 0$$

Using component form, Eq. 4.11 can be rewritten as,

$$(4.12) \quad \sigma_{ij,j} + b_i = 0$$

where b_i defines the body force.

From the previous Section, the constitutive relation has been defined as,

$$(4.13) \quad \sigma_{ij} = \lambda \varepsilon_{kk} \delta_{ij} + 2\mu \varepsilon_{ij}$$

And the strain and displacement relation can be written using component form as follows,

$$(4.14) \quad \varepsilon_{ij} = \frac{1}{2}(u_{i,j} + u_{j,i})$$

Further details can be found in Timoshenko (1951) [14], Malvern (1969) [15], Belytschko *et al.* (2000) [12], Holzapfel (2000) [17], and ABAQUS Theory Manual (2003) [2].

4.4. Thermal strain

The temperature field dictates the thermal strain distribution in the solid, which in turn gives rise to thermal stresses when the solid is constrained. In other words, the thermal strain loads the solid. When a solid body is heated, the body expands. Likewise, when a solid body is cooled, it contracts. If thermal strains is included, then,

$$(4.15) \quad \boldsymbol{\varepsilon} = \boldsymbol{\varepsilon}^{el} + \boldsymbol{\varepsilon}^{th}$$

where $\boldsymbol{\varepsilon}^{th}$ is the thermal strain and $\boldsymbol{\varepsilon}^{el}$ the elastic strain.

For an isotropic material,

$$(4.16) \quad \boldsymbol{\varepsilon}^{th} = \alpha(T - T_0) \mathbf{I}$$

in which, α is the coefficient of thermal expansion, T and T_0 are current and initial temperatures respectively, and \mathbf{I} is the unit tensor. Using index notation, we obtain,

$$(4.17) \quad \varepsilon_{ij}^{th} = \alpha \Delta T \delta_{ij}$$

where ΔT denotes the temperature change.

Therefore, Hooke's law for thermoelastic problems can be written as,

$$(4.18) \quad \sigma_{ij} = C_{ijkl}(\varepsilon_{kl} - \alpha \Delta T \delta_{kl})$$

4.5. Elasto-plastic material behavior

4.5.1. Basic concepts

As the external loads (mechanical, thermal, environmental) acting on the structure are gradually increased, plastic deformation may take place. This means that, upon removal of the external loads, the elements of the structure do not return to their original shapes. Under such conditions, the stress-strain response of the material is nonlinear, even in the small strain regime. Most engineering materials have a linear elastic behavior at the early stages of deformations. However, when certain criteria are reached (e.g., yield condition), several materials undergo permanent or plastic deformation.

Under small-strain condition, we can decompose the total strain ($\boldsymbol{\varepsilon}$) into elastic ($\boldsymbol{\varepsilon}^{el}$) and plastic ($\boldsymbol{\varepsilon}^{pl}$) parts as follows,

$$(4.19) \quad \boldsymbol{\varepsilon} = \boldsymbol{\varepsilon}^{el} + \boldsymbol{\varepsilon}^{pl}$$

and in rate form,

$$(4.20) \quad \dot{\boldsymbol{\epsilon}} = \dot{\boldsymbol{\epsilon}}^{el} + \dot{\boldsymbol{\epsilon}}^{pl}$$

Then the isotropic elastic constitutive equation may be written as,

$$(4.21) \quad \dot{\boldsymbol{\sigma}} = \lambda \text{trace}(\dot{\boldsymbol{\epsilon}}^{el}) \mathbf{I} + 2\mu \dot{\boldsymbol{\epsilon}}^{el}$$

When the material is flowing inelastically, the inelastic part of the deformation is defined by the flow rule, which we can write as,

$$(4.22) \quad \dot{\boldsymbol{\epsilon}}^{pl} = \dot{\lambda} \Gamma_{ij}$$

where,

$$(4.23) \quad \Gamma_{ij} = \frac{3}{2\bar{\sigma}} S_{ij}$$

here, S_{ij} is the deviatoric stress. The deviatoric stress components, S_{ij} , are obtained by subtracting the mean stress from the Cauchy stress components as follows,

$$(4.24) \quad S_{ij} = \sigma_{ij} - \frac{1}{3} \sigma_{kk} \delta_{ij}$$

and $\bar{\sigma}$ is defined as,

$$(4.25) \quad \bar{\sigma} = \sqrt{\frac{3}{2} S_{ij} S_{ij}}$$

Similarly, the total accumulated plastic strain, $\bar{\varepsilon}^{pl}$, can be expressed as,

$$(4.26) \quad \bar{\varepsilon}^{pl} = \int_0^{\varepsilon_{ij}^{pl}} d\bar{\varepsilon}^{pl} = \int_0^{\varepsilon_{ij}^{pl}} \dot{\bar{\varepsilon}}^{pl} dt$$

where,

$$(4.27) \quad \dot{\bar{\varepsilon}}^{pl} = \sqrt{\frac{2}{3} \dot{\varepsilon}_{ij}^{pl} \dot{\varepsilon}_{ij}^{pl}}$$

Other sources of information include Hill (1950) [18], Owen and Hinton (1980) [19], Crisfield (1991) [20], Khan *et al.* (1995) [21], and ABAQUS Theory Manual (2003) [2].

4.5.2. Yield condition

The yield condition is in general referred to as a yield function or yield surface. A important yield condition for ductile metals is the von Mises yield condition developed by Richard von Mises (1913). The von Mises yield condition ignores the third invariant of the deviatoric stress tensor and assumes that the yield function only depends on J_2 . This condition can be written as,

$$(4.28) \quad J_2 - k^2 = 0$$

where k is a scalar quantity.

When the yield condition is assumed to be isotropic, a general state of stress at a point can be written in terms of the principal stress as,

$$(4.29) \quad \begin{bmatrix} \sigma_1 & 0 & 0 \\ 0 & \sigma_2 & 0 \\ 0 & 0 & \sigma_3 \end{bmatrix}$$

As mentioned previously, the deviatoric part of the stress (Eq. 4.29) is obtained as follows,

$$(4.30) \quad \mathbf{S} = p\mathbf{I} + \boldsymbol{\sigma}$$

where \mathbf{S} is the deviatoric part of the Cauchy stress tensor $\boldsymbol{\sigma}$;

$$(4.31) \quad p = -\frac{1}{3}\boldsymbol{\sigma} : \mathbf{I}$$

where p is the hydrostatic pressure and \mathbf{I} is the second-order identity tensor.

Thus, Eq. 4.30 becomes

$$(4.32) \quad \begin{aligned} \mathbf{S} &= p\mathbf{I} + \boldsymbol{\sigma} \\ &= \begin{bmatrix} 2\sigma_1 - \sigma_2 - \sigma_3 & 0 & 0 \\ 0 & 2\sigma_2 - \sigma_1 - \sigma_3 & 0 \\ 0 & 0 & 2\sigma_3 - \sigma_1 - \sigma_2 \end{bmatrix} \end{aligned}$$

The quantity J_2 turns out to be

$$(4.33) \quad J_2 = \frac{1}{3}(\sigma_1^2 + \sigma_2^2 + \sigma_3^2 - \sigma_1\sigma_2 - \sigma_1\sigma_3 - \sigma_2\sigma_3)$$

The von Mises yield condition can be written in terms of the 3 principal stresses as,

$$(4.34) \quad (\sigma_1^2 + \sigma_2^2 + \sigma_3^2 - \sigma_1\sigma_2 - \sigma_1\sigma_3 - \sigma_2\sigma_3) + 3k^2$$

The von Mises equivalent stress, σ_{eq} , is defined as

$$(4.35) \quad \sigma_{eq} = \sqrt{3J_2}$$

and the von Mises yield condition is written as,

$$(4.36) \quad \sigma_{eq} - \sqrt{3}k = 0$$

The yield condition in this form is convenient to use in practice. One can assess whether a component can be expected to yield under external loadings by performing a linear finite element analysis and then observing a contour plot of the von Mises equivalent stress (σ_{eq}). If $\sigma_{eq} \geq \sigma_Y$ at a particular location, then the component can be expected to yield at that location. Here, σ_Y defines the yield stress of the materials. Details of the calculations which refer to the von Mises yield condition can be found in Chapter 3.

4.6. Contact modeling

The objective of this section is to describe the contact interaction between different part components which form the joint assemblies; i.e. web girder and pin, pin and hanger, etc. Also, the bridge components in contact to each other are assumed to be deformable bodies.

The contact problem which involves 3D multi-body interaction is probably the most challenging issue in numerical modeling. If contact procedures are not taken into account

properly, the final results of the computation are greatly affected and can be completely wrong. The topic is not straightforward from the engineering point of view.

Furthermore, in the current project, we intend to use the friction capability to simulate the “frozen” and “unfrozen” conditions, also called “locking” and “unlocking” conditions, between the pin and the hanger.

4.6.1. Basic concepts

In finite element analysis, contact conditions are a special class of discontinuous constraint, allowing forces to be transmitted from one part of the model to another.

The constraint is discontinuous because it is applied only when the surfaces are in contact. When the surfaces separate, no constraint is applied. Therefore, the analysis has to be able to detect when two surfaces are in contact and apply the contact constraint accordingly. Similarly, the analysis must be able to detect when two surfaces separate and remove the contact constraints.

Other sources of information regarding this topic can be found in Belytschko *et al.* (2000) [12], Wriggers (2002) [13], and ABAQUS Theory Manual (2003) [2].

4.6.2. Contact capabilities in ABAQUS

ABAQUS provides two algorithms for modeling the interaction between deformable bodies.

The first algorithm is called a *small-sliding* formulation in which the contacting surfaces can undergo only small sliding relative to each other, but arbitrary rotation of the

surfaces is permitted. The second algorithm is called a *finite-sliding* formulation where separation and sliding of finite amplitude may arise.

Among other considerations, small-sliding contact is computationally less expensive than finite-sliding contact.

Contact simulations in ABAQUS are surface based contact. Surfaces that will be involved in contact must be created on the various components in the model; i.e. pin, hanger, web-girder. Then, the pairs of surfaces that may contact each other known as contact pairs, must be identified. Finally, the constitutive model governing the interaction between the various surfaces must be defined.

With this approach, one surface definition provides “master” surface and the other surface definition provides “slave” surface. In addition, a kinematic constraint that the slave surface nodes do not penetrate the master surface is then enforced ([2]).

4.6.3. Friction

The Coulomb friction model is used with all contact analyses. It states that the critical stress, τ_{cr} , is proportional to the contact pressure, p , in the form

$$(4.37) \quad \tau_{cr} = \mu p$$

An *extended* version of the classical isotropic Coulomb friction model is provided in ABAQUS. The extensions mainly include an additional limit on the allowable shear stress. The Coulomb friction model assumes that no relative motion occurs if the *equivalent*

frictional stress, τ_{eq} , is less than the critical stress, τ_{crit} , ([2]).

$$(4.38) \quad \tau_{eq} < \tau_{crit}$$

in which, τ_{eq} and τ_{crit} are defined as follows,

$$\tau_{eq} = \sqrt{\tau_1^2 + \tau_2^2}$$

and,

$$\tau_{crit} = \mu p$$

where μ is the friction coefficient that can be defined as a function of contact pressure (p), slip rate ($\dot{\gamma}_{eq}$), the surface temperature, and the field variables at the contact point. τ_1 and τ_2 denote shear stresses in the tangential directions \mathbf{t}_1 and \mathbf{t}_2 .

In practice, the problem usually reduces to knowing a friction coefficient under operating conditions.

A special case of friction is called “rough” friction. The rough friction parameter was used in the definition of the contact surfaces. This implies that when the pin, the hanger, and web girder come into contact, no relative slipping is allowed. Here, rough friction is used to simulate the frozen condition, mentioned above.

CHAPTER 5

Thermal effects on bridge movements

5.1. Introduction

Our primary objective here is to develop a method to evaluate the bridge movements induced due to temperature changes. The effects of thermal “forces” (due to temperature changes) on a bridge structure are significant and should not be underestimated. These movements have considerable impact on its design and performance.

All of the bridge structural components that we have considered so far were assumed to remain at the *same* temperature while they were being loaded. Such assumption is not realistic. In fact, bridges expand and contract due to temperature changes (daily and seasonal changes). In general, thermal forces are caused by fluctuations in temperature (i.e., from cold to hot or from hot to cold). The structural response under thermal loading can be very complex, even though the overall strain is predominantly pure thermal expansion or contraction.

As mentioned earlier, the primary function of a pin-and-hanger connection is to allow for longitudinal thermal expansion and contraction in the bridge superstructure.

5.2. AASHTO recommendations and alternative approaches

According to Roeder (2003) [22], the temperatures used for determination of thermal design movements in the present AASHTO specifications (AASHTO 1996, 1998) have

been used since 1920s. The design temperatures recommended in the AASHTO specifications sometimes predict movements that are larger or smaller than needed.

For example, the Illinois Department of Transportation (IDOT) (1992) [4] attempted to measure the displacements of the bridge components due to temperature changes by using a series of experimental tests. Several methods for detecting pin-hanger movements were developed which range from simple to sophisticated. These include: (a) paper gages, (b) paint stripes, (c) pointers, (d) strain gages, and (e) electronic rotation sensors. They pointed out that the results using these techniques were not promising. The drawbacks include difficulty of detecting small movements and complications in installation and operating.

5.3. Temperature ranges

In general, thermal forces are caused by fluctuations in temperature (i.e., from cold to hot or from hot to cold). AASHTO (1996) [11] provides temperature variations depending on whether the structure is in a moderate or cold climate region. For metal structures, the values are given in the form of extreme hot and cold temperatures (see Table 5.1).

Table 5.1. AASHTO temperature ranges

	From	To
Moderate climate	0°F	120°F
Cold climate	-30°F	120°F

5.4. Response to temperature variations

Variations in temperature distribution in bridge members can be described in terms of a *uniform* temperature and a *gradient* temperature.

The uniform (average) temperature only causes changes in dimension of the member, while the temperature gradient causes bending deformations. On the other hand, if longitudinal expansion is prevented, the girder may experience large axial forces, which could lead to damage of the joint connection, ([22]).

5.5. New proposed method

Here, we propose a new and simple method. Our approach consists of using mathematical expression for determining bridge movements due to thermal forces. This technique can be used for design purposes or for bridge maintenance. For design calculation, it can help to check the exact dimension and clearances between critical components based on the ultimate temperature changes. In other words, the main design consequence of temperature fluctuations is that these deformations must be accommodated. For example, the designer needs to provide a pin-and-hanger connection with adequate displacement and rotation capacities. The details of the method will be described in the following sections.

5.5.1. Thermal strain

As mentioned earlier, changes in temperature produce expansion or contraction of structural materials, resulting in *thermal strains* and *thermal stresses*. In the present study, we assume that the temperature profile is linear and uniformly distributed over the height of the bridge.

For most structural materials such as bridge structure, *thermal strain*, ε^{th} , is proportional to the temperature change ΔT ; that is,

$$(5.1) \quad \varepsilon^{th} = \alpha(\Delta T)$$

in which α is a property of material called the coefficient of thermal expansion (CTE). ΔT is the differential between the extreme design temperatures and the installation temperature.

For instance, if the bridge span length is L , then the dimension will increase by the amount of δL ,

$$(5.2) \quad \delta L = \varepsilon^{th}L = \alpha(\Delta T)L$$

where δL is an elongation due to thermal expansion/contraction.

5.5.2. Rotational angle

On the other hand, the expression of the rotational angle, θ , of the pin-hanger connection relative to the reference position (Figure 5.1), is given by

$$(5.3) \quad \tan \theta = \frac{\delta L}{l_0/2}$$

Upon rearranging, the above equation becomes:

$$(5.4) \quad \theta = \tan^{-1} \left[\frac{2\alpha\Delta TL}{l_0} \right]$$

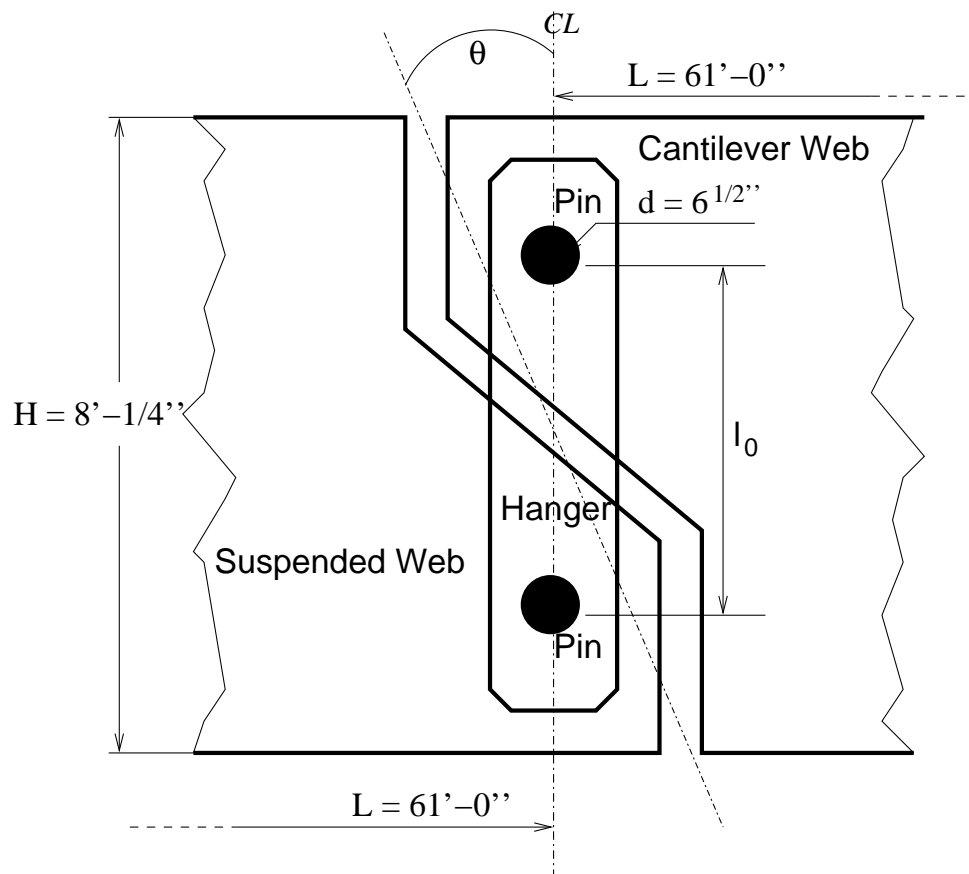


Figure 5.1. Typical pin and hanger connection

where l_0 is a segment which measure the distance between top and bottom positions of the connections. Since the angle of rotation, θ , is a small quantity, then the above equation (5.4) can be written as,

$$(5.5) \quad \theta \approx \frac{2\alpha\Delta TL}{l_0}$$

We assume that the entire bridge is made of the same construction material (ASTM A36). A Young's modulus of $E = 29 \times 10^6$ psi (200 GPa) and a Poisson's ratio of $\nu = 0.3$

define the elastic response of the typical structural material. Its coefficient of thermal expansion (CTE) is $6.5 \times 10^{-6}/^{\circ}\text{F}$ ($11.7 \times 10^{-6}/^{\circ}\text{C}$) (at room temperature).

5.5.3. Numerical results

A series of finite element computations were carried out. The results of the FEA are compared with the values obtained from the above analytical expressions (see Table 5.2). The corresponding elongations are given in Table 5.3. They are seen to be in excellent agreement.

Table 5.2. Comparison between exact $(\theta)_{EXACT}$ and finite element results $(\theta)_{FEA}$

ΔT [$^{\circ}\text{F}$]	$(\theta)_{EXACT}$ [degrees]	$(\theta)_{FEA}$ [degrees]	Error [%]
120	0.920	0.937	1.8
68	0.378	0.382	1.0
-4	-0.378	-0.383	1.3
-30	-0.651	-0.662	0.6

Table 5.3. Elongation vs. temperature

ΔT [° F]	$(\delta L)_{EXACT}$ [in.]	$(\delta L)_{FEA}$ [in.]
120	0.417	0.425
68	0.171	0.173
-4	-0.171	-0.174
-30	-0.295	-0.300

5.6. Concluding remarks

The agreement between the two results (analytical and FEA solutions) is excellent. It is clear that our proposed method is fast and reliable for helping in design purpose. It may be useful to the bridge community to include this method in the AASHTO specifications.

CHAPTER 6

Operating conditions**6.1. Introduction**

In this Chapter we will discuss the “operating conditions” of the bridge. This means that we will consider two engineering aspects similar to the real-world applications of the bridge. These include:

- lock-up condition due to pack-rust formation in the joint; and
- elastic-plastic response of the bridge structure.

6.2. Locked-up condition

As mentioned, a known problem associated with hanger plate and pin assemblies is corrosion. The joint connection may partially or fully *freeze* (locked-up), thus inhibiting the free rotation. This can lead to a large torque on the pin with plastic yielding. A typical corrosion buildup (or pack-rust) example is shown in Figure 6.1.

According to the results (locked-up condition), as illustrated in Table 6.1, we observe that the higher stress distribution takes place in the bottom pin with plastic yielding, and is 1.6 times higher than in the unlocked condition. This may render the bridge unsafe for daily use for traffic.

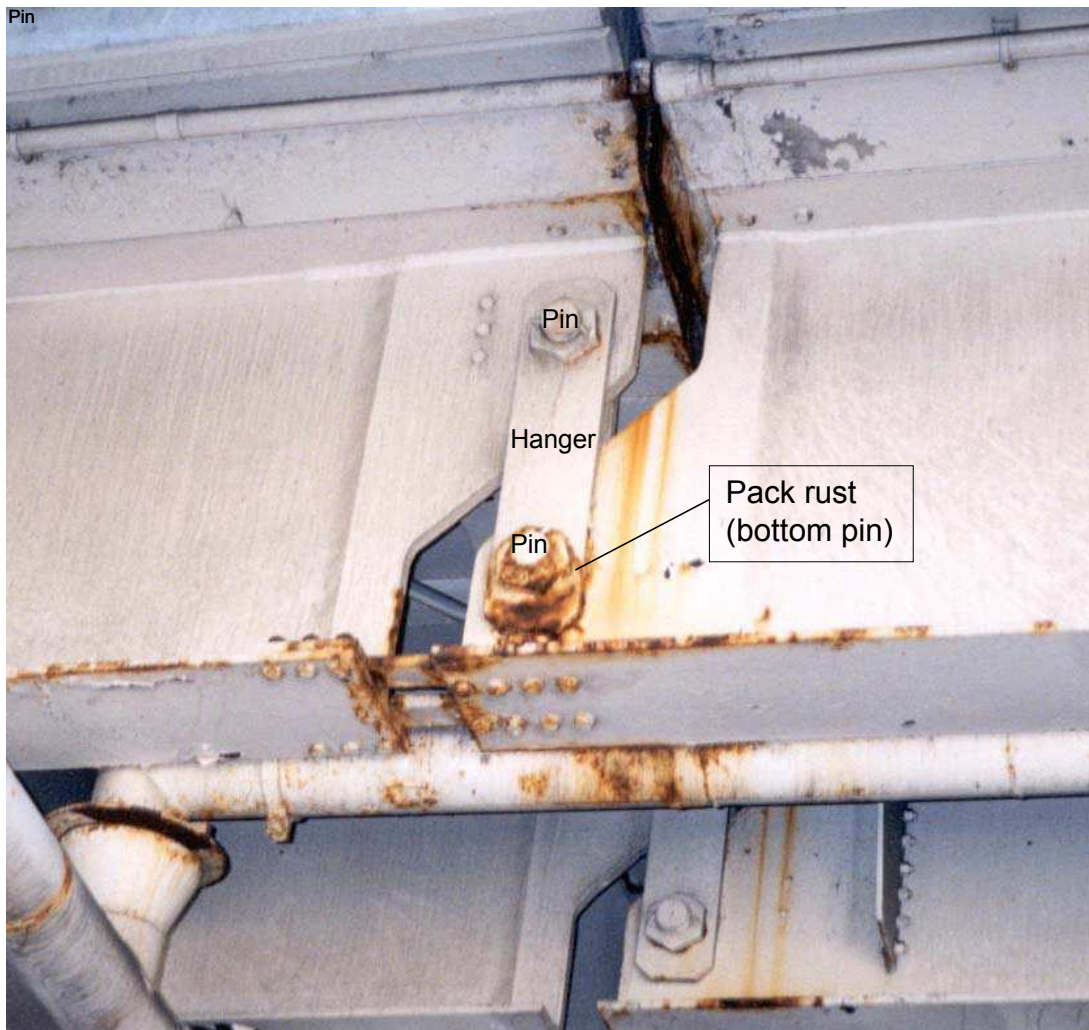


Figure 6.1. Typical pack rust formation

Table 6.1. von Mises equivalent stress σ_{eq} (locked condition)

Components	σ_{eq}	σ_{eq}/σ_Y
Pin (bottom)	54.01 ksi	1.50
Pin (top)	35.08 ksi	0.97
Hanger	38.43 ksi	1.07

6.3. Elastic-plastic behavior

All the analyses discussed so far have been considered as *linear* elastic. This means that there is a linear relationship between the applied loads and the response of the structure. In general, the bridge structure is *nonlinear* especially when the pin is in the locked condition. An elastic-plastic analysis is required to model the bridge behavior when the pin is locked.

6.3.1. Material nonlinearity

In most cases, the material behaviors fall into the following categories:

- elastic mechanical properties;
- inelastic mechanical properties;
- thermal properties; and
- general properties (density, thermal expansion, material damping).

At higher stress, metals begin to have nonlinear inelastic behavior which is referred to as plasticity. The plastic behavior of a material is described by its yield point and its post-yield hardening. The shift from elastic to plastic occurs at a certain point, known as a yield point on a materials stress-strain curve.

Further details can be found in Hertzberg (1996) [23], Boresi *et al.* (2003) [24], and ABAQUS User Manuals (2003) [2].

6.3.2. Defining plasticity in ABAQUS

When defining plasticity in ABAQUS, we must use *true stress* and *true strain*. However, material test data are commonly supplied using *engineering stress* and *engineering strain*,

also called *nominal* stress and *nominal* strain. In such situations, we must use the expressions presented below to convert from engineering stress/strain to true stress/strain values.

The deformation of the metal prior to reaching the yield point creates only *elastic strains*, which are fully recovered if the applied load is removed. However, once the stress in the metal exceeds the *yield stress*, permanent (*plastic*) deformation begins to occur. The strains associated with this permanent deformation are called *plastic strains*. Both elastic and plastic strains accumulate as the metal deforms in the post-yield region. The stiffness of the metal decreases once the material yields, ([2]).

Strains in tension and compression are the same as long as $\Delta l \rightarrow dl \rightarrow 0$,

$$d\varepsilon = \frac{dl}{l}$$

thus,

$$\begin{aligned}\varepsilon &= \int_{l_0}^l \frac{dl}{l} \\ &= \ln\left(\frac{l}{l_0}\right)\end{aligned}$$

where l is the current length, l_0 is the original length, and ε is the true strain or *logarithmic strain*.

The true stress is defined as,

$$\sigma = \frac{F}{A}$$

where F is the force in the material and A is the current area.

The relationship between true strain and engineering strain is established by expressing the engineering strain as,

$$\begin{aligned}\varepsilon_{eng} &= \frac{l - l_0}{l_0} \\ &= \frac{l}{l_0} - 1\end{aligned}$$

Thus, the relationship between the true strain and engineering strain is

$$(6.1) \quad \varepsilon = \ln(1 + \varepsilon_{eng})$$

The relationship between the true stress and engineering stress is formed by considering the incompressible nature of the plastic deformation,

$$l_0 A_0 = l A$$

thus, the current area, A , is related to the original area, A_0 , by

$$A = A_0 \frac{l_0}{l}$$

Substituting A into the true stress gives

$$\begin{aligned}\sigma &= \frac{F}{A} \\ &= \frac{F}{A_0} \frac{l}{l_0} \\ &= \sigma_{eng} \left(\frac{l}{l_0} \right) \\ &= \sigma_{eng} (1 + \varepsilon_{eng})\end{aligned}$$

Therefore, the relationship between true stress and engineering stress is

$$(6.2) \quad \sigma = \sigma_{eng}(1 + \varepsilon_{eng})$$

The plasticity model data defines the true yield stress of the material as a function of true plastic strain.

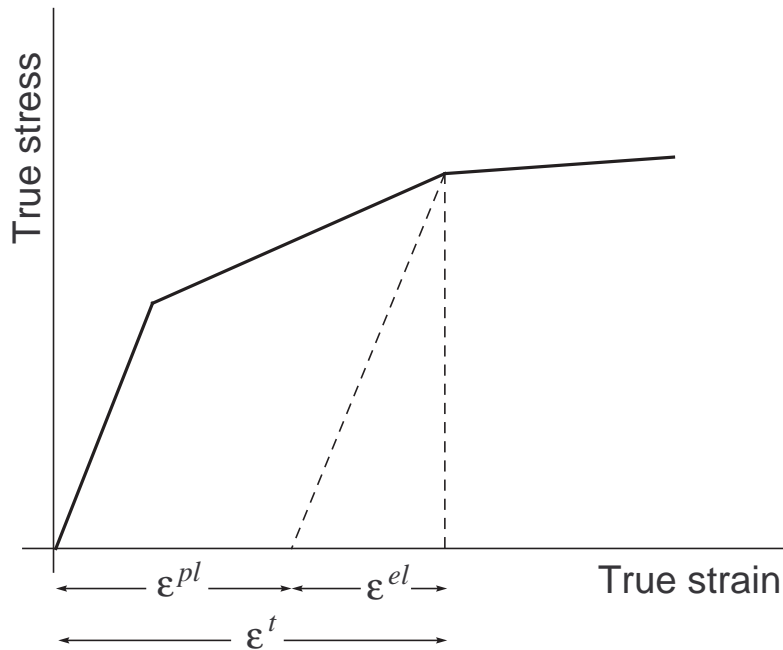


Figure 6.2. Decomposition of the total strain into elastic and plastic strains

The strains provided in material test data used to define the plastic behavior are not likely to be the plastic strains (ε^{pl}) in the material. Instead, they will probably be the total strains (ε^t) in the material. Thus, we must decompose the total strain values (ε^t)

into the elastic (ε^{el}) and plastic (ε^{pl}) components. The plastic strain (ε^{pl}) is then obtained by subtracting the elastic strain (ε^{el}) from the total strain (ε^t).

This relationship is written as,

$$\begin{aligned}\varepsilon^{pl} &= \varepsilon^t - \varepsilon^{el} \\ &= \varepsilon^t - \frac{\sigma}{E}\end{aligned}$$

where, σ is true stress and E is Young's modulus.

6.3.3. Defining the plasticity curve

Figure 6.3 illustrates the elastic-plastic material behavior of the structural steel (ASTM A36).

Typically, the material behavior is obtained based on simple uniaxial tests. This uniaxial curve (stress vs. strain) is then provided to the FEA program. However, in FEA program, the state of stress and strain is multiaxial. In order to use the uniaxial experimental stress-strain curve, the FEA program “converts” the multiaxial strain tensor (6 components) in *equivalent* strain (1 component). This strain is called equivalent because it converts a multiaxial state of strain to an equivalent state of strain.

Similarly, the von Mises stress is an equivalent stress which is the result of the conversion from a multiaxial state of stress to an equivalent state of stress. Therefore, the *yielding* condition is obtained by converting 3D (or 2D) states of stress and strain to equivalent 1D states which can be used with uniaxial experimental data. As a result, this equivalence is not perfect and depends on the plasticity theory used.

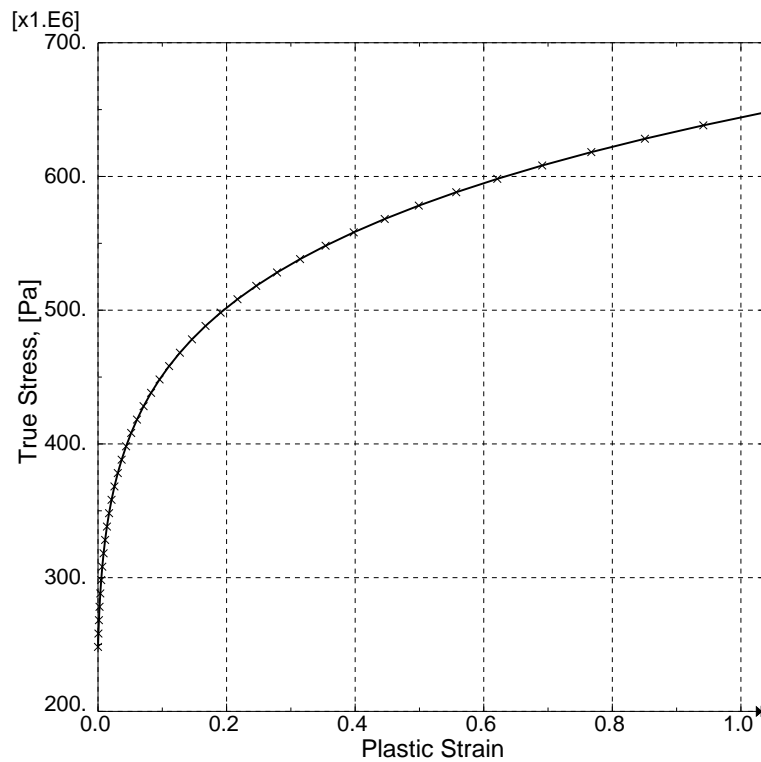


Figure 6.3. Elastic-plastic material behavior (ASTM A36) used for the computations

6.4. Lock-up condition and elastic-plastic response

Based on the computational results, Table 6.2 recapitulates the von Mises equivalent stresses (σ_{eq}) for the lock up condition. It was found that in the elastic-plastic material behavior, pin and hanger components are roughly at the same level of stress distribution, which is close to the yield stress ($\sigma_Y = 36$ ksi). Again, this may render the bridge unsafe for daily use for traffic.

The Mises stress contour and final deformed shapes of the bridge component; e.g. pin, is depicted in Figure 6.4. Note the high stress distribution on the pin surface which represents the torsion due to freezing condition in the joint.

Table 6.2. von Mises equivalent stress σ_{eq} (locked)

Components	σ_{eq}	σ_{eq}/σ_Y
Pin (bottom)	37.75 ksi	1.05
Pin (top)	35.10 ksi	0.97
Hanger	36.08 ksi	1.00

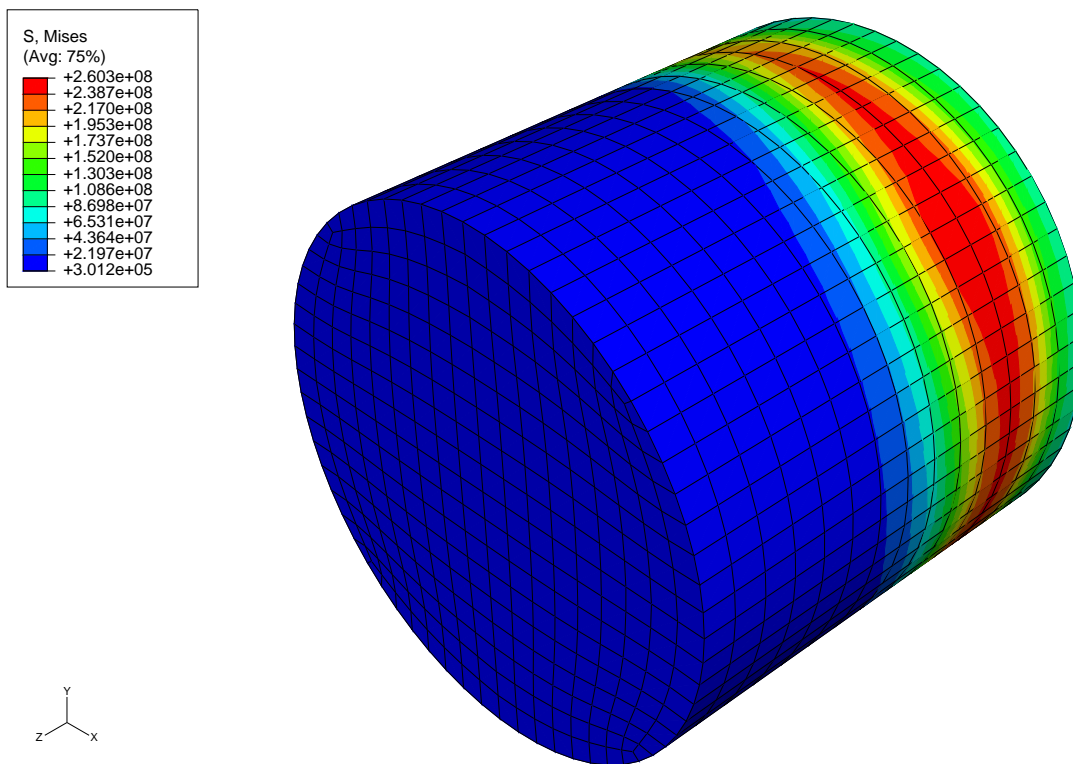


Figure 6.4. Mises stress on the bottom pin: lock up and elastic-plastic material

The tension prediction by FEA (in the middle of the hanger section) for the case of full locked-up is shown in Figure 6.6 (compare with Figure 3.7 in Chapter 3). Figure 6.5 also illustrates the bending in the cross-section of the hanger. Also, note the different profiles of the stress concentration between 2 case scenarios: lock-up and unlocked (see Chapter 3) conditions.

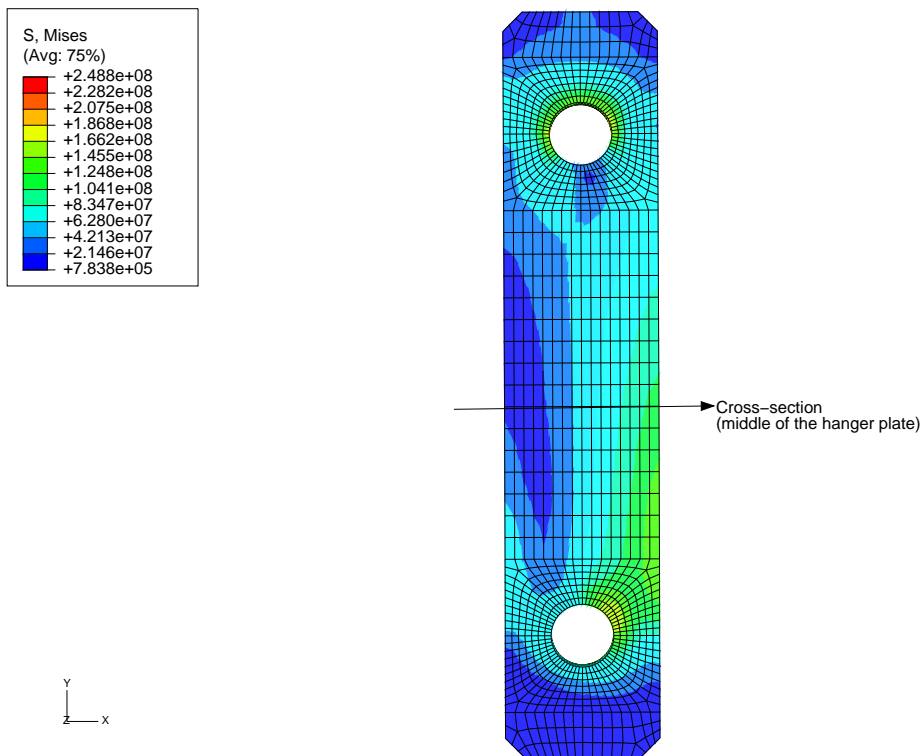


Figure 6.5. Tension profile in the hanger plate: lock up and elastic-plastic material

6.5. Concluding remarks

We have shown the results which correspond to the so-called “operating conditions” of the bridge. They are assumed to simulate the optimal operating conditions of the highway bridge in extreme environmental situations:

- Freezing in the joint mechanism;
- Elastic-plastic material behavior.

The final results are slightly greater than the yield stress of the materials used (ASTM A36). Plasticity is predicted to occur under these conditions.

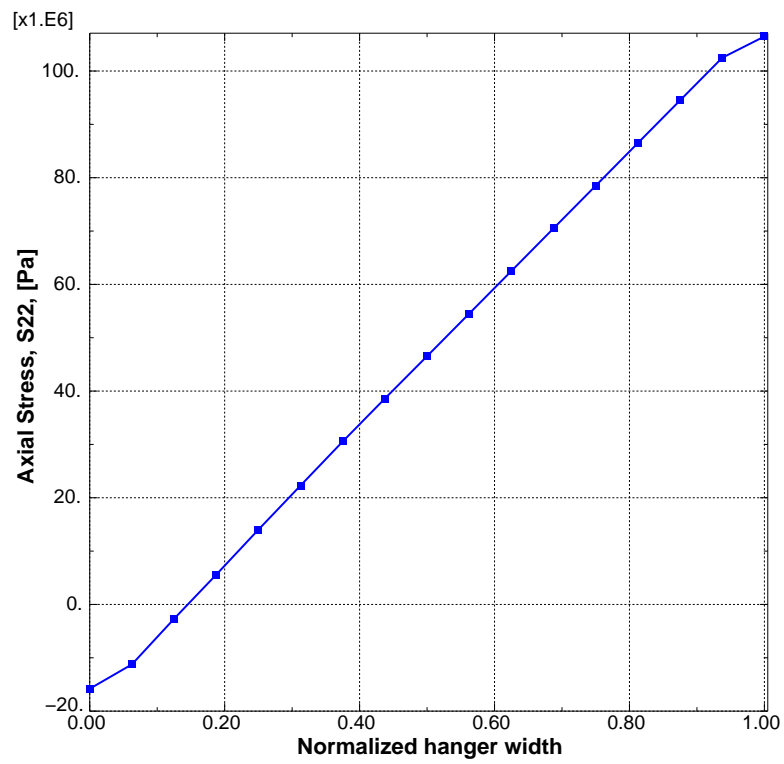


Figure 6.6. Axial stress in hanger for lock up and elastic-plastic material behavior

CHAPTER 7

Stress intensity factors for transverse crack in a pin**7.1. Introduction**

The computation of the SIFs along the three-dimensional crack front remains a challenging problem. This is primarily due to the fact that accurate calculation of stress intensity factors (SIFs) in engineering applications has been a non-trivial task.

Under repeated loadings and corrosion, cracks may develop at the surface and grow across the section of the cylinder (pin). Small cracks developing on the cylindrical surface have been an issue of concern over the past decades. The presence of such flaws or cracks raises the stress and strain significantly in the vicinity of these imperfections.

Stress intensity factor solutions required to assess the structural integrity of such configurations are lacking (Gosz and Moran, 1998 [25]). In the past, various methods, such as the finite element method (with or without singularity elements) and the boundary integral method, have been employed to obtain stress-intensity factor distributions for surface cracks and corner cracks in plates (Raju and Newman, 1979 [26] and Newman and Raju, 1983 [27]).

To address this need, another well established and useful method, known as the “domain integral method”, is used to obtain the mixed-mode of the stress intensity factors (SIFs), namely mode I, mode II, and mode III. In the domain integral method, a crack-tip contour integral is expressed as a volume integral over a finite domain surrounding the

crack-tip. The process of recasting the contour integral into a volume integral is advantageous for numerical purposes. For a general discussion on crack-tip contour integrals and their associated domain integral representation, see Moran and Shih, 1987 ([**28**] and [**29**]). Contour integral evaluation is available in ABAQUS [**2**] for any loading (including thermal loading) and for elastic and elastic-plastic material behaviors.

In the present study, we present the results of the evaluation of the mixed-mode stress intensity factors (SIFs), namely K_I , K_{II} , and K_{III} , applied to the joint connection of the bridge. The initial crack profile is illustrated in Figures 7.1 and 7.11. The crack dimensions are: $a = 0.236$ in. (6 mm), $c = 0.55$ in. (14 mm), and $D = 6.5$ in. (165.1 mm).

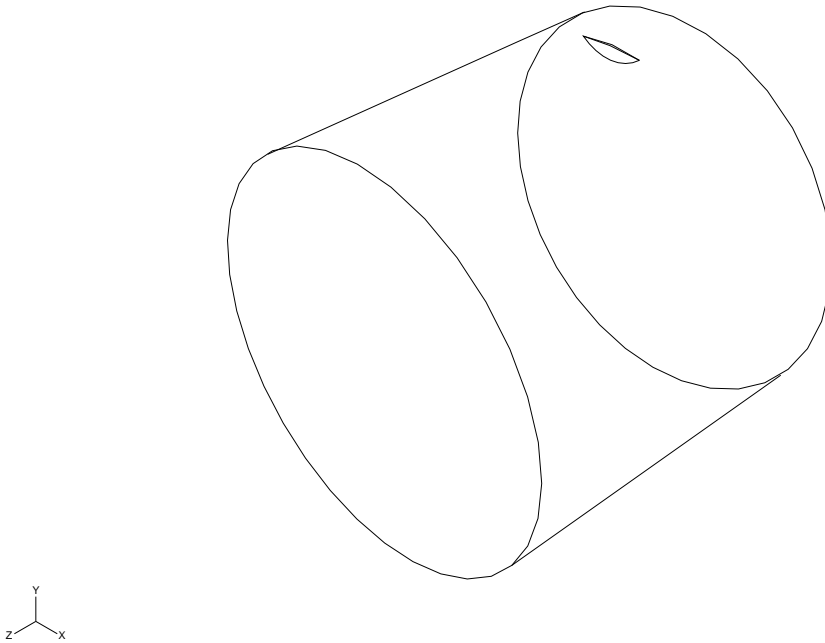


Figure 7.1. Initial crack profile embedded on the pin surface

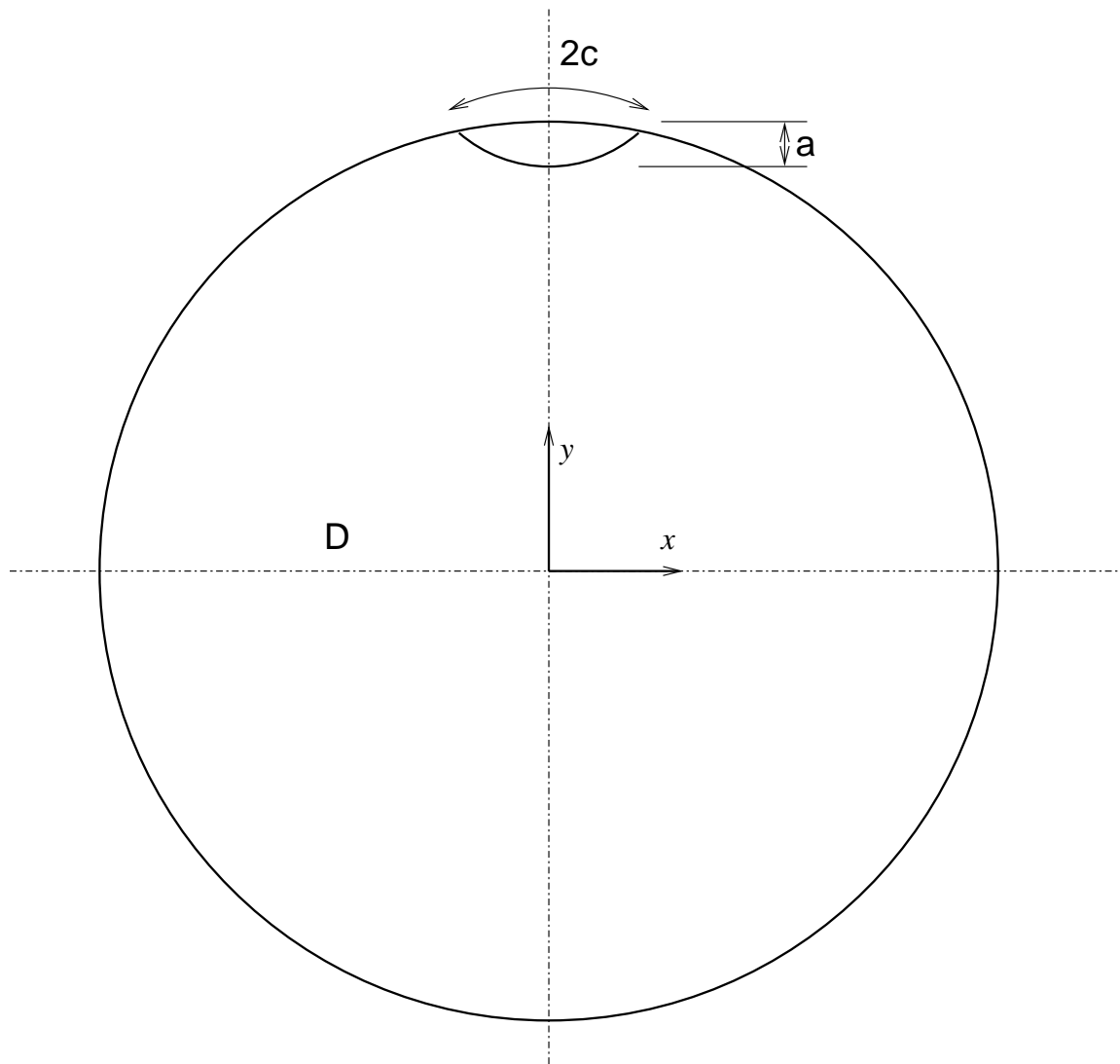


Figure 7.2. Initial crack dimensions: $a=6$ mm, $c=13.66$ mm, $D=165.1$ mm

7.2. Determination of stress intensity factors

7.2.1. overview

As indicated by Schijve (2001) [30], many results of calculations on stress intensity factors (K) for various geometries and loading cases have been published. Therefore, the first

approach to obtain K -values should be to consult the literature. Compilations of K -solutions can be found in some handbooks. Frequently cited books are:

- “The Stress Analysis of Cracks Handbook”, 1973, by H. Tada, P. C. Paris, and G. R. Irwin ([31]).
- “Stress Intensity Factors”, 1976, by D. P. Rooke and Carthwright ([32]).
- “Stress Intensity Factors Handbook”, 1987, three volumes, edited by Y. Murakami ([33]).

The above comments and suggestions are mainly concerned with plane 2D problems. In spite of the extensive literature on K -values, it should be pointed out that in many practical cases; i.e. the present investigation, K -solutions for cracks are not available. Sometimes, the values can be approximated by available solutions for less complicated geometries. Otherwise, the finite element (FE) calculations are necessary. That was the way we proceeded for the present investigation.

The calculation techniques are significantly more complex for 3D cases with curved crack front (as shown in Figure 7.1). There is no symmetry in this crack model. The model validation is not always easy.

Furthermore, the three-dimensional nature of this type of crack results in the stress intensity factors that are not only varying along the crack front, but highly sensitive to the crack shape and the direct location of the applied load (contact pressure). As a result, the crack shape may change as the crack grows.

Solutions derived using finite element analyses are available. Among others, Raju and Newman (1986) [34], Shiratori et al. (1986) [35], Shih and Chen (2002) [36], and Cai

and Shin (2004) [37]. However, their solutions are generally limited to either only one parameter (crack depth ratio) and one or two loading conditions (tension/bending).

In the present study, the combined loading, which results from the 3D multi-body contact, includes compression, bending, and torsion. In the determination of fracture parameter, such as the stress intensity factor (K), analytical solutions are needed to check the accuracy of the numerical results. Unfortunately, there is a dearth of known analytical solutions to 3D crack problems similar to our model. Consequently, we will first conduct a series of tests to validate the 3D crack model. These include:

- Check the validity of a simplified 3D crack model with available results in literature (Raju and Newman, 1979 [26])
- Compute various mixed-mode problems under combined loadings using bridge model and operating conditions.

It is interesting to note that the cylindrical-shaped components, such as pins, shafts, and bolts, are commonly used in engineering structures. Here, we will show one approach to solving this typical problem. First, we will introduce the basic concepts which relate to the stress analysis of cracks and the J -integral.

7.2.2. Stress analysis of cracks

The stress intensity factors characterize the influence of load on the magnitude of the crack-tip stress and strain fields.

To establish methods of stress analysis for cracks in elastic solids, it is convenient to define three types of relative movements of two crack surfaces (Paris, 1965 [38]). These

displacement modes (Figure 7.3) represent the local deformation ahead of a crack (Barsom and Rolfe, 1999 [39]):

- *Mode I* is the opening or tensile mode. The two fracture surfaces are displaced perpendicular to each other in opposite direction.
- In *Mode II*, the sliding or in-plane shearing mode, the crack faces slide relative to each others.
- In the tearing or antiplane mode, namely *Mode III*, the crack faces also slide relative to each other but antisymmetrically.

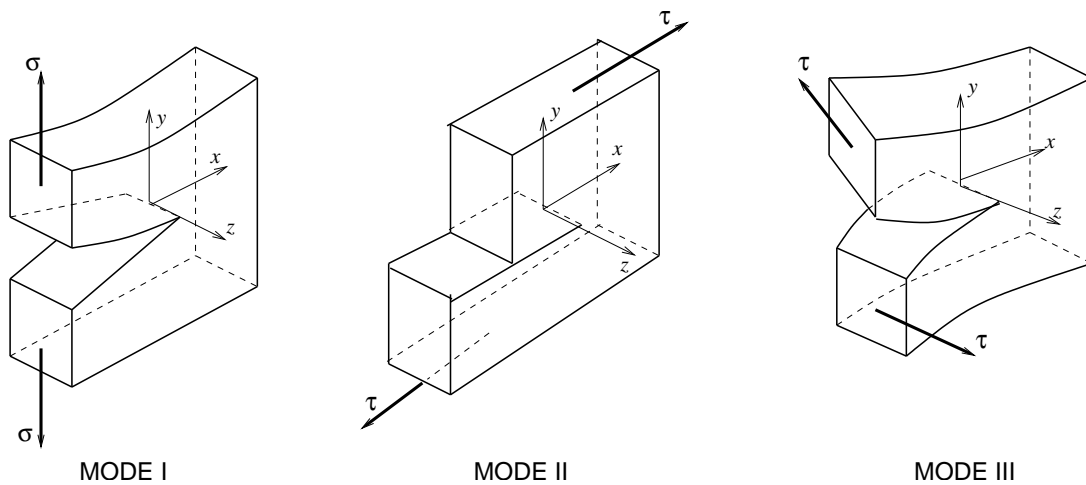


Figure 7.3. Three basic modes of crack surface displacements

Each of these modes of deformation correspond to a basic type of stress field in the vicinity of crack tip. Moreover, the stress field at the crack tip can be treated as one or a combination of the three types of stress fields, ([39]).

By using a method developed by Westergaard, 1939 [40], Irwin, 1957 [41] found that the stress and displacement fields in the vicinity of crack tips subjected to the three modes of deformation are given by:

- *Mode I*

$$\begin{aligned}
 \sigma_x &= \frac{K_I}{\sqrt{2\pi r}} \cos \frac{\theta}{2} \left[1 - \sin \frac{\theta}{2} \sin \frac{3\theta}{2} \right] \\
 \sigma_y &= \frac{K_I}{\sqrt{2\pi r}} \cos \frac{\theta}{2} \left[1 + \sin \frac{\theta}{2} \sin \frac{3\theta}{2} \right] \\
 \tau_{xy} &= \frac{K_I}{\sqrt{2\pi r}} \sin \frac{\theta}{2} \cos \frac{\theta}{2} \cos \frac{3\theta}{2} \\
 \sigma_z &= \nu(\sigma_x + \sigma_y), \quad \tau_{xz} = \tau_{yz} = 0 \\
 u &= \frac{K_I}{\mu} \sqrt{\frac{r}{2\pi}} \cos \frac{\theta}{2} \left[1 - 2\nu + \sin^2 \frac{\theta}{2} \right] \\
 v &= \frac{K_I}{\mu} \sqrt{\frac{r}{2\pi}} \sin \frac{\theta}{2} \left[2 - 2\nu - \cos^2 \frac{\theta}{2} \right] \\
 w &= 0
 \end{aligned}
 \tag{7.1}$$

- *Mode II*

$$\begin{aligned}
 \sigma_x &= -\frac{K_{II}}{\sqrt{2\pi r}} \sin \frac{\theta}{2} \left[2 + \cos \frac{\theta}{2} \cos \frac{3\theta}{2} \right] \\
 \sigma_y &= \frac{K_{II}}{\sqrt{2\pi r}} \sin \frac{\theta}{2} \cos \frac{\theta}{2} \cos \frac{3\theta}{2} \\
 \tau_{xy} &= \frac{K_{II}}{\sqrt{2\pi r}} \cos \frac{\theta}{2} \left[1 - \sin \frac{\theta}{2} \sin \frac{3\theta}{2} \right] \\
 \sigma_z &= \nu(\sigma_x + \sigma_y), \quad \tau_{xz} = \tau_{yz} = 0 \\
 u &= \frac{K_{II}}{\mu} \sqrt{\frac{r}{2\pi}} \sin \frac{\theta}{2} \left[2 - 2\nu + \cos^2 \frac{\theta}{2} \right] \\
 v &= \frac{K_{II}}{\mu} \sqrt{\frac{r}{2\pi}} \cos \frac{\theta}{2} \left[-1 + 2\nu + \sin^2 \frac{\theta}{2} \right] \\
 w &= 0
 \end{aligned}
 \tag{7.2}$$

- *Mode III*

$$\begin{aligned}
 \tau_{xz} &= -\frac{K_{III}}{\sqrt{2\pi r}} \sin \frac{\theta}{2} \\
 \tau_{yz} &= \frac{K_{III}}{\sqrt{2\pi r}} \cos \frac{\theta}{2} \\
 (7.3) \quad \sigma_x &= \sigma_y = \sigma_z = \tau_{xy} = 0 \\
 w &= \frac{K_{III}}{\mu} \sqrt{\frac{2r}{\pi}} \sin \frac{\theta}{2} \\
 u &= v = 0
 \end{aligned}$$

where the stress components, σ_{ij} , and the coordinates r and θ are shown in Figure 7.4; u , v , and w are the displacements in the x -, y -, and z -directions, respectively; ν is Poisson's ratio, and μ is the shear modulus of elasticity.

Note that dimensional analysis of Eqs. 7.1, 7.2, and 7.3 must be related to the magnitude of applied stress, and the square root of the crack length.

More details of the above with reference to the examples can be found in Tada et al. (1973) [31], Hertzberg (1996) [23], and Barsom and Rolfe (1999) [39].

7.3. J-integral

In the previous section, we have introduced the basic principles of the stress intensity factors (K).

The J -integral is widely accepted as a fracture mechanics parameter for both linear and nonlinear material response. It is related to the energy release associated with crack growth and is a measure of the intensity of deformation at a crack tip. Because of the importance of the J -integral in the assessment of flaws, its accurate numerical evaluation is

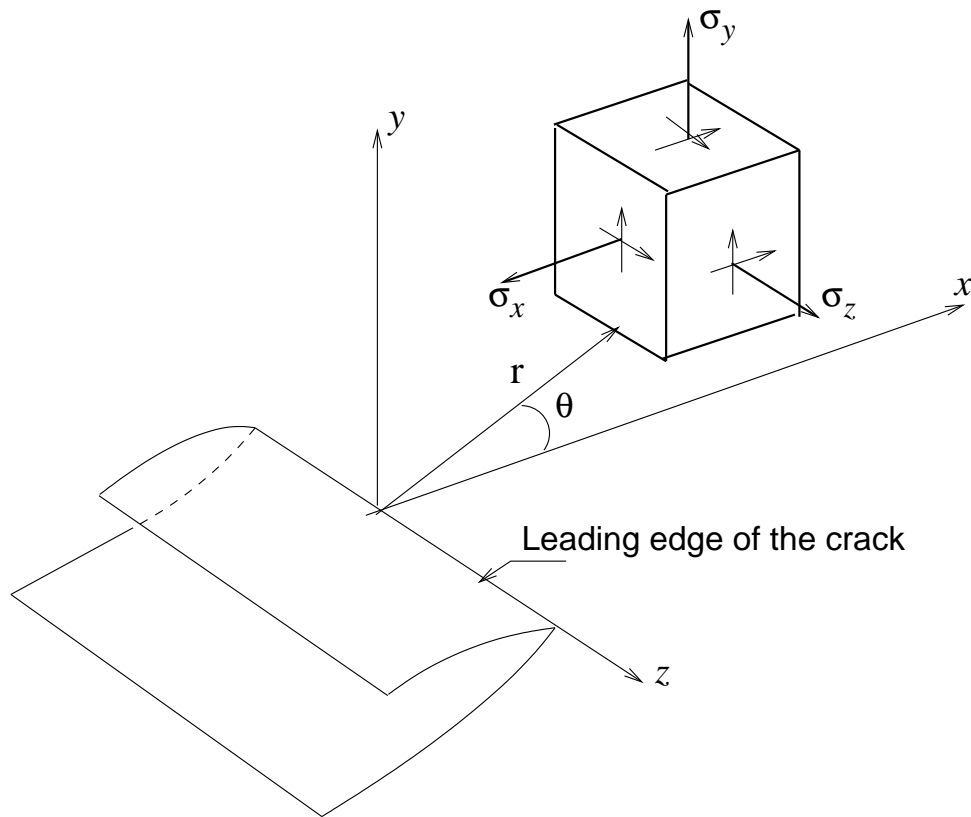


Figure 7.4. Stress components ahead of crack

vital to the practical application of fracture mechanics in design calculations. ABAQUS provides a procedure for such evaluation of the J -integral, based on the virtual crack extension/domain integral methods mentioned above. Further details can be found in Parks, 1977 [42], Shih, Moran, and Nakamura, 1986 [43], Moran and Shih, 1987 [28] and [29], and ABAQUS manuals (2003) [2].

For a two-dimensional, planar, using the small displacement gradient assumption and with body forces neglected, the path-independent J -integral is defined by (Rice, 1968 [44]),

$$(7.4) \quad J = \lim_{\Gamma \rightarrow 0} \int_{\Gamma} (W \delta_{1j} - \sigma_{ij} u_{i,1}) n_j d\Gamma$$

where, in a cracked body, Γ is the contour beginning at the bottom crack face and ending on the top face, as shown in Figure 7.5. Here, n_j is the outward normal to Γ , σ_{ij} the stress, u_i the displacement, $d\Gamma$ the increment of arc length along Γ and W the strain energy density.

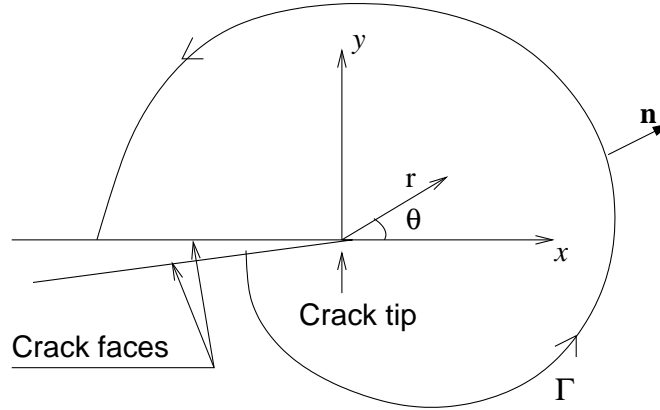


Figure 7.5. Contour for the evaluation of the J integral and crack tip coordinates

For numerical purposes, it is more advantageous to recast the line-integral (Eq. 7.4) as an area/domain integral. Such a representation is naturally suited for the finite element method.

As mentioned previously, a domain integral formulation has been detailed by Li *et al.* (1985) [45], Shih, Moran, and Nakamura, (1986) [43]), and Moran and Shih, (1987) [28] [29].

To obtain the desired domain representation for J , weighting functions q_i are introduced.

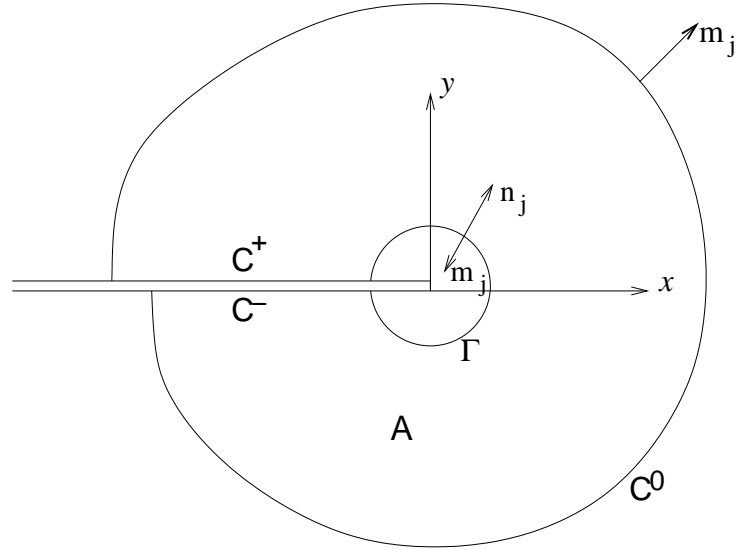


Figure 7.6. Convention at crack tip. Domain A is enclosed by Γ , C^+ , C^- , and C^0

For two-dimensional problems with the crack line oriented in the x -direction, q_1 is the only nonzero function and it has the value of *unity* on the contour Γ and *zero* on the outer contour C^0 (see Figure 7.6).

The integral in Eq. 7.4 can be restated as a line integral over the closed contour C , which consists of Γ , C^0 , and the crack faces C^+ and C^- , by

$$(7.5) \quad J = \int_C (W\delta_{1j} - \sigma_{ij} u_{i1}) m_j q_1 dC$$

here, m_j are the components of the unit vectors normal to C . On the contour Γ , m_j is equal to the negative of n_j which has been defined earlier in Eq. 7.4.

Applying the divergence theorem to Eq. 7.5, we obtain,

$$(7.6) \quad J = \int_A [\sigma_{ij} u_{i,1} - W \delta_{1j}] q_{1,j} dA$$

where A is the area enclosed by the closed contour C .

Assuming that,

$$(7.7) \quad P_{1j,j} q_1 = 0$$

It follows that,

$$(7.8) \quad \int_{\Omega} P_{1j,j} q_1 d\Omega = 0$$

$$(7.9) \quad \int_{\Omega} [(P_{1j} q_1)_{,j} - P_{1j} q_{1,j}] d\Omega = 0$$

With,

$$(7.10) \quad \int_{\Omega} P_{1j} q_{1,j} d\Omega = \int_{\partial\Omega} P_{1j} q_1 m_j dS$$

Thus,

$$(7.11) \quad \int_{\Omega} (P_{1j} q_1)_{,j} d\Omega - \int_{\partial\Omega} P_{1j} q_1 m_j dS = 0$$

Or,

$$(7.12) \quad \int_{\partial\Omega} P_{1j} q_1 m_j dS = \int_{\Omega} (P_{1j} q_1)_{,j} d\Omega$$

Now, we apply this equation to the line contours,

$$(7.13) \quad \int_{\Gamma_2} P_{1j} q_1 m_j dS + \int_{\Gamma_1} P_{1j} q_1 m_j dS + \int_{C^+} P_{1j} q_1 m_j dS + \int_{C^-} P_{1j} q_1 m_j dS = \int_{\Omega} (P_{1j} q_1)_{,j} d\Omega$$

Recalling that $q_1 = 0$ on the outer contour Γ_2 and $q_1 = 1$ on the inner contour Γ_1 . Thus,

$$(7.14) \quad \int_{\Gamma_2} P_{1j} q_1 m_j dS = 0$$

And,

$$(7.15) \quad \int_{\Gamma_1} P_{1j} q_1 m_j dS = \int_{\Gamma_1} P_{1j} m_j dS = -J$$

Therefore,

$$(7.16) \quad J = - \int_{\Omega} (P_{1j} q_1)_{,j} d\Omega + \int_{C^+} P_{1j} q_1 m_j dS + \int_{C^-} P_{1j} q_1 m_j dS$$

Or,

$$(7.17) \quad J = - \int_{\Omega} [W \delta_{1j} - \sigma_{ij} u_{i,1}] q_{1,j} d\Omega + \int_{C^+} P_{1j} q_1 m_j dS + \int_{C^-} P_{1j} q_1 m_j dS$$

7.4. Model validation

We have validated the FEA 3D model for the linear elastic analysis (Chapter 3) and the thermal model (Chapter 5). In a similar approach, we will conduct a series of tests to validate the 3D crack model. The tests include checking the validity of a simplified 3D model in which the geometry and results are available in literature. Among those most

commonly cited are the solutions to the problem of a planar elliptical cracks subjected to Mode I loading, provided by Raju and Newman (1979) [26].

7.4.1. Contour integral evaluation of a simplified 3D model

The geometry is shown in Figure 7.8. The model is loaded in Mode I by far-field tension. Due to symmetry, only one-quarter of the geometry needs to be analyzed. To simplify we will call our FEA model a *benchmark* model. We will compare the benchmark model versus Raju and Newman model (also called “Newman-Raju” in the plot). The comparison of the computed Mode I SIFs is shown in Figure 7.7.

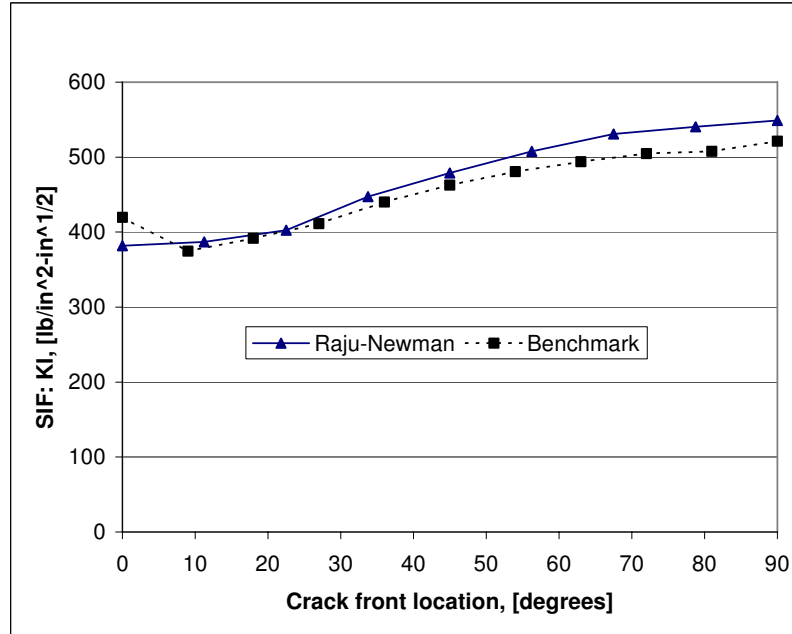


Figure 7.7. Comparison of computed Mode I stress intensity factors

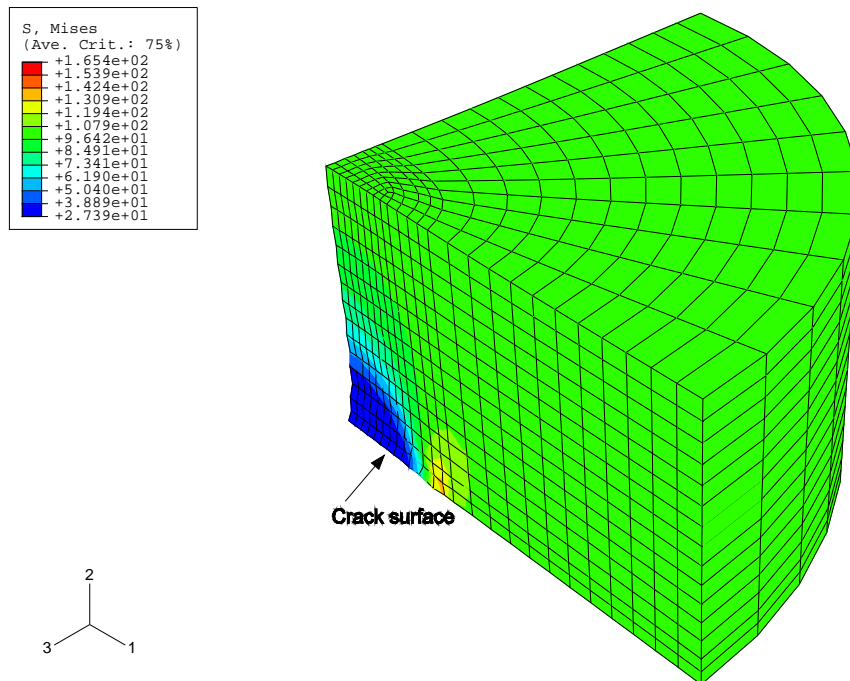


Figure 7.8. Mesh for semi-elliptic crack problem

The FEA stress intensity factors, K_I , along the crack line are compared with those obtained by Raju and Newman, 1979 [26] (Figure 7.7), who used a nodal force method to compute K_I from a finite element solution. The comparison shows good agreement between the results. Here, the J -integral values are converted to K_I using the formulation,

$$J = \frac{1 - \nu^2}{E} K_I^2$$

where ν is the Poisson's ratio and E is the Young's modulus.

It is important to note that our present benchmark model uses first-order reduced-integration brick element (C3D8R), similar to the bridge model. Consequently, by using the same type of element and the same type of meshing (without singular elements), we

can verify the accuracy level in 3D crack modeling applied to the bridge. Note that if we use rather a quadratic element (20-node element) and singular elements with mid-side nodes moved to the quarter position on element edges that focus onto the crack tip nodes, the FEA results are very closed to the reference results.

The main reasons are:

- For a multi-body contact problem; i.e. joint connection of the bridge, the first-order brick element (8-node element) is recommended. The K_I values provided by 8-node brick element show some “oscillation” at the beginning of the crack front. This minor loss of accuracy is assumed to be attributable to the type of element used (linear rather than quadratic) and without singular type of element. However, the final results, as depicted in Figure 7.7, are reasonably closed to the reference model (as suggested by Raju and Newman (1979) [26]). They are about 8% for $\phi = 0^\circ$ and 5% for $\phi = 90^\circ$.
- The current version of ABAQUS, (ABAQUS 6.4-5, 2003) [2], does not have the capability to produce automatically the singular elements near the crack tip with the pre-processor ABAQUS/CAE. An alternative solution is to mesh by hand. However, due to the complex geometry of the bridge model, this alternative is not feasible.

7.5. FEA prediction of the mixed-mode SIFs on operating conditions

Let us recall the operating conditions mentioned previously:

- unlocked condition
- locked condition

Note that “locked” condition signifies no relative motion is allowed between part components; e.g. web girder and pin and hanger plate and pin. This means that each pair of them is assumed to stick together in perfect “bonding”. This particular condition is used to simulate the existence and formation of the “pack-rust” inside the joints.

7.5.1. Unlocked conditions

In this section, the elements of the connection are allowed to move freely relative to each other. This is an *idealistic* condition which pertains mostly to the *new* bridges. However, for aging bridges, there are some degrees of “lockup” inside the joint connections.

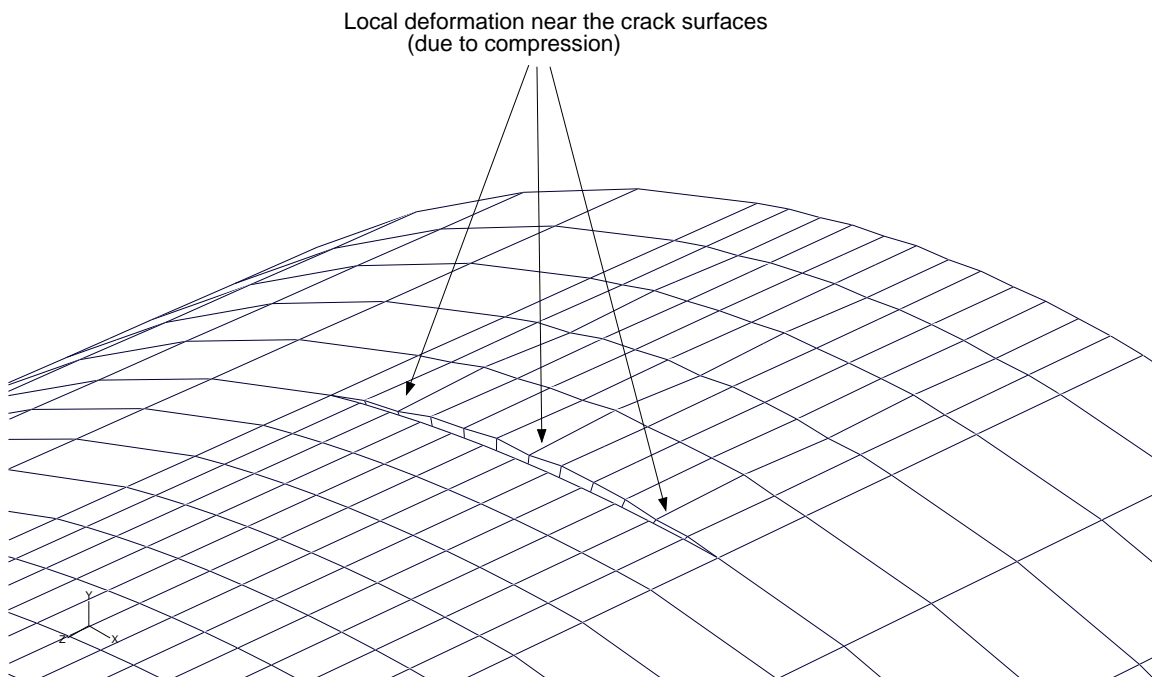


Figure 7.9. Local deformation near the crack surfaces due to compression (bottom pin)

7.5.1.1. Effects of temperature changes. The main objective here is to explore whether there are *linear* relationships between the temperatures and the stress intensity factors. Remember that bridge elements expand and contract due to temperature changes (daily and seasonal changes). In the present model, the initial (or ambient temperature) was set to be $T_0 = 59^\circ \text{ F}$ (15° C). Then, we increase linearly the temperatures; e.g. $T = 86^\circ \text{ F}$ (30° C), and $T = 113^\circ \text{ F}$ (45° C). We would expect to obtain the linear relationships of the stress intensity factors based on these differential temperatures.

The American Association of State Highway and Transportation Officials specification (AASHTO (1996) [11]) provides temperature variations depending on whether the structure is in a *moderate* or *cold* climate region. For steel bridge structure similar to this one, the values are given in the form of extreme cold and hot temperatures. The ranges are -30° F (-34.4° C) and 120° F (48.9° C) (see Table 7.1).

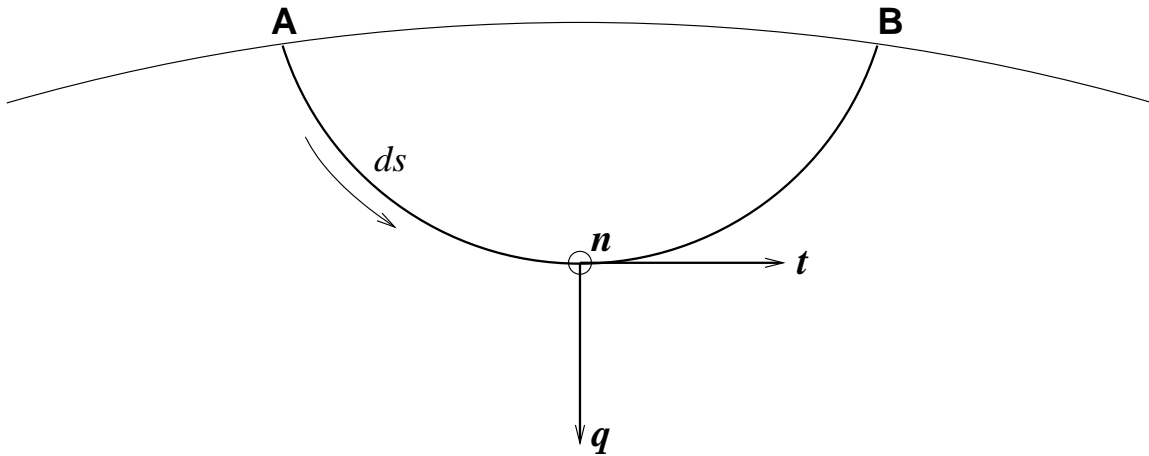
Table 7.1. AASHTO temperature ranges

	From	To
Moderate climate	0° F	120° F
Cold climate	-30° F	120° F

The FEA results are shown in Figures 7.12, 7.13, 7.14, and 7.15. The plots indicate that the stress intensity factors increase when the temperature increase. These are mainly due to the movements of the bridge components as a result of their expansions or contractions. In addition, we also found that there is a linearity in the effective stress intensity factor (K_{eff}) versus temperature (see Figure 7.15).

The definition of local orthogonal cartesian coordinates at the point s on the crack front is illustrated in Figure 7.10. The schematic representation shows the the unit vectors

\mathbf{q} , \mathbf{t} , \mathbf{n} along the crack front. The unit vector \mathbf{q} is normal to crack front, \mathbf{t} is tangent to crack front, and \mathbf{n} is perpendicular to plane of crack. The crack dimensions are: $a = 0.236$ in. (6 mm), $c = 0.54$ in. (13.66 mm), and $D = 6.5$ in. (165.1 mm).



\mathbf{q} , \mathbf{t} , \mathbf{n} unit vectors along the crack front

Figure 7.10. Definition of local orthogonal coordinates on the crack front: \mathbf{q} , \mathbf{t} , and \mathbf{n}

To account for the mixed-mode stress intensity factors, the effective stress intensity, K_{eff} , is given by Hanson *et al.* (1992, [46]):

$$K_{eff} = \sqrt{K_I^2 + K_{II}^2 + \frac{1}{1-\nu} K_{III}^2}$$

7.5.2. Locked conditions

The stress-intensity factors (SIFs) versus temperature histories in frozen condition are illustrated in Figures 7.16, 7.17, and 7.18. Resistance to the motion is caused by the high friction between the pin and other elements in the connection. These plots suggested that

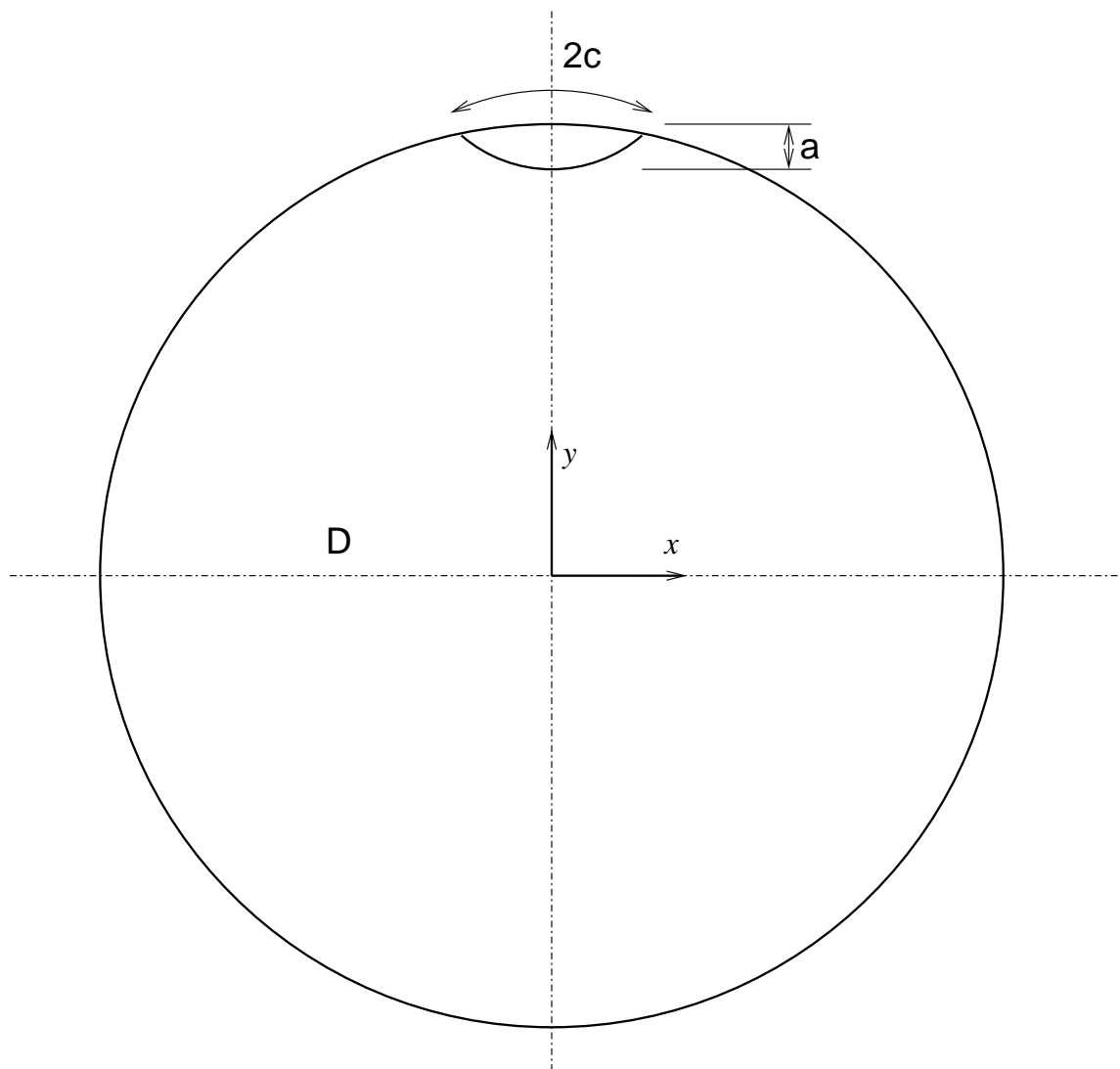


Figure 7.11. Initial crack dimensions: $a=6$ mm, $c=13.66$ mm, $D=165.1$ mm

the highest SIFs in frozen (or locked) condition are approximately twice those of the SIFs in the unlocked condition. When a structure component is not free to expand, a change in temperature will cause significant stress and introduces strain energy that will result in an increase in the total energy in the model.

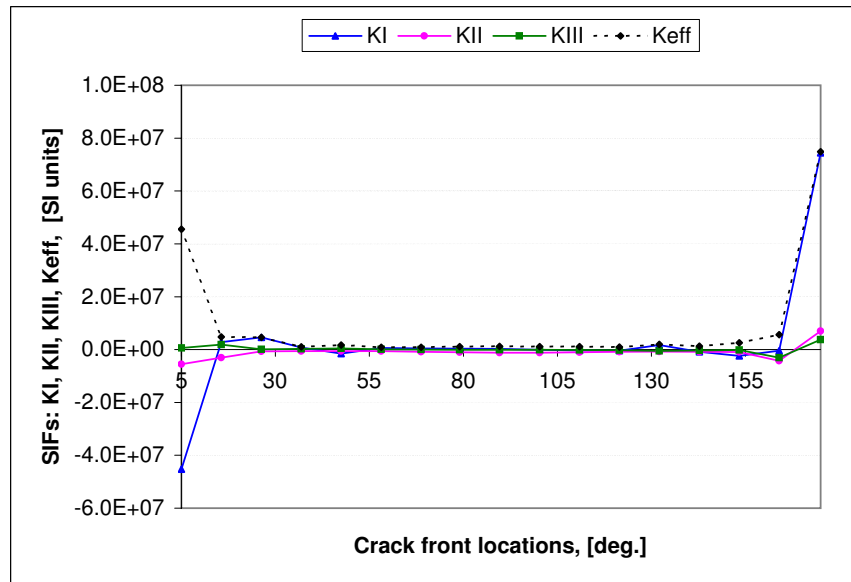


Figure 7.12. Mixed-mode SIFs (unlocked) for temperature $T = 15^\circ \text{C}$ ($T = 59^\circ \text{F}$)

Note the high torsion response on the pin surface due to frozen (locked) condition. Also note the difference movement between expansion and contraction.

7.6. Concluding remarks

The above results suggest that the mixed-mode stress intensity factors K_I , K_{II} , and K_{III} are higher at the beginning and at the end of the crack front. The highest values on these locations are mainly due to the direct contact pressure (compression) applied by the web girder to the pin. However, in the center portion along the crack front, the SIFs are much lower (far away from the direct contact pressure). Furthermore, the SIFs are fairly linear versus temperatures in unlocked conditions. They are not in locked conditions.

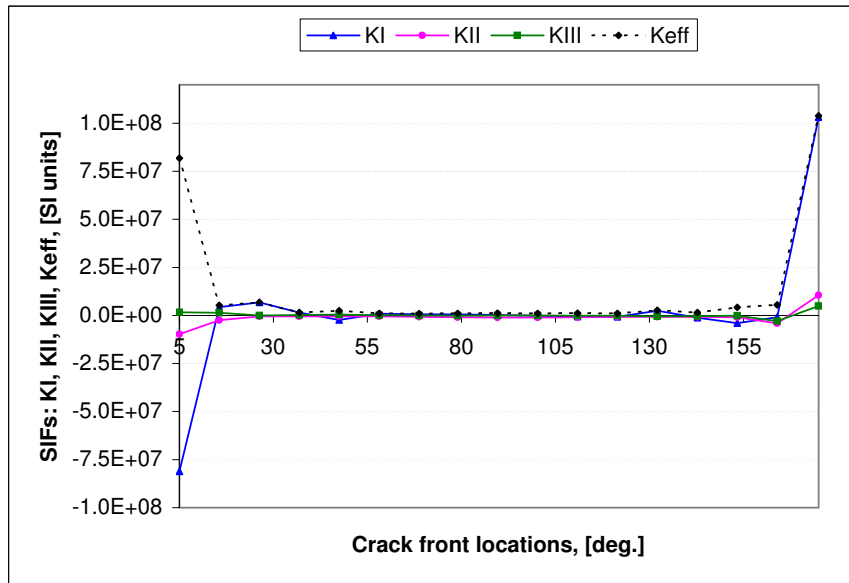


Figure 7.13. Mixed-mode SIFs (unlocked) for temperature $T = 30^{\circ}\text{C}$ ($T = 86^{\circ}\text{F}$)

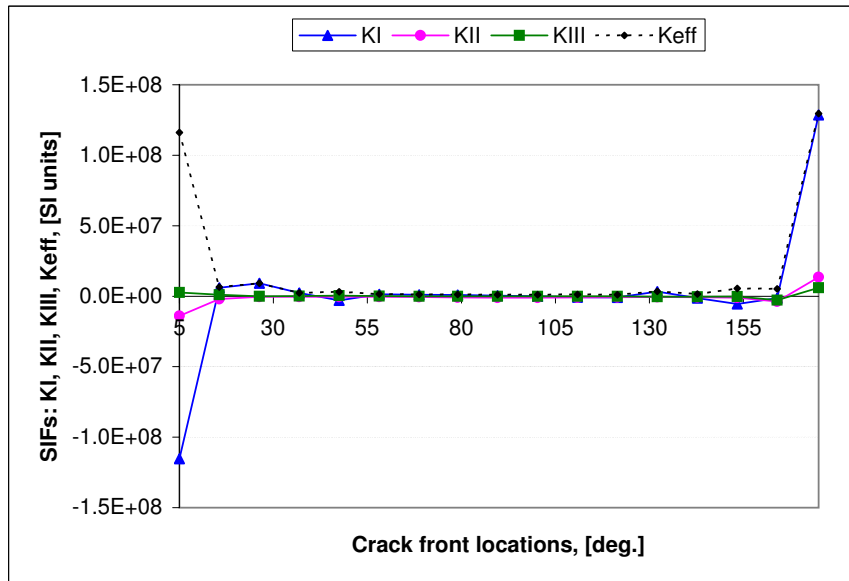


Figure 7.14. Mixed-mode SIFs (unlocked) for temperature $T = 45^\circ \text{C}$ ($T = 113^\circ \text{F}$)

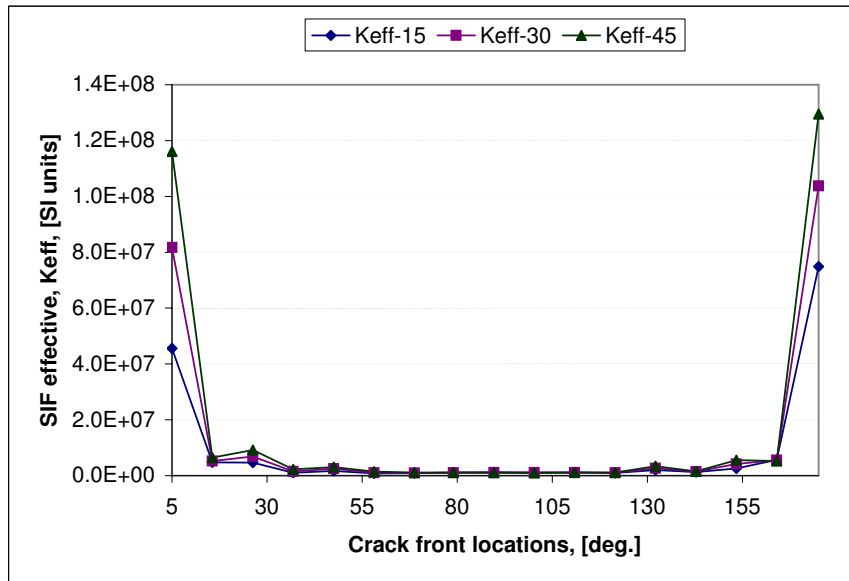


Figure 7.15. Effective SIF (unlocked), K_{eff} for different temperatures

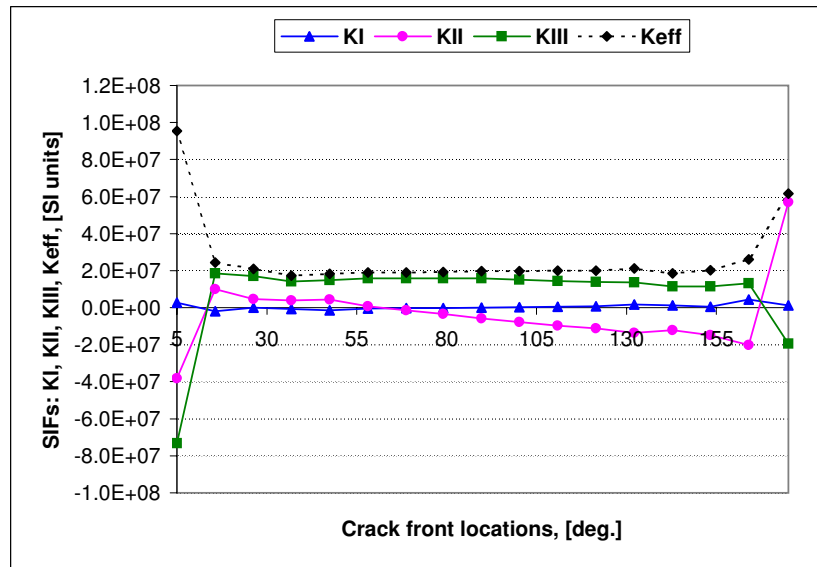


Figure 7.16. Mixed-mode SIFs (locked) for temperature $T = 15^\circ \text{C}$ ($T = 59^\circ \text{F}$)

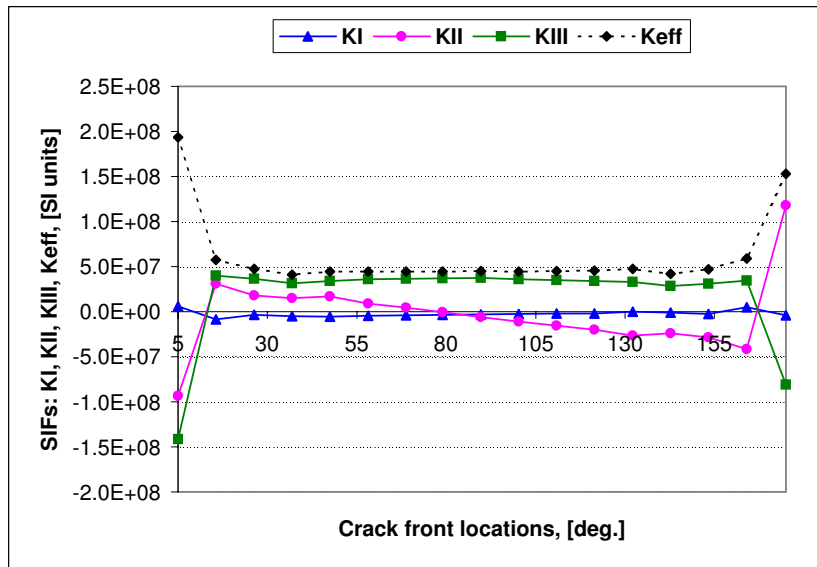


Figure 7.17. Mixed-mode SIFs (locked) for temperature $T = 30^\circ \text{C}$ ($T = 86^\circ \text{F}$)

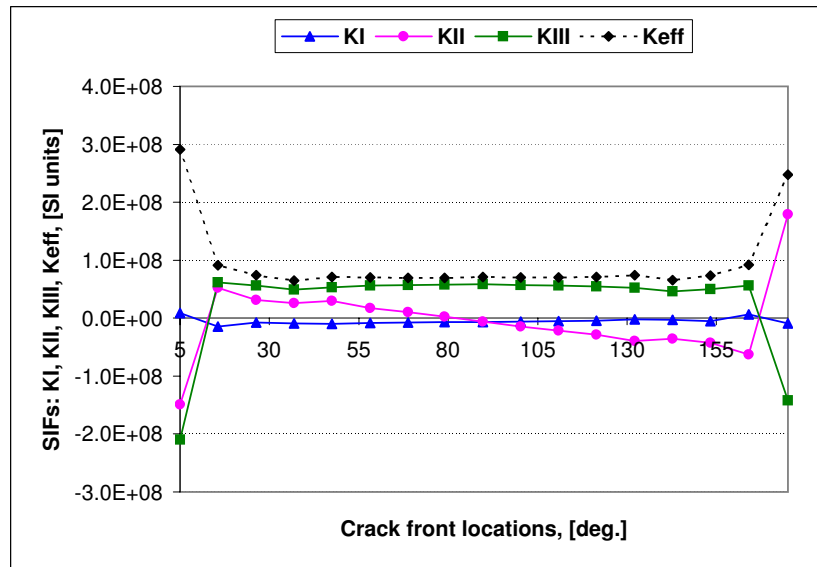


Figure 7.18. Mixed-mode SIFs (locked) for temperature $T = 45^\circ \text{C}$ ($T = 113^\circ \text{F}$)

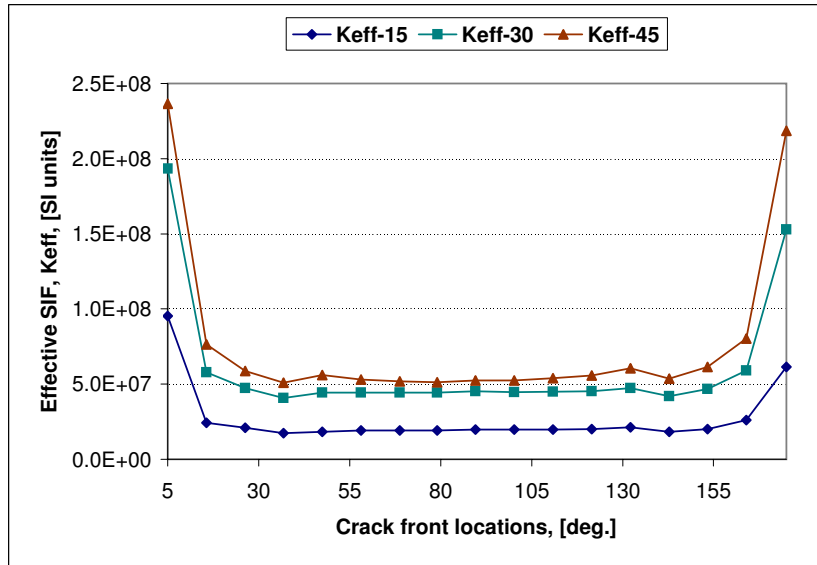


Figure 7.19. Effective SIFs (locked) for different temperatures

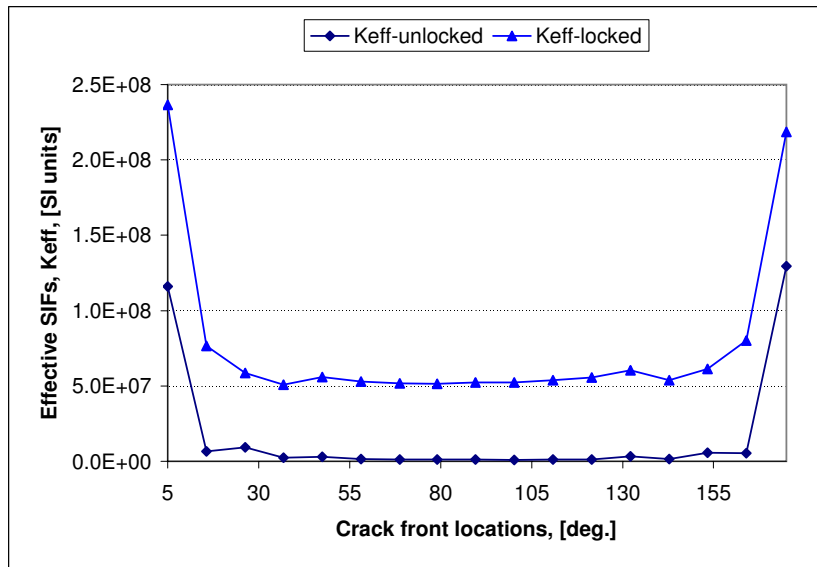
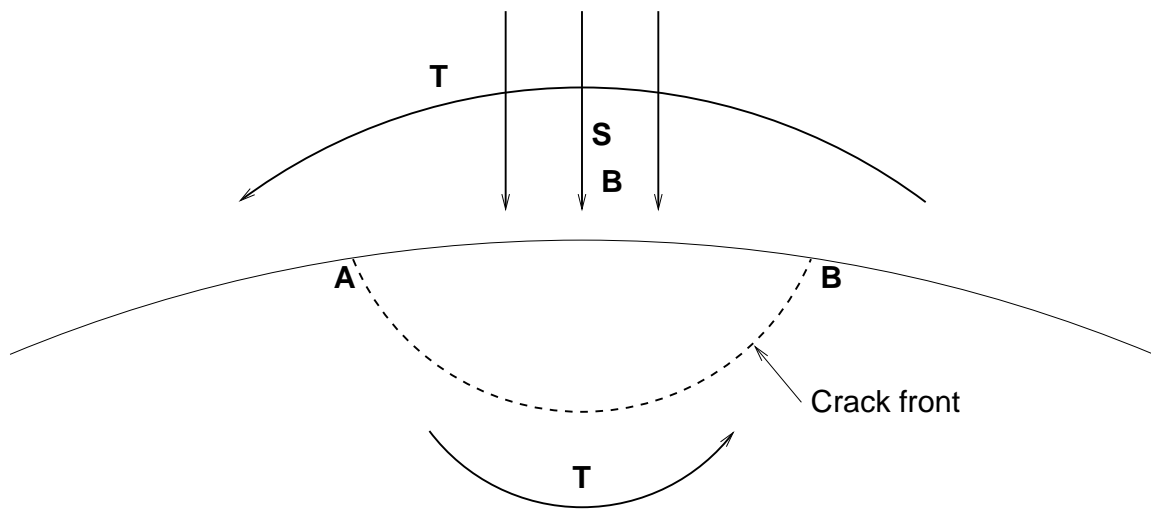


Figure 7.20. Comparison between effective SIFs between unlocked and locked conditions



Combined loading: Torsion, Shear, Bending

Figure 7.21. Schematic diagram of the combined loading

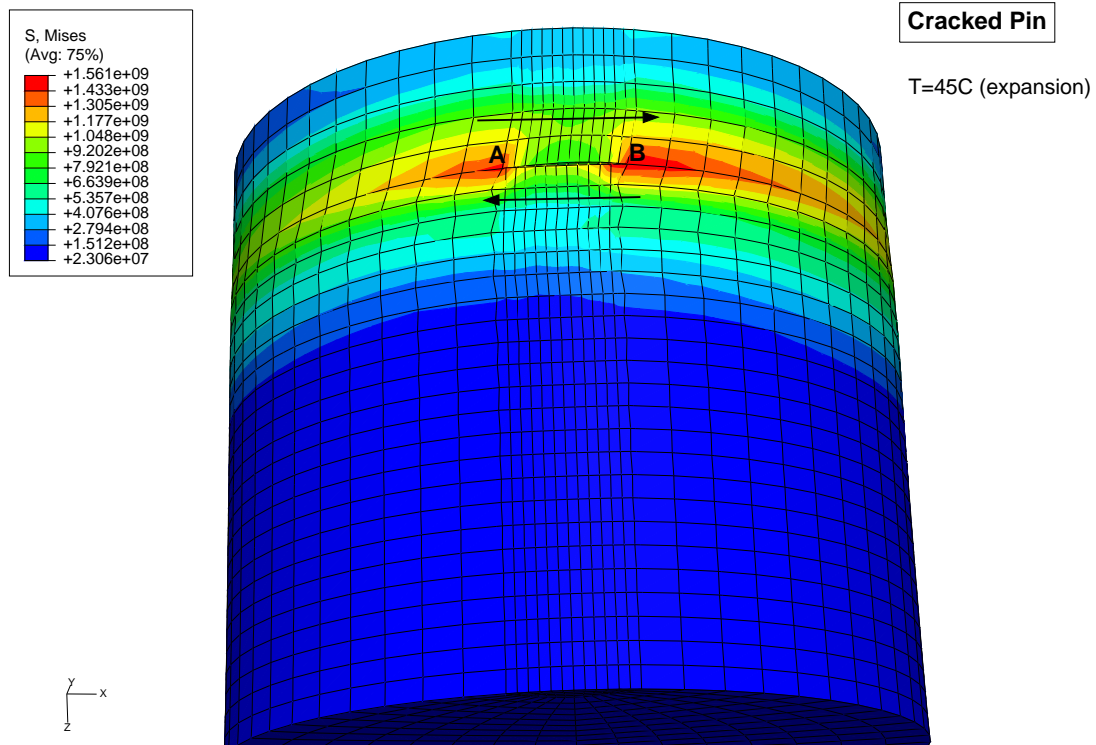


Figure 7.22. Stress contour for a temperature $T=45\text{C}$

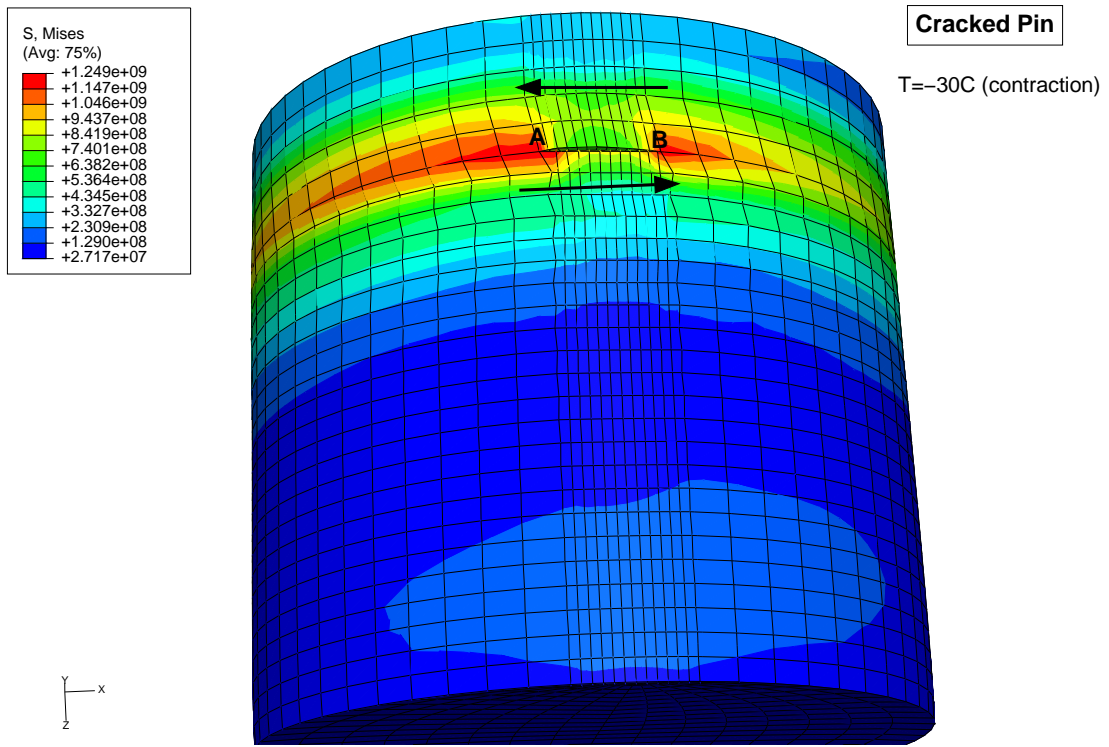


Figure 7.23. Stress contour for a temperature $T=-30C$

CHAPTER 8

Computational modeling of fatigue crack growth**8.1. Introduction**

This chapter investigates computational modeling of fatigue crack growth in the cylindrical shaped pin, which is one of the critical components of the joint connection. It should be noted that crack growth simulation is the process of modeling crack evolution in a structure. This includes all aspects of the modeling process from initial model preparation to visualization of results. This leads to the prediction of crack growth and the evaluation of structural integrity. Therefore, crack growth simulation is an incremental process, where a series of steps is repeated. Although, ABAQUS has an automatic mesh generation capability (ABAQUS/CAE), construction of a proper 3D crack model requires some human intervention and certain skills from the analyst.

In the simulation of the fatigue crack propagation, stress intensity factors (SIFs) are required for use in the crack growth law. The SIFs, computed in the previous Chapter, are augmented here by an algorithm to calculate crack growth, under cyclic loading. The computation of the SIFs along the three-dimensional crack front remains a challenging problem. This is primarily due to the fact that accurate calculation of stress intensity factors (SIFs) in engineering applications has been a non-trivial task.

Prior to this study, there were not many examples of 3D crack growth work on cylindrical pin with transverse crack. Furthermore, moving and combined loads due to multibody

contacts had not been considered in these previous analyses. The absence of closed-form solutions add to the list of difficulty during the investigation.

Motivated by this challenging problem and its difficulty, and a number of other similar problems in industry, several enhancements have been made. These include add-on tools for evaluating the crack growth.

8.2. Computational procedure for evaluating the crack growth

The basic procedure for estimating the fatigue life of a structure from a fracture mechanics approach is to first estimate the initial crack geometry and the critical crack size. Next, the number of cycles required to grow the crack from the initial size to the critical size is calculated. Once the number of load cycles is known, the time required to accumulate that many cycles is calculated from the average daily truck traffic. It takes time for a fatigue crack to develop. But a crack can then expand rapidly to become a fracture.

8.3. Crack growth simulation in ABAQUS

As mentioned before, the version of ABAQUS (version 6.4.5) [2], used in this investigation, does not have crack propagation capabilities in 3D. Therefore, an alternative approach was used. Our current approach consists in creating add-on tools, which combine with the Paris's power law for fatigue crack growth, to be used in conjunction with the ABAQUS program. Fatigue crack growth rates were correlated with the stress intensity factor ranges.

Although, ABAQUS has an automatic mesh generation capability (ABAQUS/CAE), construction of a proper 3D crack model requires some human intervention. Considering

the complexities involved in fatigue modeling in engineering applications, the predictions of the finite element analysis (FEA) appear to be reasonable in an engineering sense.

8.4. Fatigue crack growth

Figure 8.1 illustrates the initial crack geometry. The elevation view shows the initial crack on the pin surface, located on the shear plane between the suspended web-girder and the hanger plate. Due to cyclic loading generated by the traffic, this crack can grow over a period of time until the crack extends through the pin section. This can lead to catastrophic consequences, as we mentioned earlier.

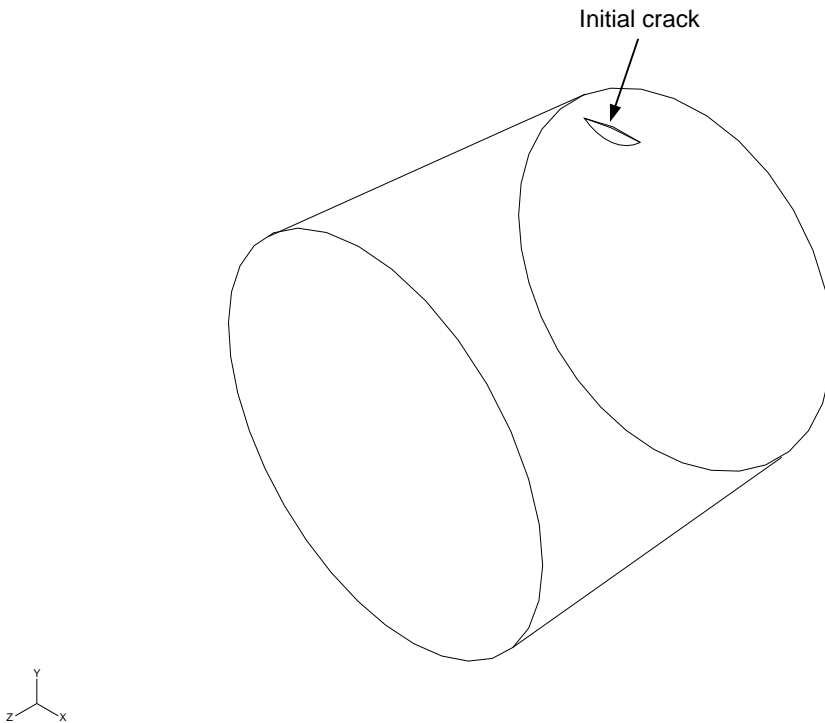


Figure 8.1. Initial crack profile embedded on the pin surface

8.4.1. Crack growth analysis procedure

Fatigue crack growth was predicted on a step-by-step basis from the Paris law, $da/dN = C(\Delta K)^m$, where C and m are material constants. It should be noted that Paris's law only represents the linear phase of crack growth curve.

In U.S. customary units, the above expression becomes,

$$(8.1) \quad \frac{da}{dN} = 3.6 \times 10^{-10}(\Delta K)^3$$

where da/dN = fatigue crack growth per cycle of loading (*in/cycle*) and ΔK = stress intensity factor range (*ksi* $\sqrt{\text{in}}$). Here, $C = 3.6 \times 10^{-10}$ and $m = 3$ which corresponds to the ferrite-pearlite steels (for example, ASTM A36) at room temperature, ([39]).

Similarly, in SI units, the above expression becomes,

$$(8.2) \quad \frac{da}{dN} = 6.9 \times 10^{-30}(\Delta K)^3$$

where da/dN = fatigue crack growth per cycle of loading (*m/cycle*) and ΔK stress intensity factor range (*Pa* $\sqrt{\text{m}}$).

Distinctly different C values have resulted depending on the system of units used. In this study and to be consistent with other data, the SI units are employed.

The numerical procedure to estimate the growth of the crack front is as follows:

- (1) Determine the stress intensity factors, K_I , K_{II} , K_{III} , and K_{eff} along the crack front for the current loading cycle and temperature.
- (2) Use the Paris law for the mixed-mode crack propagation to calculate the growth rate, da/dN , at a finite number of points along the crack front.

- (3) Assign the number of cycles, ΔN .
- (4) The increase in crack length da is then computed along the crack front.
- (5) To determine the *new* front of the crack, we need to calculate the coordinates of a vector normal of a finite number of points along the crack front. The details can be found in the following section.
- (6) Similarly, to determine the positions of the end points (on the circle), we need to calculate their coordinates by using polar coordinates. Further details can be found in the subsequent section as well.
- (7) Repeat (1)-(6) for the evolving crack.

As discussed above, the rate of fatigue crack growth under cyclic loading can be expressed in terms of range of stress intensity factor through Paris's power law (Paris, 1963 [47]),

$$(8.3) \quad \frac{da}{dN} = C(\Delta K_{eff})^m$$

where C and m are 2 coefficients which depend on the material resistance. N is the cycle number. For a mixed-mode loading, the range of the *effective* stress intensity factor, K_{eff} , is used, which can be obtained according to the expression,

$$(8.4) \quad \Delta K_{eff} = \sqrt{\Delta K_I^2 + \Delta K_{II}^2 + \frac{1}{1-\nu} \Delta K_{III}^2}$$

where ΔK is the difference between maximum and minimum stress intensity factors during a loading cycle. The equation (8.3) implies that da/dN depends on ΔK_{eff} only, where

$$(8.5) \quad \Delta K_{eff} = \sqrt{\Delta K_I^2 + \Delta K_{II}^2 + \frac{1}{1-\nu} \Delta K_{III}^2}$$

$$(8.6) \quad \frac{da}{dN} = C(\Delta K_{eff})^m$$

$$(8.7) \quad \Delta a_k = C(\Delta K_{eff}^k)^m \quad k = 1, \text{ npoints}$$

$$(8.8) \quad \Delta N = \frac{(\Delta a)_{max}}{C(\Delta K_{eff}^{max})^m}$$

8.4.2. New contour crack front computations

This section describes the integration of add-on tools to be used in conjunction with the ABAQUS program.

As mentioned earlier, in order to determine the new crack front, we first need to calculate the coordinates of a vector normal to a parabolic section. The parabola is an approximated curve of the crack front. It is defined by 3 points on a plane. We need to calculate the coordinates of the end points of the normal vector. These will be combined to the increase in crack length Δa , previously calculated.

8.4.2.1. New crack front normal positions. In order to determine the coordinates of the points which constitute the new crack front, we need to calculate the coordinates of a vector normal to a parabola (Figure 8.3), which represents the current position of the crack front.

The equation of the parabola is $y = ax^2 + bx + c$. Let us set up three equations in three unknowns using the coordinates of three points; i.e. points 1, 2, and 3:

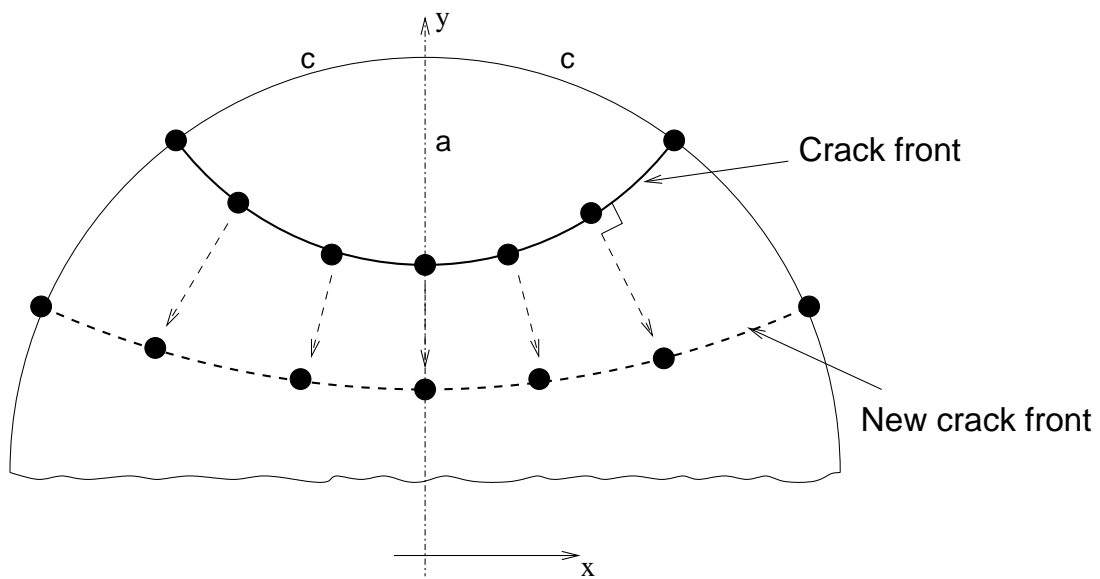


Figure 8.2. Schematic representation of the new crack front

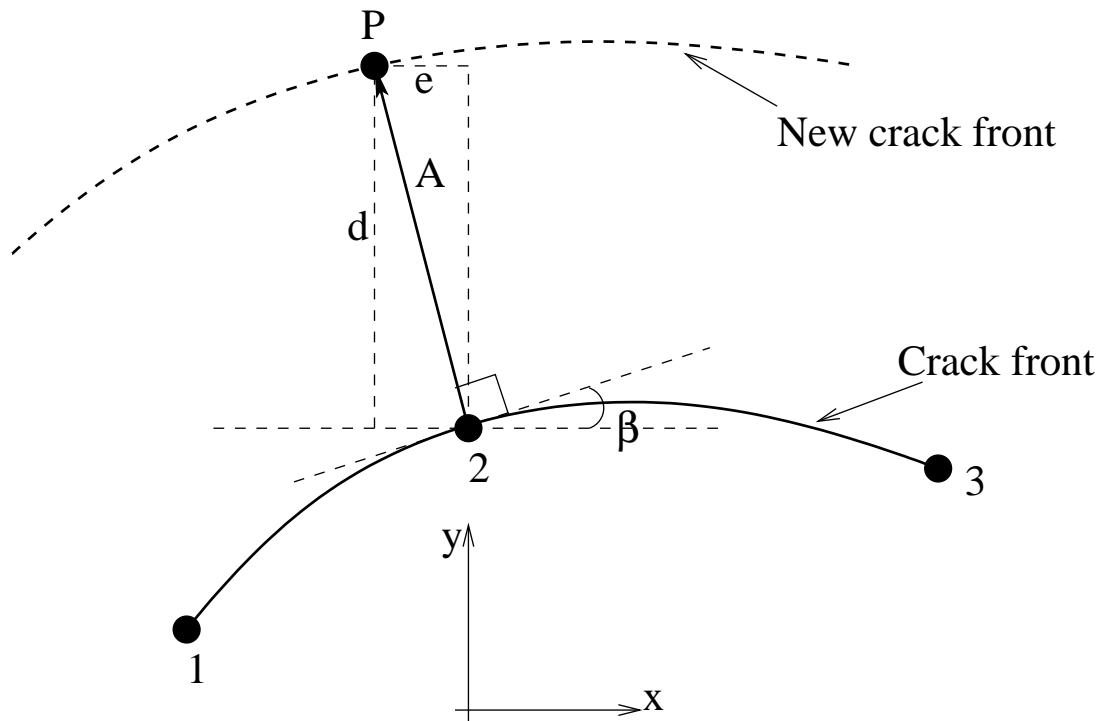


Figure 8.3. Schematic of the normal positions to the crack front

$$\begin{cases} y_1 = ax_1^2 + bx_1 + c \\ y_2 = ax_2^2 + bx_2 + c \\ y_3 = ax_3^2 + bx_3 + c \end{cases}$$

Now, let us solve these 3 equations for the unknowns, a , b , and c . From the calculus, the slope m of the parabola at (x_2, y_2) is defined as,

$$m = 2ax_2 + b = \tan \beta$$

For notations used here, refer to Figure 8.3,

$$d = A \cos \beta$$

$$\sin^2 \beta + \cos^2 \beta = 1$$

$$\tan^2 \beta + 1 = \frac{1}{\cos^2 \beta}$$

$$\begin{aligned} \cos \beta &= \frac{1}{\sqrt{1 + \tan^2 \beta}} \\ &= \frac{1}{\sqrt{1 + m^2}} \end{aligned}$$

Since,

$$d = A \cos \beta$$

Thus,

$$\begin{aligned} d &= A \cos \beta \\ &= \frac{A}{\sqrt{1+m^2}} \end{aligned}$$

Similarly,

$$\begin{aligned} e &= A \sin \beta \\ &= Am \times \frac{1}{\sqrt{1+m^2}} \\ &= md \end{aligned}$$

Depending on whether the normal has a positive or negative y component determines whether the end point of the normal will be,

$$\begin{cases} x_N = x_2 - md \\ y_N = y_2 + d \end{cases}$$

or whether,

$$\begin{cases} x_N = x_2 + md \\ y_N = y_2 - d \end{cases}$$

8.4.2.2. New crack front end-points located on the circle. In order to determine the positions of the end points located on the circle section, we use an approach which consists to express the coordinates of these points in polar coordinates (see Figure 8.4).

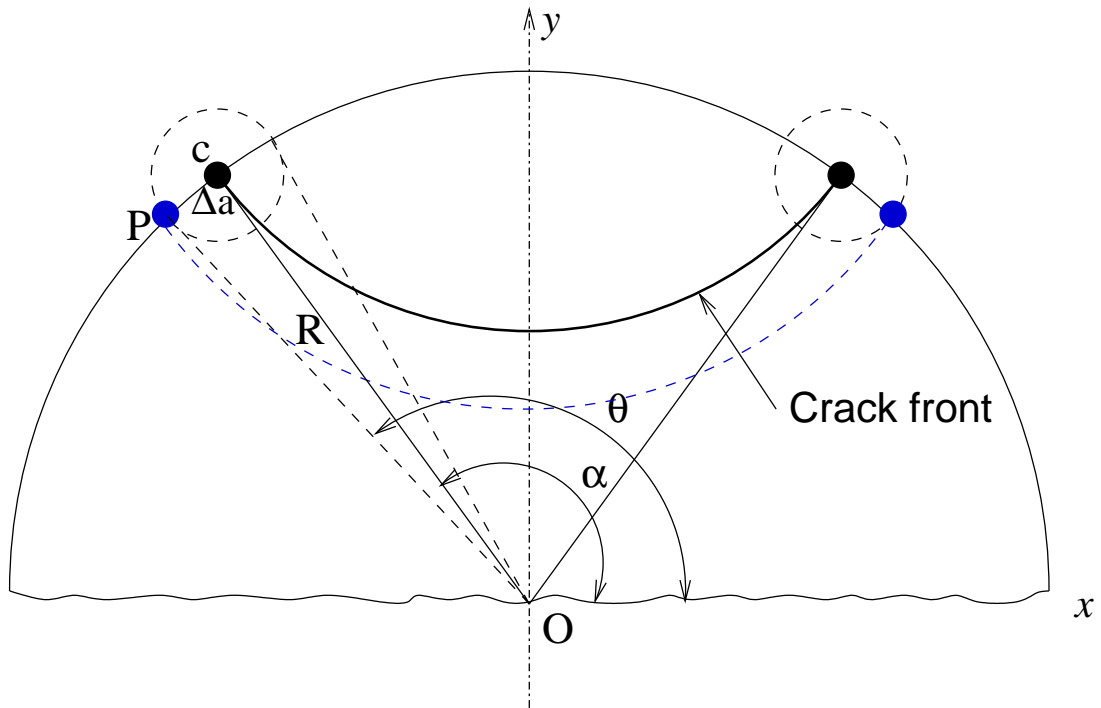


Figure 8.4. New crack front end-points located on the circle

The coordinates of point c are,

$$\begin{cases} x_c = x_0 + R \cos \alpha \\ y_c = y_0 + R \sin \alpha \end{cases}$$

Similarly, the coordinates of point P are,

$$\begin{cases} x_P = x_0 + R \cos \theta \\ y_P = y_0 + R \sin \theta \end{cases}$$

The increase in crack length Δa is then computed as,

$$\begin{aligned} (x_P - x_c)^2 + (y_P - y_c)^2 &= \Delta a^2 \\ (x_0 + R \cos \theta - x_0 - R \cos \alpha)^2 + (y_0 + R \sin \theta - y_0 R \sin \alpha)^2 &= \Delta a^2 \\ R^2 [(\cos \theta - \cos \alpha)^2 + (\sin \theta - \sin \alpha)^2] &= \Delta a^2 \\ \cos(\theta - \alpha) &= 1 - \frac{\Delta a^2}{2R^2} \end{aligned}$$

Hence,

$$\theta = \alpha \pm \cos^{-1} \left(1 - \frac{\Delta a^2}{2R^2} \right)$$

Therefore, the coordinates of the new end-points located on the circle are,

$$\begin{cases} x_P = x_0 + R \cos \theta \\ y_P = y_0 + R \sin \theta \end{cases}$$

8.4.3. Results

This section illustrates the results of the computations using the step-by-step procedure, as previously described, to predict the fatigue crack growth in the pin component.

The main question concerning fatigue crack growth is “how long does it take for a crack to grow from a certain initial size (a_0) to a critical size (a_{cr})?” The initial crack size, a_0 , typically corresponds to the size that can be detected using non-destructive inspection techniques (NDT). The critical size may be the size at which the stress intensity factor exceeds the fracture toughness at some point along the crack front or it may be some predetermined size for assessment and comparative purposes.

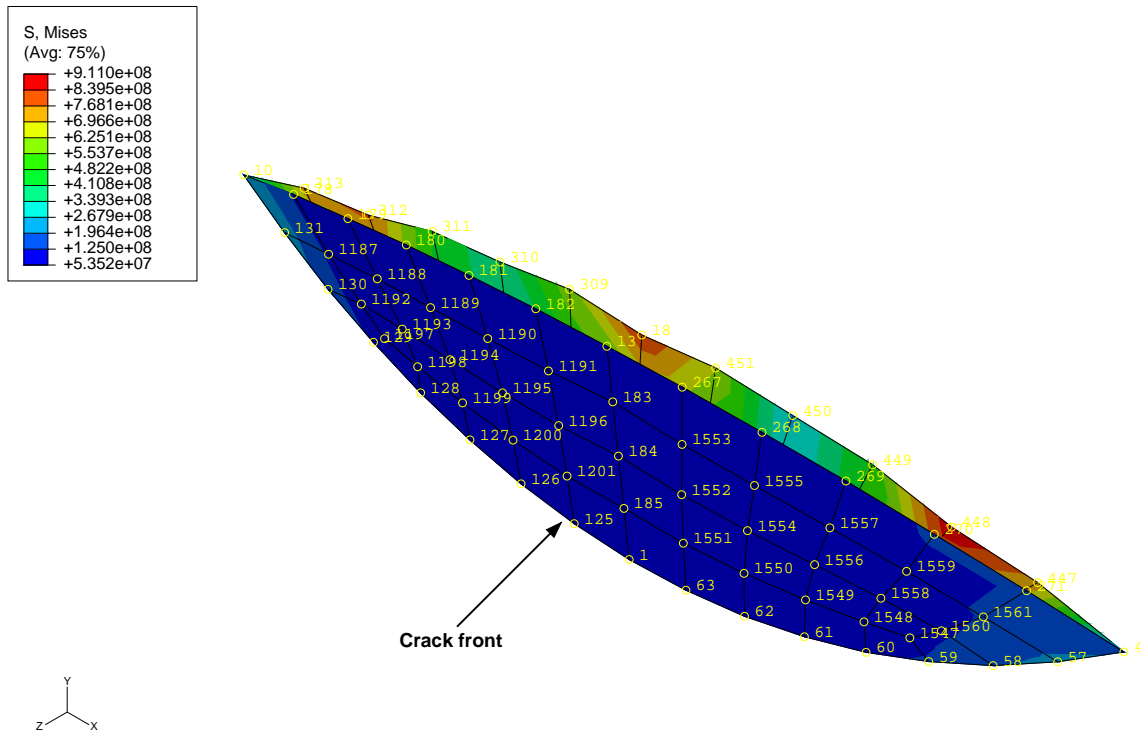


Figure 8.5. Crack surfaces

8.4.3.1. Prediction of fatigue crack growth. As said before, the criterion of crack propagation is based on the Paris law (Paris, 1963 [47]). To account for the mixed-mode propagation, the stress intensity factor is given by:

$$\Delta K_{eff} = \sqrt{(K_I^{(1)} - K_I^{(0)})^2 + (K_{II}^{(1)} - K_{II}^{(0)})^2 + \frac{1}{1 - \nu} (K_{III}^{(1)} - K_{III}^{(0)})^2}$$

where ΔK is the difference between the maximum and the minimum stress intensity factors during a loading cycle. Here, the maximum corresponds to the total load, which includes dead load, live load, and thermal load. The minimum corresponds to the dead load.

Once the constants m and C are known, for example for a structural steel construction, the Paris power law (in SI units) becomes:

$$\begin{aligned}\frac{da}{dN} &= C(\Delta K_{eff})^m \\ &= 6.9 \times 10^{-30}(\Delta K)^3\end{aligned}$$

in which, $C = 6.9 \times 10^{-30}$ and $m = 3$.

The scheme for growth of a plane crack proposed for the solution of the present study is similar to those used by Hanson and Keer (1992) [46]. It consists of the following steps:

- (1) Determine ΔK_{eff} along the crack front during a loading cycle.
- (2) Calculate the crack length $\Delta a_i/\Delta N_i$ for a finite number of points (or nodes) on the crack front.
- (3) Determine the new contour shape of the crack using the formulations described in the previous section (see “New contour crack front computations”), using the coordinates of stationary points.
- (4) Repeat 1-3 and introduce new cycles ΔN .
- (5) Sum the values of ΔN .

8.4.3.2. Initial state or stage no. 1. Table 8.1 shows the results of the initial state: ΔK_{eff} and crack growth increments Δa_i for a cycle $\Delta N = 1$. Note that the crack growth increments Δa_i have to be in meters (m) because of the units for ΔK_{eff} ($\text{MPa}\sqrt{\text{m}}$). Note that the node numbers along the contour crack front are: 10, 131, ..., 57, 4 (see Figure 8.5). A higher ΔK_{eff} gives rise to a higher crack growth rate (at the edges of the flaw, i.e.

Table 8.1. Determination of ΔK_{eff} and Δa_i along the crack front ($\Delta N = 1$)

Node	ΔK_{eff} [MPa \sqrt{m}]	Δa_i [m]
10	30.68	1.9936E-07
131	1.70	3.3747E-11
130	1.91	4.8310E-11
129	0.65	1.9346E-12
128	0.64	1.8577E-12
127	0.33	2.5032E-13
126	0.24	9.2907E-14
125	0.15	2.4409E-14
1	0.13	1.6382E-14
63	0.19	4.5544E-14
62	0.27	1.4089E-13
61	0.35	3.0730E-13
60	0.43	5.6805E-13
59	0.38	3.9501E-13
58	1.50	2.3293E-11
57	0.81	3.7459E-12
4	28.48	1.5946E-07

nodes 10 and 4). Therefore, the crack will grow faster when the peak stress occurs at the end points of the crack front.

From the coordinates of the original crack points, we determine the new contour shape of the crack front (see section “New contour crack front computations” for details). x_0 and y_0 correspond to the coordinates of the original crack points. x_n and y_n correspond the new coordinates along the crack front. The initial crack depth 'a', as depicted in Figure 8.7, is found to be 6 mm (0.24 inch). This has been observed during NDT inspection.

8.4.3.3. Stage no. 2. In the same way, for $\Delta N = 15000$ cycles, we calculate the subsequent crack growth. Results are summarized in Table 8.3. From the current coordinates of the crack points along the crack front, we determine the new contour shape.

Table 8.2. New crack front coordinates ($\Delta N = 1$)

Node	x_0	y_0	x_n	y_n
10	-0.01367	0.08141	-0.01367	0.08141
131	-0.01218	0.08032	-0.01218	0.08032
130	-0.01060	0.07936	-0.01060	0.07936
129	-0.00895	0.07853	-0.00895	0.07853
128	-0.00724	0.07784	-0.00724	0.07784
127	-0.00548	0.07729	-0.00548	0.07729
126	-0.00367	0.07688	-0.00367	0.07688
125	-0.00184	0.07663	-0.00184	0.07663
1	0.	0.07655	0.	0.07655
63	0.00184	0.07663	0.00184	0.07663
62	0.00367	0.07688	0.00367	0.07688
61	0.00548	0.07729	0.00548	0.07729
60	0.00724	0.07784	0.00724	0.07784
59	0.00895	0.07853	0.00895	0.07853
58	0.01060	0.07936	0.01060	0.07936
57	0.01218	0.08032	0.01218	0.08032
4	0.01367	0.08141	0.01367	0.08141

8.4.3.4. Stage no. 3. Results are summarized in Table 8.5 for a new increment of $\Delta N = 10000$. The new crack front is illustrated in Table 8.6.

Based on the step-by-step calculations, as shown above (stage no.1, stage no. 2, and stage no. 3), the number of cycles was found to be $N = 25,001$. We observe that ΔK_{eff} is higher at the edges of the flaw; i.e. nodes 10 and 4. Therefore, the crack will grow faster when the peak stress occurs at these end points of the crack front. The crack dimension c was initially measured as $c = 13.66$ mm (see Figure 8.7). At $N = 25001$ cycles, $c = 19.22$ mm.

The number of cycles, $N = 25001$ for this amount of crack growth, corresponds approximately to 68 years if the joints of the bridge are completely unlocked. On the other

Table 8.3. Determination of ΔK_{eff} and Δa_i along the crack front ($\Delta N = 15000$)

Node	ΔK_{eff} [MPa \sqrt{m}]	Δa_i [m]
10	30.69	0.00299
131	1.69	5.03787E-07
130	1.91	7.24210E-07
129	0.65	2.91629E-08
128	0.65	2.79232E-08
127	0.33	3.75367E-09
126	0.24	1.38816E-09
125	0.15	3.66135E-10
1	0.13	2.45680E-10
63	0.19	6.83297E-10
62	0.27	2.10485E-09
61	0.35	4.62898E-09
60	0.43	8.54081E-09
59	0.38	5.92556E-09
58	1.50	3.49328E-07
57	0.81	5.56189E-08
4	28.52	0.00240

hand, it was found that the maximum stress intensity factor under locked conditions is about 2 times higher than under unlocked conditions (see plot 7.20 in Chapter 7). Accordingly, it was estimated that 9 years should correspond to the locked conditions. Therefore, the reduction in time to growth (locked versus unlocked) is indicative of severity of locked case, although the crack was not grown to failure in the present analysis.

8.5. Concluding remarks

We have established a framework for assessment of structural integrity and fatigue life of pin and hanger connections. The relatively complex way in which the crack length

Table 8.4. New crack front ($\Delta N = 15000$)

Node	x_0	y_0	x_n	y_n
10	-0.01367	0.08141	-0.01661	0.08086
131	-0.01218	0.08032	-0.01218	0.08032
130	-0.01060	0.07936	-0.01060	0.07936
129	-0.00895	0.07853	-0.00895	0.07853
128	-0.00724	0.07784	-0.00724	0.07784
127	-0.00548	0.07729	-0.00548	0.07729
126	-0.00367	0.07688	-0.00367	0.07688
125	-0.00184	0.07663	-0.00184	0.07663
1	0.	0.07655	0.	0.07655
63	0.00184	0.07663	0.00184	0.07663
62	0.00367	0.07688	0.00367	0.07688
61	0.00548	0.07729	0.00548	0.07729
60	0.00724	0.07784	0.00724	0.07784
59	0.00895	0.07853	0.00895	0.07853
58	0.01060	0.07936	0.01060	0.07936
57	0.01218	0.08032	0.01218	0.08032
4	0.01367	0.08141	0.01604	0.08098

must be determined for each load cycle and the step-by-step counting method of generating crack growth requires long running times and tedious calculations.

Crack growth calculations were carried out for the unlocked case only. We estimate, based on initial stress intensity factors for the locked case that the time to growth the crack to $c = 19.22$ mm would be reduced by a factor of 2 from that in the unlocked case.

No attempt to grow the crack to failure was made and these calculations merely serve to illustrate the severity of the locked case over that of the unlocked. More detail investigations of the actual fatigue crack growth mechanisms would be required in order to make statements about failure processes in actual bridge pins.

Table 8.5. Determination of ΔK_{eff} and Δa_i along the crack front ($\Delta N = 10000$)

Node	ΔK_{eff} [MPa \sqrt{m}]	Δa_i [m]
10	33.81	0.00267
131	4.84	7.81884E-06
130	1.15	1.05268E-07
129	0.61	1.58729E-08
128	0.69	2.30617E-08
127	0.33	2.43124E-09
126	0.25	1.08732E-09
125	0.21	6.87759E-10
1	0.24	9.24543E-10
63	0.26	1.20456E-09
62	0.31	1.98834E-09
61	0.39	4.02679E-09
60	0.34	2.84216E-09
59	0.41	4.69905E-09
58	0.88	4.78468E-08
57	3.71	3.53363E-06
4	28.78	0.00164

Table 8.6. New crack front ($\Delta N = 10000$)

Node	x_0	y_0	x_n	y_n
10	-0.01661	0.08086	-0.01922	0.08028
131	-0.01218	0.08032	-0.01218	0.08032
130	-0.01060	0.07936	-0.01060	0.07936
129	-0.00895	0.07853	-0.00895	0.07853
128	-0.00724	0.07784	-0.00724	0.07784
127	-0.00548	0.07729	-0.00548	0.07729
126	-0.00367	0.07688	-0.00367	0.07688
125	-0.00184	0.07663	-0.00184	0.07663
1	0.	0.07655	0.	0.07655
63	0.00184	0.07663	0.00184	0.07663
62	0.00367	0.07688	0.00367	0.07688
61	0.00548	0.07729	0.00548	0.07729
60	0.00724	0.07784	0.00724	0.07784
59	0.00895	0.07853	0.00895	0.07853
58	0.01060	0.07936	0.01060	0.07936
57	0.01218	0.08032	0.01218	0.08032
4	0.01604	0.08098	0.01765	0.08064

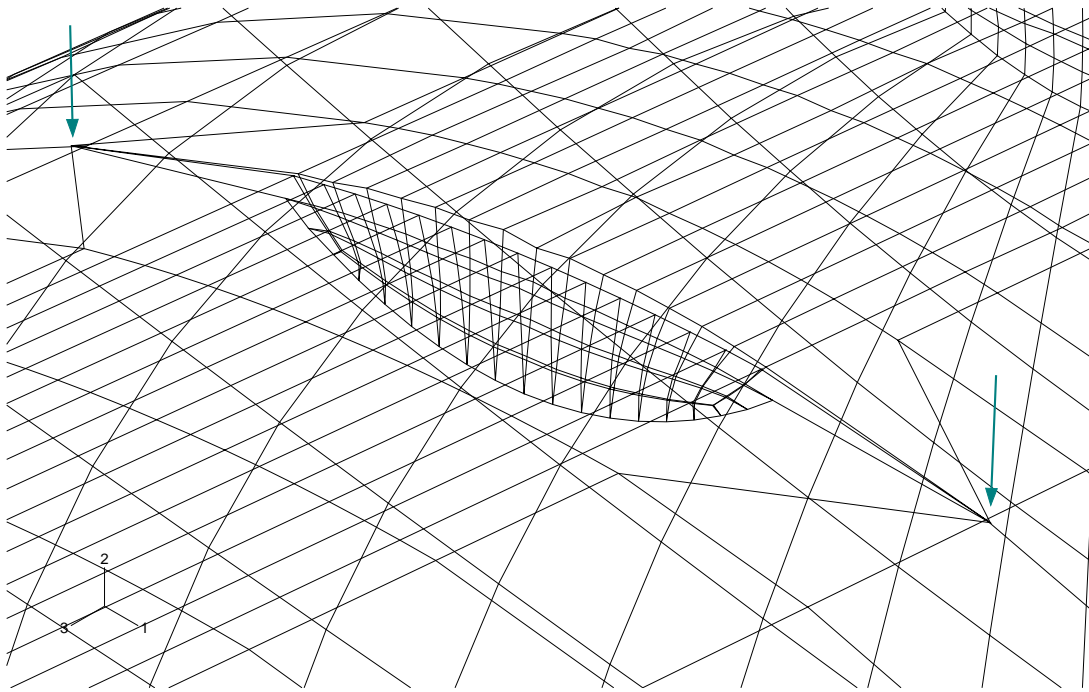


Figure 8.6. Deformed mesh showing new contour crack front

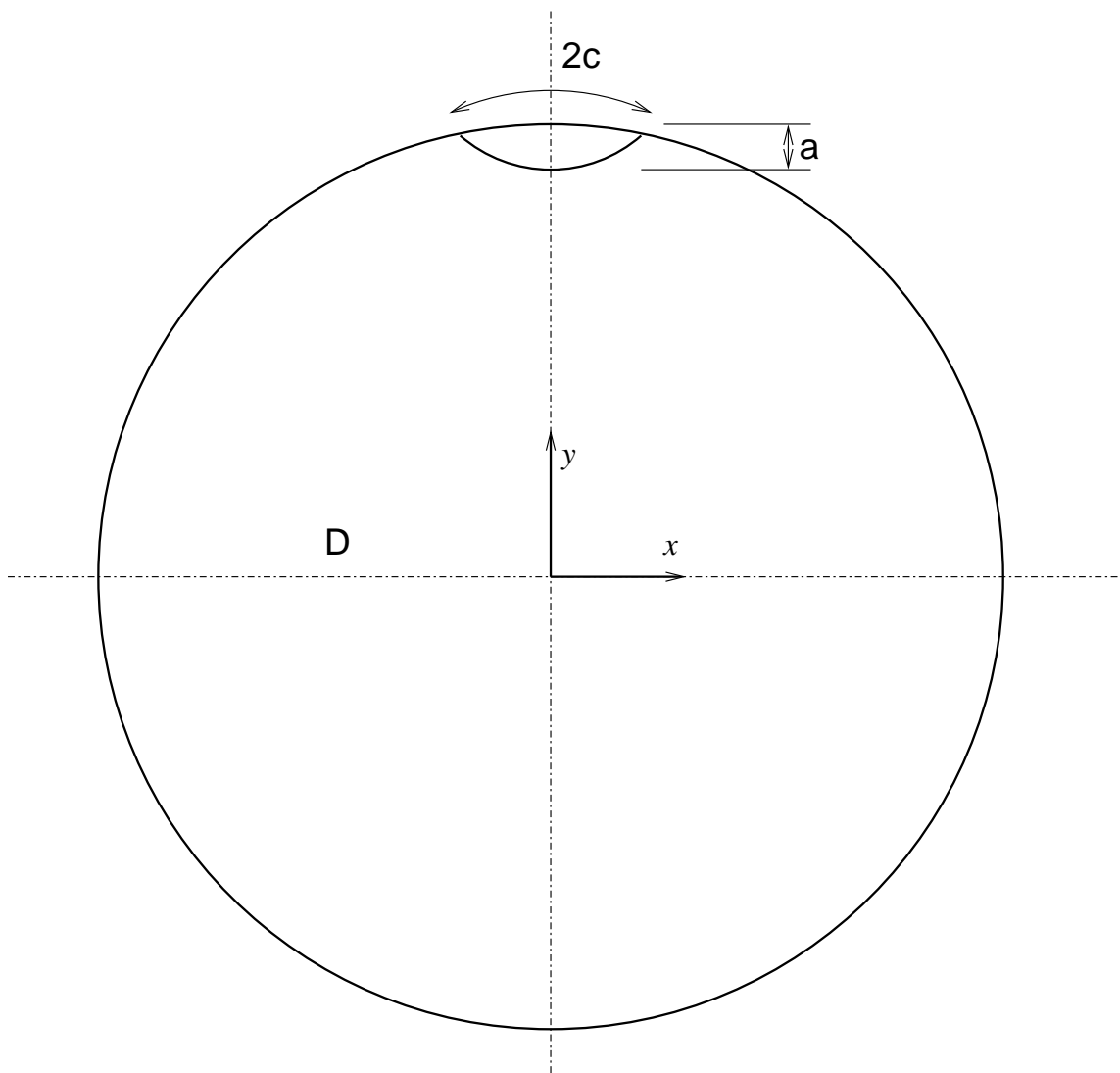


Figure 8.7. Initial crack dimensions: $a=6$ mm, $c=13.66$ mm, $D=165.1$ mm

CHAPTER 9

Conclusion and discussion**9.1. General discussions and recommendations**

The aim of the present study was to investigate failure mechanisms of the pin and hanger connections in aging highway steel bridges.

The aging of highway bridges is increasing the anxiety in all sectors of the industry, particularly as there is a desire to operate the bridges beyond their original design lives. Crack formation and growth in the vicinity of the joint connection has been identified as a serious problem. The presence of cracks or flaws in complex three-dimensional components is always a cause of concern to engineers. The frightening aspect of fatigue failure mechanisms is that initial crack growth can often go undetected.

The aim also was to relate design calculations, originally performed in bridge design in its earlier stage, to the entire structure behavior analysis carried out by our investigations. Note that the design calculations were originally done in few single components; e.g. tension in hanger, shear stress in the pin.

The advent of high speed computer has led to further advances in the use of numerical method of stress analysis by means of the FEA. Furthermore, improved knowledge of material behavior, plasticity, and mechanisms of fracture made possible the complete analysis.

Based on the findings, the following conclusions can be drawn:

- *Over-stressing.* Plastic deformation occurred in several critical components, in particular when the joints become completely frozen. Moments and high stress concentration were generated from thermal expansion/contraction as well as live loading once the pin was restrained from rotation. The mechanical freezing condition of the lower pin can be attributed to the corrosion (pack-rust) due to salt and debris accumulation. Furthermore, fatigue and reduction of fracture toughness associated with low temperatures were among operating parameters to take into account in design purpose. Therefore, better design of the pin and hanger connection is required. Here are some basic recommendations:
 - (a) Partial sealing of the pin-and-hanger housing. This would help to prevent salt and debris to accumulate near the joint.
 - (b) Greasing the lower and upper pins during regular inspections to ensure free rotation of the links.
- *Structurally deficient.* It is also interesting to note that when the bridge was designed (1954s), only a few part components were checked and compared to the AASHTO specifications; i.e. tension in hanger, shear stress in pin. According to the bridge design document, there is no indication on the effects of temperature changes, nor the frozen condition inside the joints. The analyses are limited to room temperature. The assumptions of the design calculations were mainly based on an “idealistic” condition. Each connected element was assumed to freely rotate relative to each other. In the present study, we found that the bridge elements are over-stressed under the given applied loads and extreme environmental conditions pertaining to the locked condition.

We would hope that advances in steel making, non-destructive evaluation, and numerical procedure will promote to a better bridge design in the future.

9.1.1. Crack growth

The present study also has been focused on crack growth modeling. The focus was performing 3D contact analysis of connecting elements incorporating crack. This is an important concern since changes in contact loads may lead to changes in stress intensity factors (SIFs) and therefore result in alteration of the crack front. This effect became more noticeable as the crack grew.

It should be note that ABAQUS does not have the fatigue crack capability in its current version. Therefore, the most significant feature that contributes to the simplicity and efficiency use of the finite element program ABAQUS, for a crack growth modeling in 3D, is a technique which allows for the calculation of the normal position for the new crack front. It is implemented as an add-on tool for ABAQUS program.

We have established a framework for assessment of structural integrity and fatigue life of pin and hanger connections. Our initial investigation gave preliminary but plausible results on the effects of temperature fluctuations as well as mechanical lock up of the pins on stress values and on susceptibility for crack growth.

Although, ABAQUS has an automatic mesh generation capability (ABAQUS/CAE), construction of a proper 3D crack model requires some human intervention and a certain skills from the analyst.

In addition, while the majority of complex geometries are still created with an underlying tetrahedral element, here we have had success by making our entire bridge model with high quality brick shaped elements.

9.1.2. Non-destructive evaluation (NDE)

As mentioned earlier, most of the work and publications, on the assessment of aging bridges, have been focused on non-destructive evaluation (NDE). Non-destructive testing (NDT) or NDE of materials is an inspection procedure used to produce information leading to decisions on the serviceability of components or structures. These procedures are often complex requiring expensive equipment and skilled experts to operate efficiently. Quantitative NDE techniques are needed for evaluating sizes, shapes, and locations of defects and cracks. On the other hand, computational mechanics, in particular FEA, is a tool for these tasks as well. Perhaps, the combination of these 2 tools should be used in the future for an efficient assessment of the structural integrity of the bridge.

9.2. Future work

An automated crack growth program, as an add-on tool, for commercially available FE program (ABAQUS) is needed if we want to use such commercial program in engineering applications. An application program interface (API) using Python programming language may be an appropriate way to do this. This may lead to an automatic global remeshing for modeling crack propagation.

There is another possibility which consists to interface between the extended finite element method (X-FEM) and ABAQUS. In the extended finite element method (X-FEM), the approximation of the displacement field is enriched in the vicinity of the crack by incorporating additional basis functions using a partition of unity approach. For further details, see for example Sukumar *et al.* (2000) [48] and Sukumar *et al.* (2003) [49], amongst others.

Finally, other aspect that could be included in the simulation is the corrosion. These effects which cannot be easily incorporated (oxidation/corrosion) may enhance crack growth.

References

- [1] G. Chen, C. Courtright, L. R. Dharani, and B. Xu. Failure investigation of the steel strut of Paseo suspension bridge. In *Performing Organization Report*. Missouri Department of Transportation (MoDOT), 2005.
- [2] ABAQUS Inc. *ABAQUS Manuals (version 6.45)*. HKS Inc., 2003.
- [3] D. E. Kelsey and M. A. Rotundo. Ultrasonic Testing of Bridge Pins and Hanger Straps. *Materials Evaluation*, pages 488–493, 1990.
- [4] J. M. South, C. Hahin, and R. O. Telford. Analysis, Inspection, and Repair Methods for Pin Connections on Illinois Bridge. In *Physical Research Report*, volume 107. Illinois Department of Transportation (IDOT), 1992.
- [5] R. A. Walther and R. D. Gessel. Ultrasonic Inspection of Bridge Pin and Hanger Assemblies. In *Proc. Structural Materials Technology*, pages 23–28. San Diego, 1996.
- [6] B. A. Graybeal, R. A. Walther, and G. A. Washer. Ultrasonic Inspection of Bridge Hanger Pins. *Transportation Research Record*, 1697:19–23, 2000.
- [7] D. E. Tonnias and J. J. Zhao. *Bridge Engineering*. McGraw-Hill, 2nd edition, 2007.
- [8] R. D. Cook, D. S. Malkus, and M. E. Plesha. *Concepts and Applications of Finite Element Analysis*. John Wiley, 4th edition, 2002.
- [9] M. R. Gosz. *Finite Element Method - Applications in Solids, Structures, and Heat Transfer*. CRC, 2006.
- [10] F. K. Hubbard. Design Computations. *Wisconsin Department of Transportation (WisDOT)*, 1999.
- [11] American Association of State Highway and Transportation Officials (AASHTO). *Standard Specifications for Highway Bridges*. AASHTO, Washington D. C., 15th edition, 1996.

- [12] T. Belytschko, W. K. Liu, and B. Moran. *Nonlinear Finite Elements for Continua and Structures*. John Wiley, 2000.
- [13] P. Wriggers. *Computational Contact Mechanics*. John Wiley, 2002.
- [14] S. P. Timoshenko and J. N. Goodier. *Theory of elasticity*. McGraw-Hill, 2nd edition, 1951.
- [15] L. E. Malvern. *Introduction to the Mechanics of a Continuous Medium*. Prentice-Hall, 1969.
- [16] Y. C. Fung. *Foundations of Solid Mechanics*. Prentice-Hall, 1965.
- [17] G. A. Holzapfel. *Nonlinear Solid Mechanics: A Continuum Approach for Engineering*. Wiley, 2000.
- [18] R. Hill. *The Mathematical Theory of Plasticity*. Clarendon Press, 1950.
- [19] D. R. J. Owen and E. Hinton. *Finite elements in plasticity*. Pineridge Press, U.K., 1980.
- [20] M. A. Crisfield. *Non-linear Finite Element Analysis of Solids and Structures*. John Wiley, 1991.
- [21] A. S. Khan and S. Huang. *Continuum Theory of Plasticity*. John Wiley, 1995.
- [22] C. W. Roeder. Proposed Design Method for Thermal Bridge Movements. *Journal of Bridge Engineering*, pages 12–19, 2003.
- [23] R. W. Hertzberg. *Deformation and Fracture Mechanics of Engineering Materials*. John Wiley, 4th edition, 1996.
- [24] A. P. Boresi and R. J. Schimdt. *Advanced Mechanics of Materials*. John Wiley, 5th edition, 2003.
- [25] M. Gosz and B. Moran. Stress-intensity factors for elliptical cracks emanating from countersunk rivet holes. *U.S. Dept. of Transportation - The FAA*, 1998.
- [26] I. S. Raju and J. C. Newman. Stress-intensity factors for a wide range of semi-elliptical surface cracks in finite-thickness plates. *Eng. Fracture Mechanics*, 11:817–829, 1979.

- [27] J. C. Newman Jr. and I. S. Raju. Stress-intensity factor equations for cracks in three-dimensional finite bodies. *ASTM STP 791 - Fracture Mechanics*, pages 238–265, 1983.
- [28] B. Moran and C. F. Shih. A general treatment of crack tip contour integrals. *Int. J. of Fracture*, 35:295–310, 1987.
- [29] B. Moran and C. F. Shih. Crack tip and associated domain integrals from momentum and energy balance. *Eng. Fract. Mech.*, 27:615–642, 1987.
- [30] J. Schijve. *Fatigue of Structures and Materials*. Kluwer Academic Publishers, 2001.
- [31] H. Tada, P. C. Paris, and G. R. Irwin. *The stress analysis of cracks handbook*. Del Research Corp., 1973.
- [32] D. P. Rooke and D. J. Cartwright. *Stress Intensity Factors*. Her Majesty's Stationary Office, London, 1976.
- [33] Y. Murakami (ed.). *Stress Intensity Factors Handbook*. Pergamon Press, Oxford, 1987.
- [34] I. S. Raju and J. C. Newman Jr. Stress-intensity factors for circumferential surface cracks in pipes and rods under tension and bending loads. *ASTM STP 905 - Fracture Mechanics*, 17:789–805, 1986.
- [35] M. Shiratori, T. Miyoshi, Y. Sakai, and G. R. Zhang. Analysis of stress intensity factors for surface cracks subjected to arbitrarily distributed surface stresses. *Trans. Jap. Soc. Mech. Eng.*, pages 660–662, 1986.
- [36] Y. S. Shih and J. J. Chen. The stress intensity factor study of an elliptical cracked shaft. *Nucl. Eng. and Des.*, 214:137–145, 2002.
- [37] C. Q. Cai and C. S. Shin. A discussion on The stress intensity factor study of an elliptical cracked shaft. *Nucl. Eng. and Des.*, 227:355–358, 2004.
- [38] P. C. Paris and G. C. Sih. Stress Analysis of Cracks. In *Fracture Toughness Testing and its Applications*, ASTM STP 381. American Society for Testing and Materials (ASTM), Philadelphia, 1965.
- [39] J. M. Barsom and S. T. Rolfe. *Fracture and Fatigue Control in Structures*. American Society for Testing and Materials, 3rd edition, 1999.

- [40] H. M. Westergaard. Bearing Pressures and Cracks. In *Transactions, ASME. Journal of Applied Mechanics*, 1939.
- [41] G. R. Irwin. Analysis of Stresses and Strains Near the End of a Crack Transversing a Plate. In *Transactions, ASME*, volume 24. *Journal of Applied Mechanics*, 1957.
- [42] D. M. Parks. The virtual crack extension method for nonlinear material behavior. *Comp. Meth. in Appl. Mech. Eng.*, 12:353–364, 1977.
- [43] C. F. Shih, B. Moran, and T. Nakamura. Energy Release Rate along a Three-Dimensional Crack Front in a Thermally Stressed Body. *J. of Appl. Mech.*, 30:79–102, 1986.
- [44] J. R. Rice. A Path Independent Integral and the Approximation Analysis of Strain Concentration by Notches and Cracks. *J. of Appl. Mech., Transactions of ASME*, 35, 1968.
- [45] F. Z. Li, C. F. Shih, and A. Needleman. A comparison of methods for calculating energy release rates. *Eng. Fracture Mechanics*, 21:405–421, 1985.
- [46] M. T. Hanson and L. M. Keer. An Analytical Life Prediction Model for the Crack Propagation Occuring in Contact Fatigue Failure. *Tribology Transactions*, 35:451–461, 1992.
- [47] P. C. Paris and F. Erdogan. A critical analysis of crack propagation laws. *Trans ASME, Series D*, 85:528–535, 1963.
- [48] N. Sukuma, N. Moes, B. Moran, and T. Belytschko. Extended Finite Element Method (X-FEM) for Three-Dimensional Crack Modeling. *Int. J. Num. Meth. in Eng.*, 11:1549–1570, 2000.
- [49] N. Sukuma, D. L. Chopp, and B. Moran. Extended Finite Element Method and Fast Marching Method for Three-Dimensional Fatigue Crack Propagation. *Eng. Fracture Mechanics*, 70:29–48, 2003.
- [50] American Institute of Steel Construction. *Manual of Steel Construction*. AISC, Chicago, 9 edition, 1992.
- [51] F. P. Beer and E. R. Johnston. *Mechanics of Materials*. McGraw-Hill, 2nd edition, 1992.
- [52] E. P. Popov. *Mechanics of Materials*. Prentice-Hall, 1978.

- [53] M. E. Fine and S. Vaynman. Development and Commercialization of High-performance Steel. *Dept of Transportation (DoT)*, 2003.
- [54] S. Zoruba and K. A. Grubb. Steel - Solution Center. *Modern Steel Construction*, 2003.
- [55] SCM Steel Construction Manual. Steel Materials. *SCM*, 2006.
- [56] C. P. Larrabee. Corrosion Resistance of High-Strength Low-Alloy Steels as Influence by Composition and Environment. *Corrosion*, 9:259–271, 1953.
- [57] R. A. Legault and H. P. Leckie. Effect of Alloy Composition on the Atmospheric Corrosion Behavior of Steels Based on a Statistical Analysis. *Corrosion in Natural Environments - ASTM STP 558*, pages 334–347, 1974.
- [58] H. E. Townsend and J. C. Zoccola. Eight-Year Atmospheric Corrosion Performance of Weathering Steel in Industrial, Rural, and Marine Environments. *Atmospheric Corrosion of Metals - ASTM STP 767*, pages 45–59, 1982.
- [59] S. K. Coburn, M. E. Komp, and S. C. Lore. Atmospheric Corrosion Rates of Weathering Steels at Test Sites in the Eastern United States - Effect of Environment and Test-Panel Orientation. *Atmospheric Corrosion - ASTM STP 1239*, pages 101–113, 1995.
- [60] H. H. Uhlig. *Corrosion Handbook*. John Wiley, 1948.
- [61] M. G. Fontana. *Corrosion Engineering*. McGraw-Hill, 3rd edition, 1986.

APPENDIX A

Design requirements according to AASHTO**A.1. AASHTO code**

The American Association of State Highway and Transportation Officials (AASHTO) [11] specifications are to highway bridge design engineers what the American Institute of Steel Construction (AISC) are to designers of steel structures and the American Concrete Institute (ACI) are to designers of concrete structures.

AASHTO specifications are the bible of highway bridge design engineers. They are intended to serve as a standard or a *guide* for the preparation of state specifications and as a reference for bridge engineers [7].

The AASHTO specifications apply to ordinary highway bridges up to spans of 500 ft. For longer spans and unusual bridges, supplementary specifications are usually required. The specifications were periodically revised every four to six years to incorporate the new knowledge found through research and development.

In general, an acceptable structure should meet all requirements of safety and performance. The safety evaluation of a bridge structure requires checking if the effects of the loads applied on the structure exceed the capacities of individual members or the capacity of the whole system. Traditional design was based on the concept of a *factor of safety* to supposedly cover all unknowns and imprecise known factors, i.e., the initial yield stress and the tensile strength of the material.

Here, we present two different types of calculations:

- Design calculations
- AASHTO specifications

The results will be compared in order to make sure that the design values are within the standard specifications. Then, they will be used to check the validation of the finite element results.

A.2. Design calculations

These design calculations are sometimes called *elastic design calculations*, since it is assumed that the material behaves elastically, i.e., it obeys Hooke's law under service loads, and the hand-calculations are based on the equations of Mechanics of Materials.

Only the *dead* and *live* loads which include *impact* are taken into account here. Dead loads also called permanent loads consist of the *weight* of the entire structure, which should include the roadway (deck), road surfacing, sidewalks, supporting members, and any other permanent attachments to the bridge. The live loads, which are very different from those encountered in building design, consist of truck loading and lane loading.

Individual structural members such as pin and hanger need to be checked in accordance to the standard specification . In general, the design provisions of the AASHTO [11] and AISC [50] are similar. However, some basic differences in allowable stresses, limiting thicknesses and sizes are evident [?].

A.2.1. Loading conditions

Because the most typical loads encountered in highway bridge structures are due to *dead* weight and vehicular traffic (*live* load including *impact*), only these two loads are considered in this study. It was estimated that the total load for one girder - for this particular highway bridge structure (WisDOT [10]) - is expressed as,

$$P = (LL + I) + DL = 71,000 + 197,000 = 268,000 \text{ lb}$$

where LL , I , and DL are used to reference *live loads*, *impact*, and *dead loads* respectively.

According to AASHTO (Table 10.32.1), the allowable stresses in steel structures are summarized as follows,

- Shear in pins, $F_v = 0.40 \times F_y = 14,000$ psi (ASTM A36)
- Tension in hanger, $F_t = 1.4 \times (0.55 F_y) = 27720$ psi (ASTM A36)

in which, F_y denotes yield stress (in AASHTO notations). These notations will be used throughout this Section.

A.2.2. Shear stress in pin

Although there is no simple way to find the shear stresses acting throughout the entire circular cross section, we can readily determine the shear stresses at the neutral axis (where the stresses are the largest) by making some reasonable assumptions about the stress distribution ([51], [52]). We assume that the stresses act parallel to the y -axis and have constant intensity across the width of the pin (Figure A.1). In this problem, there are two planes of shear, and so the pin is said to be in double shear. In double shear,

each of the shear forces (V) is equal to one-half of the total load (P) transmitted, that is $V = P/2$. The shear forces are the resultants of the shear stresses distributed over the cross-sectional area of the pin. Thus, the average shear stress is obtained by dividing the shear force V by the area A of the cross section on which it acts.

$$\tau_{av} = \frac{V}{A} = \frac{V}{\pi d^2/4} = \frac{134,000}{\pi \times 6.5^2/4} = 4.04 \text{ ksi}$$

where V is the shear force, A is the cross-sectional area, and τ_{av} is the average shear stress. As mentioned earlier, the total load is 268 klb (1192 kN), and the diameter of the pin (d) is 6.5 in. (165 mm).

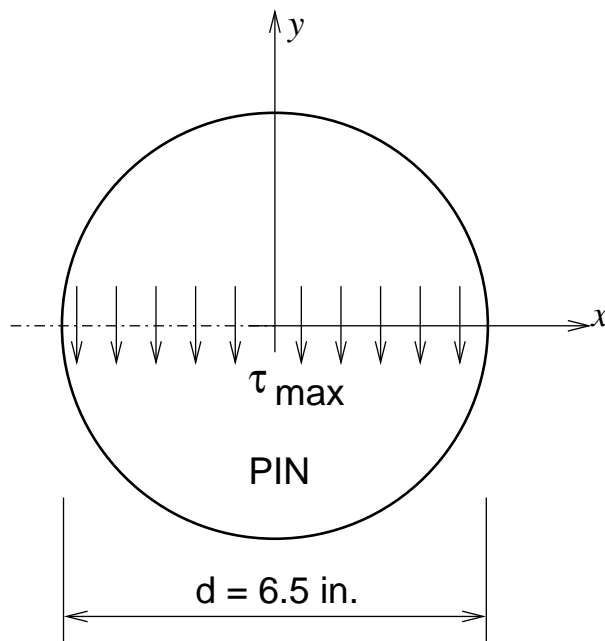


Figure A.1. Shear stress acting on the cross section of a pin

Furthermore, the elementary beam theory, based on the assumption that the shearing stress is uniformly distributed along the horizontal diameter of the cross section gives the

maximum stresses which is equal to $4/3$ times the average shear stress V/A . Thus, the maximum shear stress is $4/3 \times 4.04 = 5.39$ ksi.

On the other hand, according to AASHTO, the allowable stress for shear in the pin is given by

$$F_v = 0.40 \times F_y = 0.40 \times 36 = 14.40 \text{ ksi}$$

in which, F_v denotes allowable shear stress and F_y denotes yield stress.

A.2.3. Tension in hanger

In the design or analysis of a connection, it may be necessary to check the *tensile* capacity of the connected member itself (hanger). Because the connections are subjected simultaneously to shear and tension loads, they are required special analysis to assure conformance to specification provisions (AASHTO) for values of F_v and F_t which denote allowable shear and tension stresses respectively.

Note that hanger plates are designed to carry the tensile load and transfer the load to another connected member (Figure A.2.3). Note that (a) represents the front view of the connection, and (b) the side view of the connection.

The allowable stress in the hanger plate is taken across the member net area. The net cross-sectional area, that is, the area that remains after the hole is drilled through the hanger, is equal to the net width times the thickness. The net area is normally used when the bar is in tension. That is the case for pin-hanger connections. In addition, the stresses are assumed to be uniformly distributed over an area. The net width w_{net} is equal to the gross width w minus the holes. Thus,

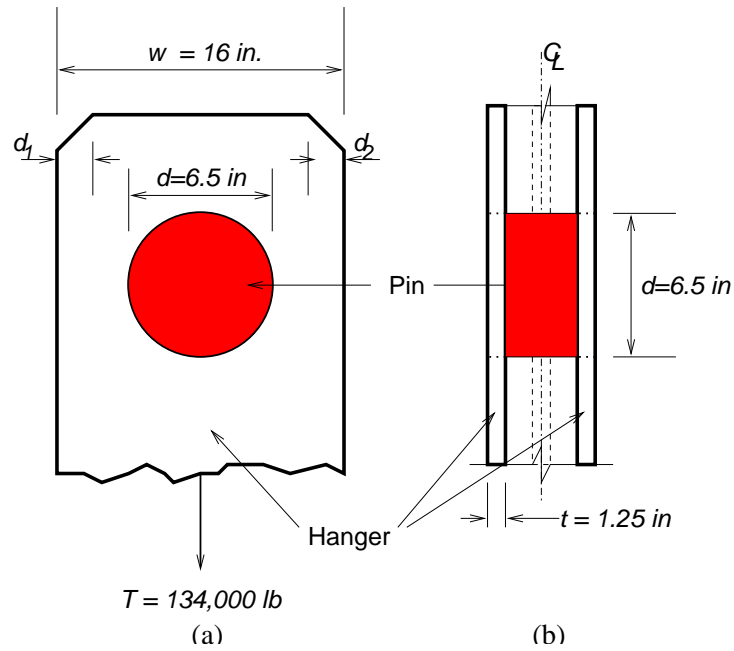


Figure A.2. Hanger plate subjected to a tensile load T

$$w_{net} = w - \sum_i d_i = 8.624 \text{ in.}$$

Hence, the net area becomes

$$A_{net} = w_{net} \times t = 8.624 \text{ in.} \times 1.25 \text{ in.} = 10.78 \text{ in}^2$$

Hence, the axial tension in hanger is

$$\begin{aligned}
 f_t &= \frac{T}{A_{net}} \\
 &= \frac{134,000 \text{ lb}}{10.78 \text{ in}^2} \\
 &= 12.43 \text{ ksi}
 \end{aligned}
 \tag{A.1}$$

In addition, according to AASHTO (AASHTO 10.25.1), the net section across the pin hole shall be not less than 140 percent, and the net section back of the pin hole not less than 100 percent of the body of the member. Therefore, the axial tension (Equation A.1) becomes:

$$f_t = 12.43 \text{ ksi} \times (140\%) = 17.40 \text{ ksi}$$

Thus, the allowable axial tension stress (AASHTO 10.25.1) is

$$F_t = 0.55 F_y \times (140\%) = 27.72 \text{ ksi}$$

in which F_y denotes yield stress in AASHTO notations. Table A.1 summarizes the above results for design requirements.

Table A.1. Results for the shear stress in pin and tension in hanger

<i>Stress</i>	<i>Design</i>		<i>AASHTO</i>	
	ksi	MPa	ksi	MPa
Shear in pin	4.04	27.85	14.40	99.28
Tension in hanger	12.43	85.70	27.72	191.12

For more information about these calculations, one can refer to the American Association of State Highway and Transportation Officials (AASHTO) specifications, 1996 [11], the Wisconsin Department of Transportation (WisDOT), 1999 [10], Beer and Johnston, 1992 [51], and Popov, 1978 [52].

APPENDIX B

Material selection

The selection of materials may be driven by project requirements. For many decades, bridges have been fabricated from plain carbon steels that have yield strengths between 36 ksi and 50 ksi.

Another problem with steel as a structural material is its susceptibility to corrosion. Pre-heating and post-heating of these steels were generally needed to prevent welding cracks that in combination with low fracture toughness (K_C) of the steel at low temperature have led to catastrophic failures [39].

B.1. NUCu 70W

In the early 1990s, the Federal Highway Administration (FHWA) and the Navy identified a need for a high performance weatherable structural steel that would have a 70 ksi yield strength. Lower carbon content for improved welding and high fracture toughness at cryogenic temperatures was desired for this steel. Under the auspice of the FHWA/Navy/AISI Steering Committee a new steel designated ASTM HPS 70W was developed. At Northwestern University, several years after the development described above began, a different approach was taken to meet the 70 ksi yield strength target. A NUCu 70W was thus created. The steel has a number of advantages over the ASTM HPS 70W. Under the Infrastructure Technology Institute (ITI) sponsorship, Fine and Vaynman (2003) [53] developed a copper precipitation-hardened, high-performance weathering steel

(NUCu 70W) steel having the lowest carbon equivalent of any structural steel and can be easily welded without pre- or post-heating. The fracture toughness is high compared to other structural steels particularly at cryogenic temperatures. Weathering resistance and corrosion resistance properties are better than those of any other available weathering steel. Copper significantly improves the corrosion resistance of steel in marine and inland environments. The high copper content in NUCu steel is effective in substantially reducing the weight loss.

NUCu steel is now included in the ASTM A710 Standard. The steel was used for rehabilitation of a bridge in Illinois. The Illinois Department of Transportation (IDOT) recently announced the completion of a new bridge in Lake Villa, Lake County (Illinois) constructed with NUCu steel.

Details can be found in Fine and Vaynman (2003) [53].

Table B.1. Material properties (NUCu 70W)

Material	σ_Y		σ_{UTS}		Elongation
	ksi	MPa	ksi	MPa	%
NUCu 70W	70	483	80	552	27

B.2. ASTM A992

It should also be noted that the list of available steel changes from time to time. For example, in the earlier to mid 1900s the only steel specification was ASTM A6 steel which is no longer on the list [54].

Later other steels were developed including ASTM A36 and ASTM A572 which were widely used in the building and bridge structures. A36 steel has a minimum yield stress

of 36 ksi. The ultimate tensile stress of this steel varies from 58 to 80 ksi. For design calculations, it is suggested to use the minimum value of 58 ksi for the ultimate tensile strength. Around the year 2000, ASTM A992 steel was introduced which meets the requirements of both ASTM A36 and ASTM A572 and has now become the dominate steel specification. ASTM A992 includes a yield strength range of 50 ksi to 65 ksi and a minimum tensile strength of 65 ksi.

Details can be found in Zoruba and Grubb (2003) [54] and the SCM steel Construction Manual (2003) [55].

APPENDIX C

Pack-rust formation and expansion**C.1. Introduction**

In this Section, we present a simplified model describing the ratio of pack-rust expansion based on chemical reaction.

As mentioned earlier, the failures in joint connections appear to be due to rust and other corrosion products, which had built-up between the connecting devices over many years. Figure C.1 illustrates the typical locations where corrosion is likely to occur.

For steel structures, such as bridges, the severity of deterioration will depend on how long the metal is exposed to water, oxygen, and salt. The rate of corrosion in different environments has been evaluated in several studies, in particular by Larrabee (1953) [56], Legault *et al.* (1974) [57], Townsend *et al.* (1982) [58], and Coburn *et al.* (1995) [59].

Based on their studies, the rate of corrosion can accelerate significantly in the presence of a *marine* environment or in *cold regions* where water and salt are usually combined.

C.2. Corrosion expansion calculation

Depending on the zone of attack, corrosion can occur as volume corrosion (three-dimensional), surface corrosion (two-dimensional), line corrosion (one-dimensional), or pitting (zero-dimensional). Further details on corrosion engineering can be found in textbooks, such as Uhlig (1948) [60] and Fontana (1986) [61].

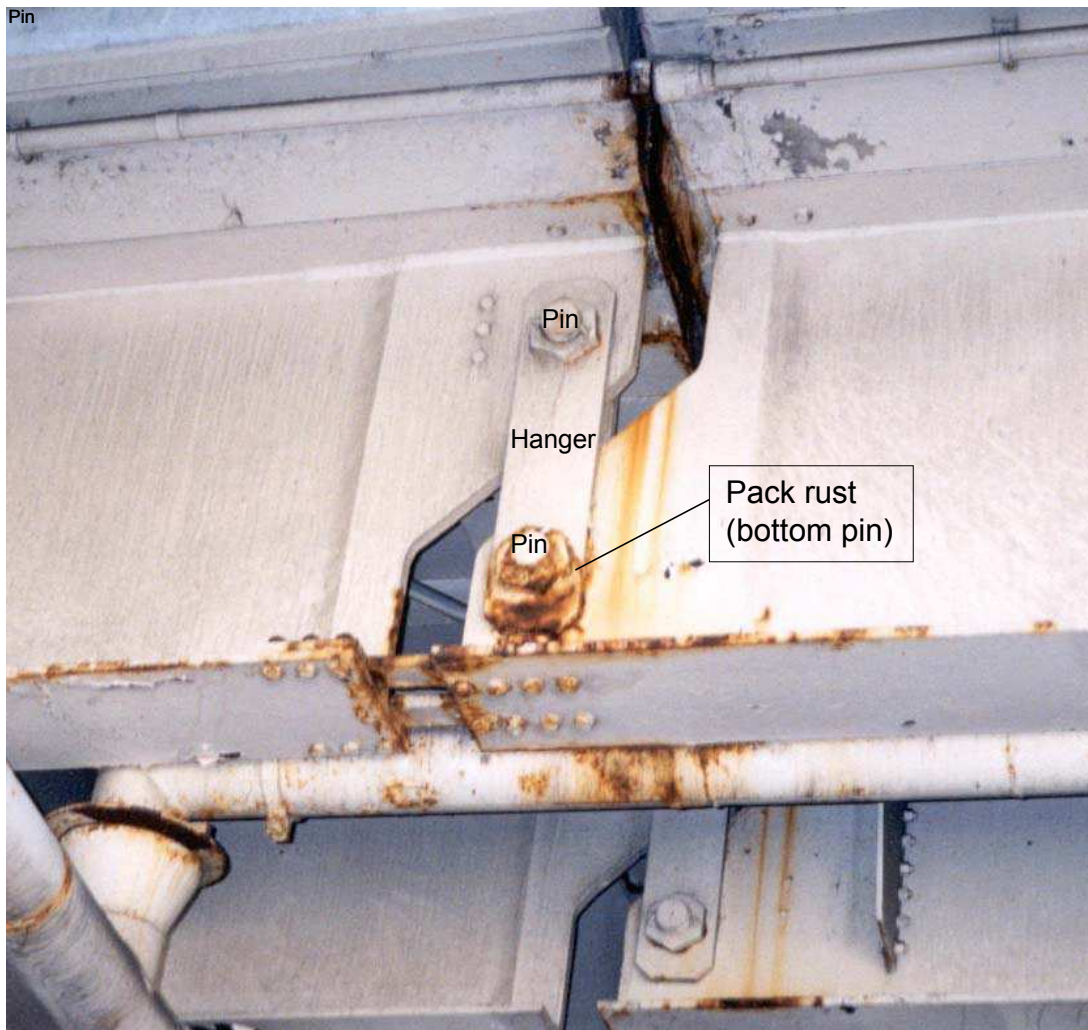


Figure C.1. Typical pack rust formation

C.2.1. Chemical reaction

The corrosion of steel can be considered as an electrochemical process that occurs in stages. Moist air and water containing carbon dioxide attack iron (Fe) to form rust that is *iron oxide hydrate* (red rust), as schematically illustrated in Figure C.2. The sum of these reactions can be represented by the following equation:

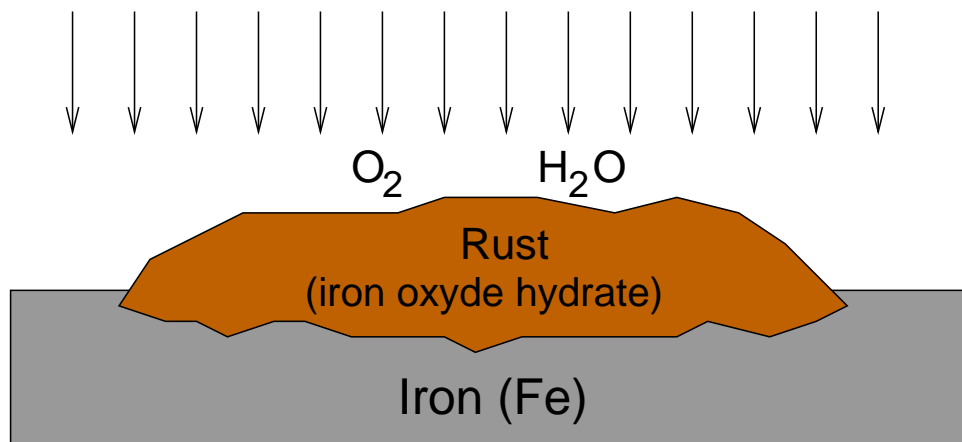
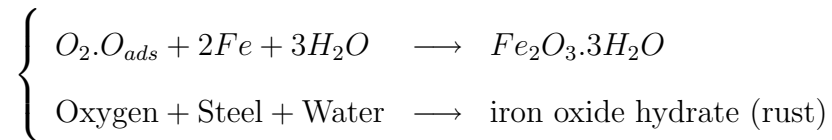


Figure C.2. Schematic representation of the corrosion formation

The process requires the simultaneous presence of water (H_2O) and oxygen (O_2). In the absence of either one, corrosion does not occur.

Because the resulting oxide layer is soft and porous, the changes can be calculated as follows.

- A mass of one mole of iron (Fe) = $2 \times 56 = 112$ g
- A mass of one mole of iron oxide hydrate is $Fe_2O_3 \cdot 3H_2O = 2 \times 56 + 3 \times 16 + 3(1 \times 2 + 16) = 214$ g

Thus, one gram (1 g) of iron is given by

$$1 \text{ g } (Fe) = \frac{214}{112} = 1.91$$

Using density expressions, the volumes of rust ($Fe_2O_3 \cdot 3H_2O$) and iron (Fe) can be expressed respectively as,

$$v_{rust} = \frac{m_{rust}}{d_{rust}} = \frac{214}{4.28} = 50.0 \text{ cm}^3$$

$$v_{iron} = \frac{m_{iron}}{d_{iron}} = \frac{112}{7.87} = 14.23 \text{ cm}^3$$

where v , m , and d denote volume, mass, and density respectively. Therefore, the volume expansion of these substances is expressed as,

$$\frac{v_{rust}}{v_{iron}} = \frac{50}{14.23} = 3.5$$

The result indicates that the pack-rust expansion is 3.5. This value provides a useful indication of likely corrosion expansion. However, because of variations in atmospheric environments, corrosion rate data cannot be generalized. It is the “micro-climate” immediately surrounding the bridge structure which determines corrosion rates (or expansion) for practical purposes. Details can be found in Larrabee (1953) [56], Legault *et al.* (1974) [57], Townsend *et al.* (1982) [58], and Coburn *et al.* (1995) [59].